

Received December 21, 2017, accepted February 4, 2018, date of publication March 9, 2018, date of current version March 28, 2018.

Digital Object Identifier 10.1109/ACCESS.2018.2814072

GNSS Transpolar Earth Reflectometry exploriNg System (G-TERN): Mission Concept

ESTEL CARDELLACH¹, (Member, IEEE), **JENS WICKERT²**, **RENS BAGGEN³**, **JAVIER BENITO⁴**, **ADRIANO CAMPS⁵**, (Fellow, IEEE), **NUNO CATARINO⁶**, **BERTRAND CHAPRON⁷**, **ANDREAS DIELACHER⁸**, **FRAN FABRA¹**, **GREG FLATO⁹**, **HEINRICH FRAGNER⁸**, **CAROLINA GABARRÓ¹⁰**, **CHRISTINE GOMMENGINGER¹¹**, **CHRISTIAN HAAS¹²**, **SEAN HEALY¹³**, **MANUEL HERNANDEZ-PAJARES⁵**, **PER HØEG¹⁴**, **ADRIAN JÄGGI¹⁵**, **JUHA KAINULAINEN¹⁶**, **SHFAQAT ABBAS KHAN¹⁷**, **NORBERT M. K. LEMKE¹⁸**, **WEIQIANG LI¹**, **SON V. NGHIEM¹⁹**, (Fellow, IEEE), **NAZZARENO PIERDICCIA²⁰**, (Senior Member, IEEE), **MARCOS PORTABELLA¹⁰**, **KIMMO RAUTIAINEN²¹**, **ANTONIO RIUS¹**, (Member, IEEE), **INGO SASGEN¹²**, **MAXIMILIAN SEMMLING²**, **C. K. SHUM²²**, **FRANÇOIS SOULAT²³**, **ANDREA K. STEINER²⁴**, **SÉBASTIEN TAILHADES¹⁸**, **MAIK THOMAS²**, **ROGER VILASECA²⁵**, **AND CINZIA ZUFFADA¹⁹**, (Member, IEEE)

¹Institute of Space Sciences (CSIC), 08193 Cerdanyola del Vallès, Spain

²GFZ German Research Centre for Geosciences, 14473 Potsdam, Germany

³IMST GmbH, 47475 Kamp-Lintfort, Germany

⁴Airbus DS Space Systems España, 28022 Madrid, Spain

⁵UPC/IEEC, 08034 Barcelona, Spain

⁶DEIMOS Engenharia, 1998-023 Lisbon, Portugal

⁷IFREMER, 29280 Plouzané, France

⁸RUAG Space GmbH, 1120 Wien, Austria

⁹Environment and Climate Change Canada, Victoria, BC V8P 5C2, Canada

¹⁰Institut de Ciències del Mar and Barcelona Expert Center on Remote Sensing, 08003 Barcelona, Spain

¹¹National Oceanography Centre, Southampton SO14 3ZH, U.K.

¹²Alfred Wegener Institute for Polar and Marine Research, 27570 Bremerhaven, Germany

¹³ECMWF, Reading RG2 9AX, U.K.

¹⁴Department of Physics, University of Oslo, 0371 Oslo, Norway

¹⁵Astronomical Institute, University of Bern, 3012 Bern, Switzerland

¹⁶Harp Technologies Oy, 02150 Espoo, Finland

¹⁷National Space Institute, Technical University of Denmark, 2800 Kongens Lyngby, Denmark

¹⁸OHB System AG, 82234 Weling/Oberpfaffenhofen, Germany

¹⁹Jet Propulsion Laboratory, California Institute of California, Pasadena, CA 91125, USA

²⁰Department of Information, Electronics and Communications Engineering, Università La Sapienza, 00185 Rome, Italy

²¹Finnish Meteorological Institute, 101 Helsinki, Finland

²²The Ohio State University, Columbus, OH 43210, USA

²³Collecte Localisation Satellites SA, 31520 Ramonville Saint-Agne, France

²⁴Wegener Center for Climate and Global Change, University of Graz, 8010 Graz, Austria

²⁵TRYO Group, 08530 La Garriga, Spain

Corresponding author: Estel Cardellach (estel@ice.csic.es)

This work was supported in part by the Spanish under Grant ESP2015-70014-C2-2-R and Grant ESP2015-70014-C2-1-R and in part by the Specific Expedition Budget of GFZ. The work of S. V. Nghiem was supported in part by the NASA Cryospheric Sciences Program and in part by the NASA Land Cover and Land Use Change Program.

ABSTRACT The global navigation satellite system (GNSS) Transpolar Earth Reflectometry exploriNg system (G-TERN) was proposed in response to ESA's Earth Explorer 9 revised call by a team of 33 multi-disciplinary scientists. The primary objective of the mission is to quantify at high spatio-temporal resolution crucial characteristics, processes and interactions between sea ice, and other Earth system components in order to advance the understanding and prediction of climate change and its impacts on the environment and society. The objective is articulated through three key questions. 1) In a rapidly changing Arctic regime and under the resilient Antarctic sea ice trend, how will highly dynamic forcings and couplings between the various components of the ocean, atmosphere, and cryosphere modify or influence the processes governing the characteristics of the sea ice cover (ice production, growth, deformation, and melt)? 2) What are the impacts of extreme events and feedback mechanisms on sea ice evolution? 3) What are the effects of the cryosphere behaviors, either rapidly changing or resiliently stable, on the global oceanic and atmospheric circulation and mid-latitude extreme events? To contribute answering these questions, G-TERN will measure key parameters of the sea ice, the oceans, and the atmosphere with frequent and dense coverage over polar areas, becoming a "dynamic mapper" of the

ice conditions, the ice production, and the loss in multiple time and space scales, and surrounding environment. Over polar areas, the G-TERN will measure sea ice surface elevation (<10 cm precision), roughness, and polarimetry aspects at 30-km resolution and 3-days full coverage. G-TERN will implement the interferometric GNSS reflectometry concept, from a single satellite in near-polar orbit with capability for 12 simultaneous observations. Unlike currently orbiting GNSS reflectometry missions, the G-TERN uses the full GNSS available bandwidth to improve its ranging measurements. The lifetime would be 2025–2030 or optimally 2025–2035, covering key stages of the transition toward a nearly ice-free Arctic Ocean in summer. This paper describes the mission objectives, it reviews its measurement techniques, summarizes the suggested implementation, and finally, it estimates the expected performance.

• **INDEX TERMS** Polar science, GNSS, reflectometry, GNSS-R, sea ice, altimetry, polarimetry, radio-occultation, Low Earth Orbiter.

I. INTRODUCTION

A novel remote sensing technique based on signals of the Global Navigation Satellite System (GNSS) reflected off the Earth surface, the so called GNSS reflectometry (GNSS-R), was suggested in the nineties for ocean altimetric [1] and scatterometric [2] applications. As investigations progressed, experimental campaigns, dedicated modelling activities and the analysis of actual spaceborne data sets have expanded the range of applications of the GNSS-R, which so far have generated two special issues of the IEEE Journal of Selected Topics in Applied Earth Observations and Remote Sensing (J-STARS) [3], [4], an IEEE GRSS tutorial [5] and dedicated book chapters [6]–[8]. The cryosphere and polar areas are some of the new scientific targets of this technique.

Komjathy *et al.* [9] pioneered the research on GNSS-R for cryosphere information acquiring and analyzing data collected from airborne instruments. Their experimental results indicated the potential of reflected GNSS signals to provide information on the presence and condition of sea and fresh-water ice, as well as the freeze/thaw state of frozen ground. The Arctic sea ice data set was analyzed afterwards confirming its potential for ice scatterometric applications in [10], [11]. Reflected signals captured from a GNSS Radio Occultation satellite were preliminary inverted to sea ice and Greenland ice sheet altimetry under very slant geometries [12], while data obtained from a dedicated GNSS-R spaceborne experiment demonstrated the feasibility of acquiring signals reflected off sea ice from space at near nadir geometries [13], [14], even when a relatively low gain antenna was used. Dedicated coastal experiments based in Greenland [15] firstly investigated polarimetric responses of GNSS reflection off sea ice [16] and the trackability of the electromagnetic carrier phase after sea ice reflections, enabling precise phase-delay altimetry of the coastal ice [17]. Mid latitude snow properties were found to be characterized from reflected signals unintentionally captured in ground-based geodetic GNSS stations (e.g. [18]–[20]), while the interaction of GNSS signals with the dry snow in polar ice sheets was theoretically tackled in [21] and experimentally investigated [22]. Penetration depths down to a few hundred meters were reported in Antarctica ice sheet.

More recently, new sets of GNSS-R data have enabled to test some of these polar remote sensing concepts from spaceborne scenarios. One of the data sets has been acquired from the Soil Moisture Active Passive (SMAP) mission, as the transmitting chain of its L-band radar failed and the receiving chain was tuned to collect GNSS reflected signals. The novelties of SMAP GNSS-R over other GNSS-R missions are the reception in two polarizations (two orthogonal linear base) and the high gain of its 6 meter antenna. These data have enabled GNSS-R to detect the land surface freeze/thaw state [23] and distinguish between ocean water and sea ice through the polarimetric response [24]. SMAP GNSS-R data were opportunistic, limited and are not available to the community, and they mostly cover continental areas (target of the SMAP mission). On the other hand, the UK TechDemoSat-1 (TDS-1) polar satellite operated a GNSS-R payload in a 2 out of 8 days cycle since July 2014 to July 2017, the data were open but the antenna was in a single polarization and of much moderate gain (13 dBi). The extensive sets of TDS-1 data over the poles have resulted in ice sheet altimetry studies [25], different algorithms to detect sea ice [26], [27], to estimate sea ice concentration [28], to perform sea ice altimetry using the group-delay of the reflected echo [29] or by using its carrier phase delay [30]. The latter reports negative correlation between the ice thickness and the altimetric solution, both presenting variations of the same order of magnitude. These findings might be an indication that the altimetric response comes from the ice-water interface (draft), which if confirmed would suppose a new and complementary way of extracting sea ice thickness.

The GNSS-R technique is proposed in a polar-science oriented mission [31], in response to the ESA EE9 Revised Call [32]. Unlike the GNSS-R spaceborne payloads deployed so far, the GNSS Transpolar Earth Reflectometry exploring system (G-TERN) proposes to implement a different acquisition technique to access the full GNSS transmitted bandwidth and a system of antennas tailored to altimetric applications. This approach follows the steps of the ESA's Passive Reflectometry and Interferometry System In-Orbit-Demonstration (PARIS-IOD) [33] and the ESA's GNSS Reflectometry, Radio Occultation and Scatterometry on board the ISS (GEROS-ISS) [34], both missions focused on

GNSS-R altimetry and having successfully passed their irrelative industrial feasibility studies (Phase-A). G-TERN was proposed by a multidisciplinary international team of 33 scientists and engineers experts in GNSS remote sensing, polar sciences, oceanography, hydrology and space technology, to attempt to contribute solving a relevant scientific problem within the constraints of the ESA EE9 ‘Revised Call’. The call, issued in December 2016, asked for missions to address a relevant Earth scientific problem, while fitting in a reduced budget and short implementation time, using innovative techniques but based on proved concepts. Different aspects of the mission concept and suggested implementation are detailed in the following sections, together with the simulation exercises to assess the performance of the system.

II. SCIENTIFIC OBJECTIVES

Advancing the understanding of the cryosphere in a changing climate has been identified as a ‘Grand Challenge’ by the World Climate Research Programme (WCRP). Components of the cryosphere play a central role in several processes that remain an important source of uncertainty in projections of future climate change. Examples of such processes are the prospect of an ice-free Arctic Ocean in contradistinction to Antarctic sea ice increase; the role of ice-sheet dynamics in amplification of Greenlands and Antarcas contribution to the global sea-level rise; the fate of mountain glaciers providing fresh water to hundreds of millions of people worldwide; and the strength of positive feedbacks between the warming climate and natural emissions of greenhouse gases from the thawing permafrost [35]. Furthermore, a particular issue has emerged in past Intergovernmental Panel on Climate Change (IPCC) Assessments [36] as topic of considerable uncertainty: the ability of models to simulate recent declines and future changes in sea ice. Recent studies have linked changes in snow and ice to circulation changes, weather extremes, and the obvious impacts on terrestrial and marine ecosystems, which create a great sense of urgency [37]. For the reasons discussed below, G-TERN primarily aims to contribute to understanding sea ice processes, their evolution and interactions with the rest of the climate systems.

The sea ice cover is a crucial component of the polar and global systems, influencing and influenced by changes across a wide range of temporal and spatial scales. A recent attempt to quantify the overall impact of sea ice on the current climate found that sea ice and anthropogenic greenhouse gas emissions are of similar magnitude in terms of their influence on the global heat budget [38]. Sea ice plays a number of key roles in moderating global climate, not only by influencing the planetary heat budget but also by interacting with the oceanic and atmospheric circulation systems as well as the terrestrial environment [39]–[50]. These complex feedback mechanisms link the atmosphere, sea ice, ocean, seafloor, and land, and many of them are not yet fully understood [46]. For example, winds and ocean currents can alter the distribution of sea ice. These changes

in the sea ice cover can then affect large-scale circulation patterns in the atmosphere (e.g. [41], [43]) and the ocean (e.g. [39]), which in turn may impact weather and the global climate system. Moreover, the Southern and Arctic Oceans are different dynamic systems. On one hand, surface waters in the Southern Ocean have experienced less warming than has been observed in other areas. On the other hand, the Arctic sea ice has decreased rapidly, and recent reports indicate that it could be largely free of sea ice in summer as early as the late 2030s, only two decades from now.¹ Climate models face a challenging paradox when attempting to predict the evolution of the polar systems: whereas the historical trend in Arctic sea-ice extent is underestimated by the models, the simulated downward trend in Antarctic sea-ice extent is at odds with the small observed positive trend that has been further complicated by unusual weather events shrinking Antarctic sea ice in the last season. The polar sea ice paradox remains one of the most challenging science issues to be resolved regarding climate change science [51]–[54].

Arctic sea ice prediction has inherent limitations due to the stochastic nature of the climate system. These limitations are poorly understood, especially across the full range of timescales and variables of scientific and societal interest. Advances in understanding these limitation and in the seasonal-to-decadal predictive capabilities require enhancements of our theoretical, observing, and modeling capabilities [55]. The recent decline in the extent of Arctic summer sea ice has resulted in a dramatic shift in its composition, first-year sea ice become dominant over multiyear sea ice (e.g. [47], [55], [56]), which reduces its size, remains younger and thinner [57], [58]. This rapid change to a new state is likely to have important implications for sea ice variability, predictability and even Arctic halogen photochemistry [59]–[62]. In the face of this significant transition, there is the need to identify and understand whether and how key parameters are properly modeled. Currently, sea ice models’ treatment of ice dynamics and thermodynamics employs parameterizations that were often developed based on observations taken in a primarily multiyear ice regime, and they may not apply in the new state, in which the surface albedo heat balance are profoundly altered. Moreover, it is likely that if, as expected, the substantial ice retreat continues and the remaining ice transforms to a largely seasonal character, the oceanic and atmospheric circulation and thermodynamic structure will respond to the changes in the surface state, affecting large-scale patterns. The regime shift may also cause changes in physical and biochemical processes that have not been adequately accounted for in current models.

Over Antarctica, it is not yet well established quantitatively the relative contributions from multiple mechanisms to explain the observed variability and the slight increase in overall Antarctic sea ice extent, as many local,

¹AMAP Snow, Water, Ice and Permafrost. Summary for Policy-makers. This document presents the policy-relevant findings of the AMAP 2017 assessments of snow, water, ice and permafrost in the Arctic (SWIPA), 2017.

regional, and global processes influence sea ice growth and melt. Different theories suggest different potential explanations to this phenomena, including the role of feedbacks between the ocean and sea ice; possible tropical Pacific and Atlantic teleconnections; and effects of winds and ocean currents controlled by topography and bathymetry [63]. Understanding the mechanisms and processes driving sea ice variability and trends in the Southern Ocean is limited by the lack of proper observations to quantify sea ice characteristics and processes [63], [64]. Changes in the Antarctic, where average sea ice extent is approximately 20% greater than in the Arctic [64], could result in relatively significant changes to planetary albedo. Furthermore, feedbacks between sea ice production and ocean water temperature and salinity may play a role in determining the stability of Antarctica's massive sheets of glacial ice [65]–[67]. Understanding sea ice variability and trends may thus be important for anticipating the rate of ice sheet melt and sea level rise in the coming decades. Process-based understanding is critical for improving our knowledge of the mechanisms of Antarctic sea ice variability, but they require high-resolution atmosphere and ocean products, especially for resolving some of the features such as eddies, polynyas/ice formation, and katabatic winds/cyclogenesis. These complexities demand major advances to observe the Southern Ocean.

Furthermore, extreme events such as polar lows and anomalous winds due to dipole anomalies [47] may combine with preconditioning and ice-albedo feedback to result in abrupt changes, e.g., a large decrease of sea ice in a short time [57], [68]–[71], with decadal impacts. For example, drastic loss of perennial sea ice owing to persistent wind patterns in 2005 and 2007 [42] may influence the long-term sea ice trends. Models can simulate extreme events of this type (e.g. [72]) but the accuracy of how simulated extreme events modify key parameters of the ice needs to be further assessed.

The Arctic Marginal Ice Zone (MIZ) and the Antarctic Frontal Ice Zone (FIZ) are the areas where sea ice is more exposed to weather and ocean phenomena [63], together with advection zones (AZ) in coastal areas. Moreover, near coastal areas, warm waters from river discharge can bring significant heat to melt sea ice effectively. From Arctic rivers, massive discharges carry an enormous heating power of 1.0×10^{19} J/yr for each 1°C of the warm river waters above freezing [49]. River discharges, which vary weekly, rapidly warm up sea surface temperature by more than 10°C at the scale of ~ 150 km away from the coast and 2°C as far as ~ 450 km out in the ocean [49]. These phenomena not only melt the sea ice, but also alter the air-sea interactions in the boundary layer through variations in the air-sea temperature difference that impacts the Monin-Obukhov length and the friction velocity. The ice in these areas is therefore highly dynamic, and proper understanding and quantification of its rapid response to quick evolving episodes of winds, waves, polar lows and discharge episodes would enhance our knowledge of the interactive mechanisms leading to the ice

variability (see Figure 1). This could be achieved with observations of these forcing phenomena, together and synchronized with frequent quantification of ice production and deformation processes, including divergence in polynyas near the coast, evolution of the MIZ and FIZ formations, and ice mass variations.

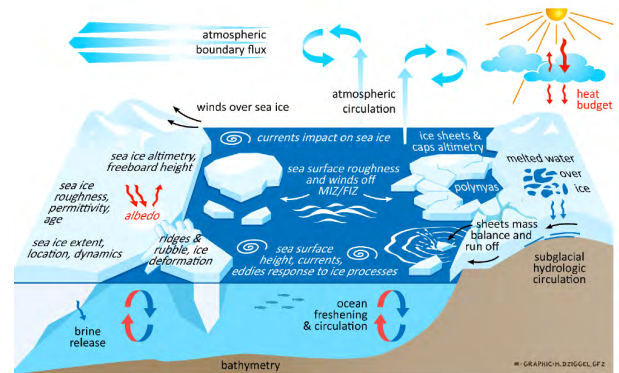


FIGURE 1. Sketch of different processes and interactions involving the cryosphere. G-TERN aims to improve understanding of the sea ice related processes and interactions at regional to climate scales, with focus on highly dynamic variations (ice production, deformation, melt), their driving forces and feedback mechanisms, including extreme events, ocean and atmospheric circulation. Other processes of the cryosphere related to sea ice snow cover and brine content, ice sheets and caps, hydrology and snow, biochemistry, and permafrost are secondary objectives of the G-TERN mission. Figure from G-TERN EE9 Proposal.

Understanding of sea ice changes critically depends on local and regional thickness distribution. Apart from thermodynamic growth (modal growth) and melt, ice thickness and changes of sea ice extent are governed by the drift and deformation of the ice (dynamical growth). Changes of Antarctic sea ice extent critically depend on northward ice advection and the formation of sea ice in coastal polynyas. Ice thickness variations result from changes in ice convergence, which thickens ice by rafting and ridging. The latter process is also manifested by large changes of surface roughness and scattering properties. These pieces of information could contribute to resolving the Arctic-Antarctic sea ice paradox, improving the re-parametrization of the sea ice processes in climate models and therefore enhancing the short and long term predictability of sea ice trends and other valuable sea ice related parameters. This knowledge would also have potential to find proper proxies to extend the records of sea ice to before the satellite era, a key element to fully understand the trends currently observed [64]. Acquiring this knowledge requires observational capabilities to capture the highly dynamics of the sea ice, quantify their quick changes in ice production and growth, degradation and melting processes, their mass variations in rapid intervals, and the way they interact with the surrounding ocean and weather. These observational capabilities do neither exist currently nor in planned future missions.

For the reasons above, the primary objective of the G-TERN mission is to quantify crucial characteristics, processes and interactions between the cryosphere and other

Earth system components in order to advance the understanding and prediction of climate change and its impacts on the environment and society. The mission addresses the World Climate Research Programme (WCRP) Scientific Challenge on Melting Ice and Global Consequences, including the rapid transition towards an ice-free Arctic Ocean and its impact on the large-scale atmospheric circulation, extreme weather and climate conditions. G-TERN also aims to contribute resolving the challenging polar sea-ice paradox. These objectives are articulated through three key questions:

- **MAIN OBJECTIVE, QUESTION-1:** In a rapidly changing Arctic regime and under the resilient Antarctic sea ice trend, how will highly dynamic forcings and couplings between the various components of the ocean, atmosphere and cryosphere modify or influence the processes governing the characteristics of the sea ice cover (ice production, growth, deformation and melt)?
- **MAIN OBJECTIVE, QUESTION-2:** What are the impacts of extreme events and feedback mechanisms on sea ice evolution?
- **MAIN OBJECTIVE, QUESTION-3:** what are the effects of the cryosphere behaviours, either rapidly changing or resiliently stable, on the global oceanic and atmospheric circulation and mid-latitude extreme events?

The secondary objectives of G-TERN address complementary cryospheric science questions as well as other climate relevant applications. The first secondary objective aims to demonstrate the suitability of the G-TERN mission technique, the reflectometry using navigation signals (GNSS-R), to sense other cryosphere products. If successful, these products would complement the investigations on the main objective with potential to become a breakthrough in other cryospheric questions.

- **SECONDARY OBJECTIVE-1, COMPLEMENTARY CRYOSPHERE PRODUCTS:** Which is the potential of the G-TERN techniques to extract geo-physical information about
 - snow cover over sea ice, its thickness and density;
 - sea ice permittivity, density and/or brine content;
 - sea ice surface melt onset and melt pond fraction;
 - distinction between modal (thermodynamic) and dynamical (deformation) growth of the sea ice;
 - ice sheets and large caps, their surface elevation changes, mass balance, run offs, melting episodes, surface and sub-surface snow properties;
 - permafrost active layer changes, freeze and thaw phase, surface deformations;
 - seasonal snow in mid latitudes, its thickness and snow properties; and
 - glacier evolution?

Finally, the last secondary objective addresses selected contributions of the land component into the global warming scenario. In particular, G-TERN aims to contribute quantifying the biomass and its variations as well as the extension

of the flooded areas within wetlands (i.e. inundated wetland extent), including densely vegetated ones (e.g. forested swamps). Both variables play essential roles in the water and energy cycle, linking hydrological, ecological and atmospheric carbon sciences.

- **SECONDARY OBJECTIVE-2, LAND COMPONENT:**
 - How the water coverage is changing in wetland areas (particularly swamp forests) in view of the rapid rate of wetland collapse?
 - What is the role of wetlands in methane emission processes, especially in view of new pathways for methane emissions that can be potentially identified with frequent observations including densely vegetated and forested regions?
 - How regional conditions, especially soil moisture, impact wetland inundation dynamics and affect regional atmospheric patterns (e.g., by altering the Bowen ratio) that in turn impact the transport and distribution of methane emitted from wetlands?

A. OBSERVATIONAL REQUIREMENTS

The observational requirements of G-TERN are driven by the primary objectives. To properly contribute answering the primary scientific questions, G-TERN will measure key parameters of the sea ice, the oceans and the atmosphere with frequent and dense coverage over polar areas, becoming a ‘dynamic mapper’ of the ice conditions, ice production and loss in multiple time and space scales, and surrounding environment. Frequent mapping is very important for better observing and understanding multi-scale interaction processes. For example, the causes and effects of deformation events on changes of the sea ice mass balance. Global interactions and their impacts will also be explored through generating global datasets of ocean and atmospheric observations suitable for assimilation in numerical models.

Given that at polar areas the rapid and violent weather systems have typical temporal scales of days to a week, river discharge change significantly over weekly scales, and given that these events are relevant target phenomena to be observed (QUESTION-1 and -2), their temporal scales constraint the time resolutions of G-TERN over polar areas to a few day periods. Particularly important during the spring-summer transition is the albedo switch from high to low values that crucially impact the surface heat balance and thus sea ice melt processes. Such albedo switch may occur on a weekly temporal scale [73], and thus demanding sub-weekly (~3 days) observations to account for the Nyquist temporal sampling requirement. The albedo change is dependent on different distribution of melt pond fraction over the synoptic sea ice classes including first-year (seasonal) and multi-year (perennial) sea ice in the Arctic [74], and over different Antarctic sea ice classes [63] depending on the sea ice roughness, including the FIZ with spatial scales as little as 100 km [63]. Indeed, understanding the causes and effects of deformation events on changes of the sea ice mass balance requires rapid repeat observations over the

TABLE 1. Observational requirements to address G-TERN's primary scientific objectives (level-3 products' requirements).

Variable	Requirements on geophysical variables for the PRIMARY OBJECTIVE (Q1-Q3).			
	Scope	Spatial resolution	Temporal resolution / coverage	Accuracy within spatio-temporal resolution
Sea ice altimetry	P	30 km	3 days	10 cm
Sea ice roughness	P	30 km	3 days	10% dynamic range (0.0015 mss)
Ocean surface altimetry	P	30 km	3 days	10 cm
	G	0.5°	10 days	10 cm
Ocean surface roughness	P	10 km along-track	1 second / 3 days	0.002 mss or 10%
	G	10 km along-track	1 second / 10 days	0.002 mss or 10%
Time life	5-10 years, launch 2025			

same regions. Furthermore, these processes are the ones that determine the ice behavior on longer time scales and in larger regions. For properly mapping these small polar mesoscale storms (of 100 to 500 km longitudinal scales) as well as their effects into the sea ice, submesoscale horizontal resolutions are required. Given the various spatial scales of sea ice and ocean characteristics, a spatial resolution better than 50 km can account for the Nyquist spatial sampling requirement to address process at the 100-km scale. Moreover, on ~ 30 km scale, sea ice can be considered a continuous fluid and sub-scale processes will accumulate and integrate on the grid scale to cause measurable changes that can be interpreted with commonly used ice deformation rheologies. Therefore, G-TERN in polar areas shall resolve sea ice properties, ice surface elevation and the surrounding ocean surface at spatial resolutions of the order of 30 km with full polar coverage within 3 days. To distinguish between different seasonal ice the sea ice surface elevation measurements should have accuracies of the order of 10 cm within the spatio-temporal requirements.

At middle latitudes and the tropics, G-TERN should contribute to understand the effects of changes in the cryosphere on the global ocean circulation and mid-latitude extreme events (QUESTION-3). The extreme events must be studied at mesoscale, as well as the global circulation feedback mechanisms, which can involve intermediate scales. For instance, mesoscale features such as eddies mediate the transport of heat, salt and carbon by mixing densities and the connection of the surface water to the deep ocean through the thermocline (e.g. [75], [76]). Therefore, G-TERN shall resolve mesoscale ocean features globally, with spatial resolutions of 0.5 degree and full coverage within 10 days. These mesoscale ocean features have signatures at the decimeters level, reason for which the accuracy within the global spatio-temporal resolution is requested at 10 cm in sea surface elevation, too. For both surface ice and ocean roughness, the accuracy of the measurement should be at 10% level of its dynamic range. Hereafter we will express the surface roughness parameter as the mean square of the surface slopes (mss). The requirements of these geophysical variables are summarized in Table 1, where scope 'P' means polar areas and 'G' is for the rest of the globe (middle latitudes and tropics).

The G-TERN would be launched in 2025, with a nominal lifetime of 5 years and expected extension to cover 10 years

of observations. G-TERN operating for a period of five years would provide a large data set obtained during potential critical years of the evolution of the Arctic, 2025-2030, when sea ice reduction is projected towards nearly sea ice-free Summers, and it would also acquire sufficient information to enhance our understanding of the Southern Ocean trends and mechanisms. Models that best match historical trends project a nearly ice-free Arctic in the summer by the 2030s [77], [78], with some studies pointing that this might happen before 2030 (during G-TERN nominal lifetime) [79]. Other analysis predict the transition later on, from mid 2030s to before 2050 [80], [81]. Extending the mission timelife to ten years would increase the chances to explore this transition and its potential associated tipping point - a point beyond which the system abruptly changes into a different climatic state. The 'dynamic mapping' (e.g., 3 days) capabilities of G-TERN might become essential to properly quantify the changes and comprehend any new chain of interactions or evolved feedback mechanisms that might occur under the new conditions. Exploring the global responses to these changes would also benefit from an extended lifetime of the mission, as feedbacks between different spheres might include components at longer time scales.

III. MISSION CONCEPT

The G-TERN mission is based on the combined application of the GNSS Reflectometry (R) and Radio Occultation (RO) remote sensing approach, which has been recently investigated successfully and in detail as heritage from the ESA funded GEROS-ISS mission Phase A studies [34]. The GNSS-R component will apply grazing carrier phase-delay altimetry [82] and group-delay/Doppler altimetry (e.g. [33], [83]), as well as scatterometry and polarimetry over ice, water and land surfaces using the interferometric GNSS-R (iGNSS-R) approach. An overview of the different measurement techniques is provided in Section IV with more details about the iGNSS-R concept in Section IV-A. G-TERN is proposed as a single-satellite mission in a near-polar sun-synchronous, 6a.m/6p.m. orbit at 600 km altitude. The selection of a sun-synchronous orbit is not a strong scientific requirement for the polar observations (other near polar orbits would perform as well), but it is a suitable choice to minimize the effects of the strongest ionospheric scintillations phenomena over tropical areas, and will suite the high power and heat dissipation demands (as shown in Section V). The

launch is planned in 2025 and the nominal mission duration is five years. Table 2 summarizes the main mission characteristics.

TABLE 2. Overview on the main G-TERN mission characteristics.

Sensor:	iGNSS-R + GNSS-RO 12 simultaneous beams L-band, 2-frequencies 2-polarization
Orbit Orientation:	Near-polar
Optimal Orbit:	Sun-synchronous 6AM/6PM
Orbital height:	600 km
Time life:	2025-2030/2035

G-TERN is proposed as a box-shaped satellite with the OHB LEO platform, of around 800 kg dry mass. The payload is dominated by the beamforming capable antennas, which allow 12 simultaneous reflectometry observations at virtually any direction in two frequencies. The payload is separated from the platform by an isostatic mechanical interface. The spacecraft is compatible with a VEGA-C dual-launch and the possibility to fit as a secondary passenger within the VESPA adapter will be considered during the next phases, as soon as a detailed specification of the adapter is available. After presenting the measurement techniques (Section IV), further details on the platform and payload can be found in Section V, while the expected performance is analyzed in Section VI.

IV. GNSS MEASUREMENT TECHNIQUES

This section presents a qualitative overview of the measurement techniques suggested for G-TERN. For detailed descriptions and formulation the readers are pointed to the available textbooks and tutorials [5]–[8]. The basic observation concept of the G-TERN mission is based on the innovative use of L-band navigation signals for remote sensing (GNSS remote sensing). Such ground and satellite GNSS based Earth observation techniques are already widely and operationally used since several years for atmosphere sounding. Outstanding example for this application is the routine assimilation of related data products to improve regional and global weather forecasts, which was started in 2006 (e.g. [84]). But the GNSS atmospheric data are also exploited by a large international community of geodesists, atmospheric scientists and climate researchers for atmospheric research including studies of the global change (e.g. [85]–[88]).

In the recent years the international research in GNSS remote sensing has focused on the GNSS reflectometry (e.g. [89]–[91]), which complements the atmosphere sounding techniques, and exploits navigation signals, reflected off the Earth to derive geophysical parameters of the water, ice and land surfaces (e.g. [1], [2], [5], [22], [27], [33], [92]–[96]). The advantages of the GNSS-R technique are (1) its synoptic and high-temporal resolution capabilities, derived from the multiplicity of GNSS transmitters which provide reflected signals simultaneously (Figure 2);

(2) the passive nature of the receiver, as the transmitting global navigation infrastructure is deployed and maintained by third parties; (3) its truly ‘all weather’ operability even in severe weather like cyclones, required for navigation purposes and at multiple L-band electromagnetic frequencies; and (4) represent a novel exploitation of signals of opportunity, with all surface and different types of climatic observations scalable by the number of ever-growing GNSS satellites. Numerous successful ground and airborne experiments demonstrated already the large and versatile potential of this innovative space geodetic technique for Earth Observation (e.g. [15], [82], [97], [126]). Recently also the first dedicated satellite based experiments are in preparation, as ESAs Geros-ISS [34], or have already successfully been launched, as the UK TechDemoSat-1 (TDS-1) [91] and NASA’s CyGNSS [99].

The GNSS-R missions in orbit (TDS-1 and CyGNSS) operate under the acquisition technique used in most of the GNSS navigation applications: the weak GNSS signals are cross-correlated with a clean replica of the publicly available modulation codes. This approach, called hereafter ‘clean replica’ or ‘conventional’ (cGNSS-R) is cheap and easy to implement, it does not require large directive antennas but can only be applied to the publicly available codes. These codes (e.g. GPS Coarse Acquisition, C/A) are narrow band and therefore with limited ranging performance. Ranging performances are crucial in altimetric applications, and a way to increase the received bandwidth is to use the whole transmitted one, including the encrypted codes. These codes present broader bandwidths, of the order of 10 times wider than the publicly available modulations. As they are not public it is not possible to synthesize clean replicas of them and alternative approaches are needed. A possible approach is called interferometric GNSS-R (iGNSS-R), for which the reflected signals are cross-correlated against the direct ones. Because the direct signals are noisier than the idealized clean replicas, this approach increase the noise unless highly directive antennas point to each of the reflection points and to each of the transmitting sources. Highly directive antenna beams, each one pointing to a single satellite or specular point also help discriminating the different received satellite signals (traditionally discriminated and identified through the code itself). The iGNSS-R approach with high directive antennas has sufficiently large SNR to take advantage of the full bandwidth and enhances the altimetric precision figures by factors between 2 and 6 [96], [100]–[105], while its spatial resolution is enhanced from 25 km in cGNSS-R to 10 km in iGNSS-R (it depends on the geometry, observable, retrieval technique and integration time). The iGNSS-R approach was the one selected for mission proposals such as the PARIS IoD [33], the Geros-ISS [34], and the ‘Cookies’ [106], but none of them orbited yet. Geros-ISS primary science objective focused on altimetry, and it successfully passed two independent industrial Phase-A studies. G-TERN, like Geros-ISS, envisages iGNSS-R altimetry both using group-delay observables (range information extracted from the

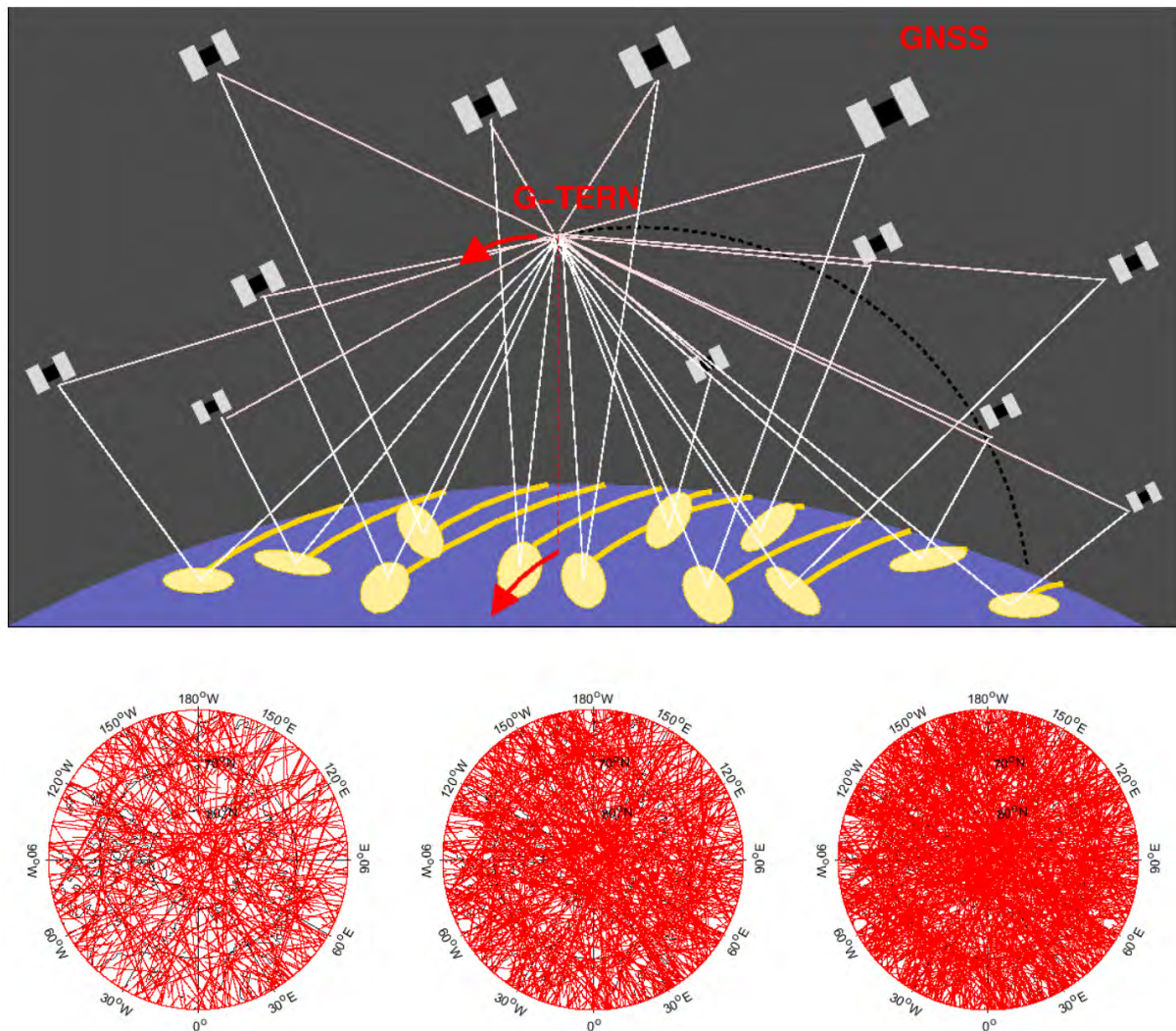


FIGURE 2. Top: sketch of the GNSS Reflectometry multi-static observation concept: from a single receiver it is possible to collect signals reflected from multiple GNSS transmitters simultaneously. Each transmitter-surface-receiver link results in an independent measurement of surface characteristics around its specular point. As the receiver moves, so the specular points do, each tracing a ground track of observations. G-TERN implements capabilities for 12 simultaneous reflections (Figure adapted from [7]). Bottom: examples of the specular locations of the G-TERNs 12 simultaneous reflections, at 1Hz rate, accumulated during 1 day (left), 2 days (centre) and 3 days (right) over the North pole. The distribution of reflection points does not follow a repeatable pattern, but it keeps the latitudinal statistics.

envelope of the cross-correlation function) and phase-delay observables (carrier phase information when the scattering is essentially coherent). Neither TDS-1 nor CYGNSS have implemented these capabilities.

The primary observable of the GNSS-R is the ‘delay-Doppler map’ (DDM) or its central Doppler slice, called ‘waveform’. In iGNSS-R the waveform is the cross-correlation, in the delay domain, between reflected and direct line-of-sight signals, after they have been aligned both in delay and frequency based on a-priori information of the transmitter, receiver locations and velocities, and the location of the reflecting surface. If the surface scatters predominantly in diffuse regime, the waveform follows the bi-static radar equation with a Woodward ambiguity function (WAF) given by the autocorrelation of the combination of the GNSS

transmitted codes and the sinc-exponential Doppler filtering [93, eq. 27]. In some Earth surfaces, the scattering diffuses the signal over wider areas, the ‘glistening zone’. This zone span across areas beyond the narrow stripe filtered in by the sinc-exponential. Therefore, the bi-static radar equation can also be evaluated for Doppler frequencies other than the one of the specular point. When the reflected energy is mapped into a suit of delay lags and Doppler frequency cells, the resulting observable is called ‘delay-Doppler map’ (see Figure 3). The DDMs acquired from TDS-1 GNSS-R experiment show clear distinctive features when the signals are scattered off the rough ocean or off areas covered by sea ice. These differences have been confirmed by several peer-reviewed studies [26]–[30], which indicate that GNSS reflections off sea ice mostly present features of coherent rather than diffuse

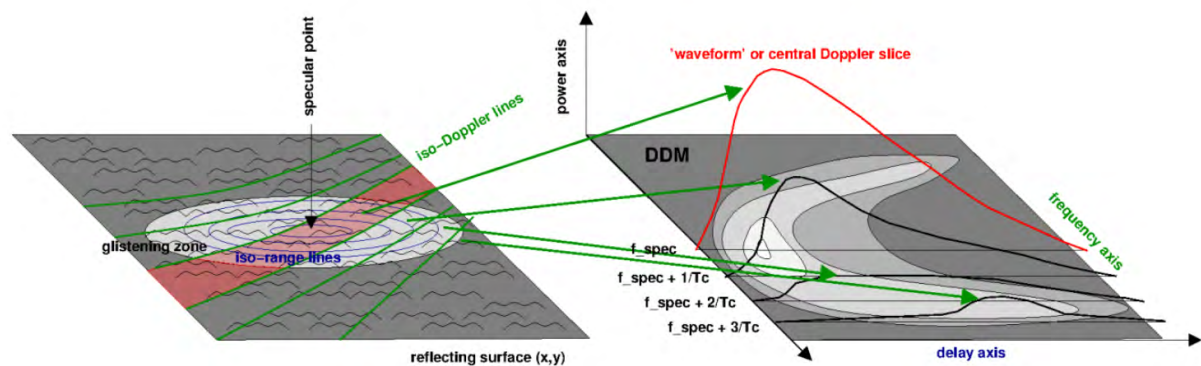


FIGURE 3. The primary GNSS-R observable is the delay-Doppler map (DDM) and its central frequency slice, called waveform. Figure adapted from [7].

scattering. When the coherent scattering predominates, as it also happens over calm waters and even land, the waveform follows the criteria and models in [107]–[111]: the DDM essentially shrinks to the WAV shape. It is also important to note that when the scattering is coherent, the carrier electromagnetic signal can be tracked. Then, the time series of its phases mainly evolves with the geometry of the observation and carrier phase-delay altimetry is possible to achieve (see Section IV-B).

The resolution of the GNSS-R products depends on many factors, such as the observable being used (large portion of the DDM, or the peak power, or the leading edge of the waveform, etc), the nature of the scattering (diffuse or specular), the geometry of the bi-static observation (orbital height, incidence and azimuth angles) and even the coherent integration time. The baseline techniques to be applied in G-TERN will generally rely on the leading edge and near-peak observables, which correspond to the resolution of the specular WAF, its projection onto the surface. For typical coherent integration times of 1 millisecond, the central WAF is mostly limited by the ellipse of points on the surface suffering delays with respect to the specular point of the order of one chip of the GNSS modulation. In iGNSS-R, this is approximately a chip of 30 m range, which projects ellipses of sizes ~ 10 km. When the scattering is coherent (over most of sea ice), the peak of the signal comes from the 1 st Fresnel zone, projecting ellipses of a few to several hundred meters (geometry dependent). Indicative values as function of the elevation are given in Table 3 for the near-nadir field of view. At grazing angles of observation the scattering is specular, and the Fresnel zones elongates between 0.5 km to 5 km.

A. iGNSS-R GROUP-DELAY ALTIMETRY

GNSS-R altimetry is the determination of the Earth's surface elevation using GNSS reflected signals [1]. Most of the GNSS-R altimetric developments have been done over the ocean [102], [112]–[116], but the bi-static altimetric measurement principles used over the ocean are applicable and also

TABLE 3. Approximate spatial resolutions of G-TERN baseline observations in the near-nadir field of view (incidence angles $\leq 45^\circ$), and corresponding to one snap-shot measurement.

Approximate spatial resolutions of G-TERN baseline (snap-shot) observations			
	Incidence 0 deg	Incidence 30 deg	Incidence 45 deg
Diffuse scattering:	6 km	6-7 km	7-10 km
Specular scattering:	340 m	370-430 m	410-580 m

valid for altimetry over any other surface that can reflect enough power to enable precise observables. For GNSS-R, these are typically ocean and also ice (e.g. [17]), although certain land surfaces, inland water bodies, or estuaries can also reflect GNSS signals strongly [109]–[111], [117]. The vertical height of the reflecting surface can be given with respect to a reference value (ellipsoid, mean topography, digital elevation/surface model, etc). The position and velocities of both the transmitting and receiving systems must be known accurately, as the vertical component of the surface location is measured from the total range of the radio-link between the transmitter, the surface and the receiver. The central point around which the signal is reflected is defined as the 'specular point', which follows the Snell's laws of reflection. Potentially, a single receiver could measure the reflected range corresponding to each transmitter in view, meaning they all could be solved into the altimetric retrievals for each of their specular points (synoptic capabilities in Figure 2). The number of simultaneous GNSS transmitters in view, from Low Earth Orbiter (LEO) altitudes was of the order of 40 for GPS and GLONASS constellations as in 2012 [7]. This number can be easily doubled when Galileo and BeiDou will be fully deployed by 2020. In practice, the number of simultaneous measurements will be limited by the receiver capabilities. G-TERN implements capabilities for twelve simultaneous observations. The GNSS-R measured surface elevation is an averaged value across the measurement area, zone from which the GNSS-R observation is representative. As presented in Table 3, iGNSS-R resolutions approximately correspond to ~ 10 km if the scattering is diffuse.

In group-delay altimetry the observable of interest is the delay (or range) of the reflected signal. In interferometric GNSS-R technique, planned for G-TERN, the delay is understood as the time lapse between the arrival of the reflected radio link and the arrival of the line-of-sight radio link (non-reflected, also called ‘direct’ signal). Among the GNSS community it is common to work with ranges or distances rather than the time lapses needed for the signal to travel them. The term ‘delay’ is then used indistinctly for both concepts, and often expressed in units of length (as range/distance). Given that these measured ranges include systematic effects such as drifts in the clocks, atmospheric delays, or instrumental biases, they should be called pseudo-ranges. As explained before, the GNSS-R observable is the DDM or its central slice, the waveform. The determination of the arrival time of the reflected signal is equivalent to finding the point along the waveform or DDM that corresponds to the reflection off the specular point. Signals reflected off a roughness-free surface (e.g., very calm waters or smooth sea ice) present a non-distorted correlation function, and the specular delay corresponds to the delay of its peak. This is also the case in standard GNSS navigation receivers for determining the arrival time of the line-of-sight signals. In general, though, this does not apply in Earth reflectometry. For rough surfaces such as the ocean or rigged ice, the peak of the waveform is typically shifted from the specular delay because of the surface roughness, which induces scattering off surface elements around and even away from the specular point. Then, the arrival time of the shortest-specular-delay corresponds to some point between the rising of signal power and its peak, an unknown point along the leading edge of the waveform. Several approaches have been suggested to determine this point (e.g. [102], [103], [105], [118]), among others, the peak of the first delay-derivative of the waveform, a certain fraction of its power, or fitting a theoretical model (e.g., match filter).

The group-delay altimetry has been tested from ground-based and airborne campaigns, for both conventional GNSS-R and interferometric GNSS-R. The experiments have applied the same principles, regardless of the acquisition approach (cGNSS-R vs iGNSS-R), being the main difference between them the bandwidth (thus range resolution) of the signals involved in the processing. The improvement in precision in iGNSS-R compared to cGNSS-R is in the range 2 to 6 [96], [100]–[102], [105]. Airborne iGNSS-R experiments have reported precisions in the range of 0.25 to 0.6 m in 10 seconds observations [119], largely limited by the noise of the aircraft trajectory (see Figure 4), which agrees with the precision predicted by the theoretical models evaluated at these airborne scenarios [102], [105].

Group-delay spaceborne altimetry has also been reported from TDS1 satellite, over ocean and sea ice surfaces. Because TDS-1 does not implement the interferometric capabilities, the results correspond to cGNSS-R. Over smooth sea ice in Hudson Bay the reported precision is 0.96 m in 0.5 seconds and 3.5 km sampling [29]. Over open ocean, [118] reports

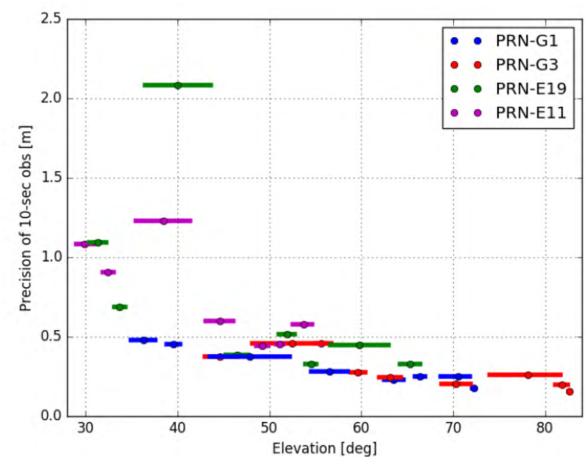


FIGURE 4. Precision obtained in an iGNSS-R airborne campaign flying at ~3000 meter altitude over the Baltic Sea under variable wind conditions between 6 and 15 m/s, for GPS PRN1, PRN3 and Galileo PRN19 and PRN11. The values obtained from Galileo satellites around 40° are due to contamination from other satellites caused by the limitations of this particular beamformer to get a proper separability in such particular events (unpublished Figure from [119]).

group-delay cGNSS-R precisions of the order of 7 to 8 m in 1 second observations, in agreement with precision predicted based on models tuned for the CYGNSS mission (very similar to TDS-1) [120], which is not tailored to altimetric applications.

B. iGNSS-R PHASE-DELAY ALTIMETRY

Most GNSS reflections off the Earth surface correspond to diffuse scattering, where the phase of the carrier is too noisy to be tracked and it loses its range information. Nevertheless, at slant to grazing angles of observation (below 30° elevation) the roughness effectively becomes smoother and coherent reflections occur. Signatures of Earth surface reflection based on GPS carrier phase observations at grazing observation geometry have been reported for satellite based receivers within the GPS/MET proof-of-concept mission for GPS radio occultation [121] and aboard the German CHAMP satellite [122]. These observations were achieved with low-gain antennas and state-of-the-art GPS radio occultation receivers without any specific optimization for GNSS reflectometry. A case study done with carrier phase data from CHAMP also presented altimetric retrievals over the Greenland ice sheet and sea ice [12]. The derived surface heights had 0.7 m precision in 0.2 second averaging. Coherent phase delay GNSS-R altimetry is applied within a radio occultation like geometry and is therefore highly synergistic with GNSS-RO measurements, which in parallel provide atmospheric/ionospheric information for the offset reduction/elimination of the coherent GNSS-R measurements itself.

Phase altimetric simulations have been performed for ocean application to prepare for measurements from Low Earth Orbiting Satellites within the GEROS-ISS related scientific study GARCA [34], [123]. The simulation results

show that phase altimetric retrievals are sensitive to anomalies of the ocean topography and that an altimetric precision of 10 cm in 1 second observation is possible in this respect [124]. At angles of elevation below 10° , critical uncertainties were found to be induced by residuals of the tropospheric delay, degrading the precision to about 30 cm. In general, a limit for phase altimetry is set by the diffuse character of L-band reflections off the rough surface that impede the retrieval of coherent phase observations. However, the diffuse reflection limit depends on the surface roughness and the signal incidence/elevation angle. Coastal experiments demonstrated carrier phase delay altimetry for wind speeds up to 10 m/s [125] and significant wave heights < 0.6 m [108]. Airborne experiments revealed the sensitivity of carrier phase retrievals to geoid undulation [126] sea surface topography [82] over rough open waters in the Mediterranean Sea. Figure 5 shows phase altimetric retrievals from an airship experiment. The 20 cm geoid undulation along the 15 km reflection track is resolved with 3–4 cm precision. The phase-altimetric precision relies on a model-based retracking of the signal, using geometric and atmospheric corrections. A general difficulty arises from the apriori unresolved phase ambiguity. A reference height is provided by the nearby tide gauge stations to fix the ambiguity at the crossover point. In spaceborne scenarios, crossover points with reflected GNSS signals from other transmitters and other altimetric sensors would allow to mitigate the uncertainty of the phase ambiguity. The previous coastal and airborne experiments over sea surfaces have shown that carrier phase altimetry works for reasonable range of elevation angles at the reflection point (5° – 30°). At higher elevation angles coherent observations off the wind-driven sea are much less frequent due to diffuse reflection. At lower elevations the tropospheric residual usually impedes precise altimetric retrievals.

The presence of sea ice at the water surface significantly shifts the diffuse reflection limit and improves the phase coherence of L-band observations [17], [128] and phase delay altimetry was conducted with a few cm precision from a 700 m cliff in Greenland [17]. In fact, smooth carrier phase observations have even been obtained at much higher elevation angles ($\sim 50^\circ$ incidence) over smooth sea ice from the TDS-1 mission [30], with preliminary analysis showing precisions of 4.7 centimetres in 20 millisecond observations. In addition to the tracks analyzed in [30], other phase delay data obtained from TDS-1 over sea ice seems to confirm the possibility of tracking the carrier phase when reflected off sea ice surfaces (see Figure 6). Also continental ice sheets yield rather distinct than diffuse reflections [22] that can be suitable for phase altimetry. The ability of phase altimetry to use data at low elevation angles increases the swath significantly compared to near-nadir configurations. An extension of the elevation range from grazing and slant observations also towards higher angles is expected for sea ice and ice sheet altimetry. The reason is the reduced roughness of some types of sea ice and ice sheet surfaces, that yields reduced diffuse scatter and coherent phase observations.

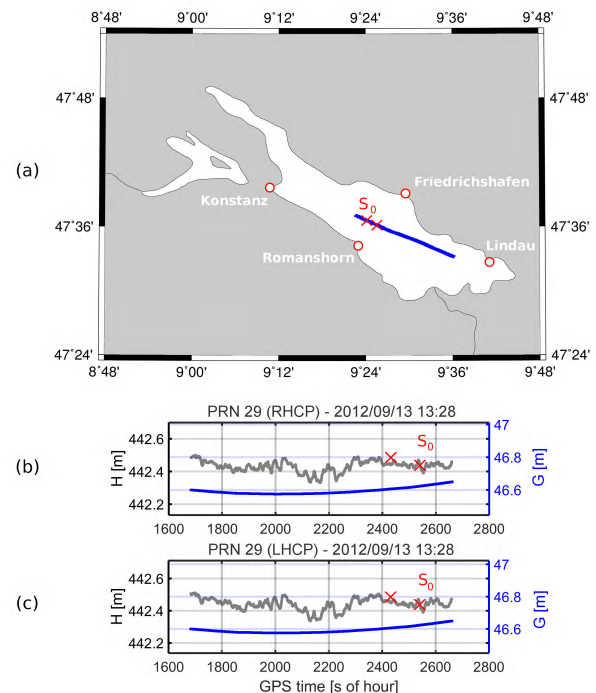


FIGURE 5. Panel (a): Example reflection track (blue) over Lake Constance obtained from a GNSS-R payload aboard a zeppelin. A crossover reference S_0 is indicated which allows to solve the phase ambiguity. The reference is based on lake level estimates from the gauge stations (red circle) nearby. Panels (b) and (c) show the phase altimetric solution (gray) for right- and left-handed polarization retrievals, respectively. Due to crossover referencing the total height level H can be estimated. For comparison, the geoid undulation G along the track is plotted as blue line, taken from GCG05 model [127].

An important question, which requires further investigations, is the L-band signal penetration into the snow cover on sea ice, sea ice itself and ice sheets. In [11] the penetration into sea ice was estimated between 30 and 70 cm, while over dry snow over ice sheets [22] reported reflections from sub-surface layers down to 200–300 meter at Concordia Station, Antarctica. In general, L-band signals are more transparent to snow than other instruments at higher frequency bands, thus representing an advantage to minimize the contamination of the retrievals induced by the snow cover (issues in Cryosat-2 and ICESat/ICESat-2).

C. IGNSS-R SCATTEROMETRY

During the initial stages of the GNSS reflectometry, the target of the incoherent reflection measurements was the wind speed and wind direction (e.g. [129], [130]), when precisions of the order of 2 m/s in wind speed and 20 degrees in wind direction were reported. However, it was soon understood that the wavelengths of L-band signals were sensitive to a combination of other ocean surface parameters, such as wind, swell and wave age, reason for which the term ‘L-band roughness’ was introduced. The mean square slopes, mss—dispersion of the surface slopes—was thus the preferred parameter in some other studies (e.g. [131]–[133]). The ‘L-band roughness’ has

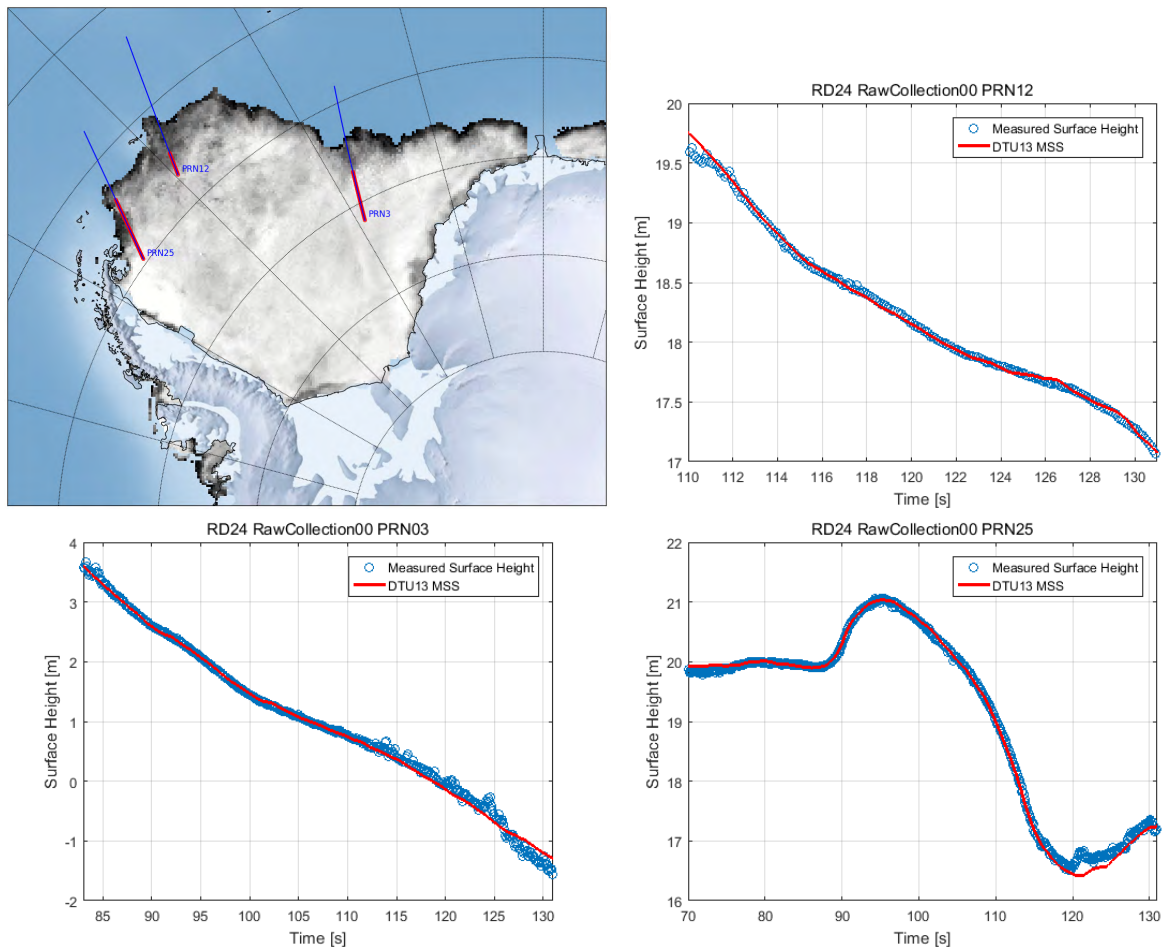


FIGURE 6. In addition to the TDS-1 phase-delay altimetry over sea ice shown in [30], other sets of data provide further evidences of the trackability of the phase in sea ice GNSS reflections. Top-left: Three GNSS reflected tracks over sea ice, acquired in raw data mode by TDS-1 on March 24th, 2015. The red segments correspond to the portions where phase-delay altimetry is applied. Top-right and bottom panels: Carrier phase altimetry obtained with the data sets, and compared to the mean sea surface (DTU13 model). TDS-1 raw data made available by SSTL and processed by W. Li (ICE-CSIC/IEEC).

interest as complementary information required in sea surface salinity measurements performed with L-band radiometry (ESA's SMOS, NASA's Aquarius), as well as potential source of air-sea interaction and dragging, when combined with independent wind estimates.

The previous statements were first supported by a wide diversity of air-borne and stratospheric experiments performed at different altitudes, receiver speeds, instrumental equipments, and analysis techniques (e.g. [129]–[140]). At least eight different techniques were used in the listed references, of different degree of complexity and elaboration, different final product (scalar roughness, directional roughness, non-Gaussian features). Recently, intensive work has been done to extract wind and roughness information from GNSS-R spaceborne missions, such as TDS-1 and CYGNSS, mostly constraining the source of information around the peak of the DDM [90], [141], [142] or inspecting the geophysical informational content in DDM cells further away from the specular [143], [144]. In all these inversion

schemes the starting point is the bi-static radar equation from which the radar cross section or the probability density function of the slopes is inferred. Over the oceans, given the G-TERN specifications one expects similar scatterometric performance as for the CyGNSS mission, with finer spatial resolution (provided by the iGNSS-R technique).

Characterization of sea-ice has been also reported from experimental GNSS scatterometric work [11], [16]. Over ice, mss derived from the decay rate of the GNSS reflected waveforms was also reported as a valuable indicator of the ice surface roughness, as it is linearly related to the standard deviation of the surface elevation [11]. These airborne campaigns showed good agreement with the surface elevation dispersion obtained from GPS reflections and those measured with a lidar aboard the same aircraft. Similarly, an efficient permittivity of the ice, obtained from the received GNSS-R power, correlated with the ice age. A combination of both power and decay characterize the ice age or type. From the TDS-1 spaceborne platform, high accuracy in sea ice detection has

been obtained using DDM observables [26] through investigating the degree of coherence of the waveform extracted from DDM [27] or using neuronal networks [28]. Moreover, the signatures around the peak of the DDM have also been used in these neuronal networks to estimate the sea ice concentration [28], with an overall discrepancy with respect to independent concentration estimates at 1% level.

D. iGNSS-R POLARIMETRY

Polarimetry is a powerful tool for radar remote sensing of our planet. It consists in observing the polarization properties of the electromagnetic wave scattered by the target for any polarization of the impinging wave illuminating the target. The strength of the technique stems from the capability to identify the main scattering mechanisms involved in the interaction of the signal with the target, each mechanism being characterized by its own polarization signature. A number of measurements has to be performed, which consists in observing in two orthogonal polarizations the scattered signals obtained when illuminating the target with as many polarizations of the impinging waves. Depending on the polarization base we consider, e.g., horizontal (H) and vertical (V); or right handed circular (R or RHCP) and left handed circular (L or LHCP), we have to measure HH, VV, HV and VH or RR, LL, RL, LR. Note that we have to measure not only the signal strength (i.e., its power) but also the phase difference between incidence and scattered polarization components. We can translate measurements in the circular polarization base into measurements in the linear polarization base [145]. Some of these measurements can be redundant (e.g., VH and HV in backscattering) or can bring poor information content, so that we can reduce the number of observations keeping the relevant information for target characterization.

The GNSS transmitters radiate a wave whose polarization is nominally RHCP. To carry out a fully polarimetric measurement one should measure the co-polar (R)ight but also the cross-polar (L)eft component due to transmitting antenna polarization imperfections, and then receive at the same time the Right and Left polarized scattered signals in amplitude and phase. Monostatic radars are already exploiting polarimetry from satellites, but G-TERN will provide for the first time polarimetric spaceborne measurements of the signal reflected around the specular direction, with high potential in the cryosphere domain, but also capable to fulfil many secondary objectives of the mission. A critical aspect (especially at RHCP, as it can be several dBs below LHCP) is the sensitivity required to cover the full dynamic range of the signal associated to different surface conditions. This requires a suitable gain of the system and in particular of the nadir-looking antenna. Additional critical aspects can be the effects of surface topography and land cover heterogeneity, especially if they change within the area of the first Fresnel zone. Those are challenges of GNSS-R over land that G-TERN could help to tackle and solve.

For cryosphere applications, the polarimetric response of the scattering is well recognized by the scientific

community as an essential aspect of the remote sensing of sea ice (e.g. [146]). At L-band, the Fresnel reflection coefficients of the circular polarization base show sensitivity to water-ice transition and, in lower degree, also to ice properties through its permittivity changes (e.g. brine content). At relatively low angles of elevation (large incidence) such as the geometries planned for the phase-delay altimetry, these changes affect both the ratio between the power of the two polarized scattered signals (e.g. LHCP/RHCP) as well as their phase shift (here called Polarimetric Phase Interferometry, POPI, [15], [16]). Figure 7-left shows the polarimetric ratio and POPI of sea water and sea ice as obtained from their Fresnel coefficients (from formulations in [147]). The figure clearly shows two separate regions, for sea water and for ice. Actual measurements are also affected by the textures of the roughness, the purity of the transmitted signals and the receiver instrumental response. These ideas were tested during an ESA field campaign conducted between November 2008 and May 2009 from a 700 m cliff overlooking Disko Bay, Greenland (ESA's GPS-SIDS campaign). Despite the polarimetric ports were not calibrated, signatures consistent with the sea ice concentration were found (Figure 7-right). The ideas on polarimetric response of water/ice surfaces were also tested in a shipborne experiment, conducted 2016 in Fram Strait, which provided reflectometry data during drift and fast ice periods [148] in two orthogonal polarizations for reflections at slant elevation angles (5° - 30°) (Figure 8). The power loss observed in LHCP data during the transition from calm open-water to the regime of high sea ice concentration agrees with model predictions. Recently, the receiver chain of SMAPs radar, working at two linear polarizations, has been used to search for GNSS reflected signals. For the first time it has been possible to obtain from a spaceborne platform the polarimetric signatures of GNSS reflected signals. Over polar regions, the polarimetric ratio, here defined in linear base and at smaller angle of incidence (40°) has shown sensitivity to sea ice [24].

The combination of different geometries (from nadir to 45° incidence and 5° to 30° elevation) accumulated in a few days within a relatively small area, together with the polarimetric capabilities of G-TERN may have potential to discern leads and polynyas and melt onset; or to help characterizing the snow cover above the sea ice and the phase of permafrosts active layer [23]. These potential products are some of the demonstration activities envisaged as secondary objective of the mission.

E. GNSS RADIO OCCULTATION

An additional, but secondary, objective for G-TERN is GNSS based radio occultation (RO) for precise sounding of the neutral atmosphere and the ionosphere. Global and precise atmosphere sounding using GNSS radio occultation has matured in recent years from experimental proof-of-concept missions to well-established and operational applications (e.g. [149]). Outstanding examples for this progress are the results from CHAMP (e.g. [149], [150]),

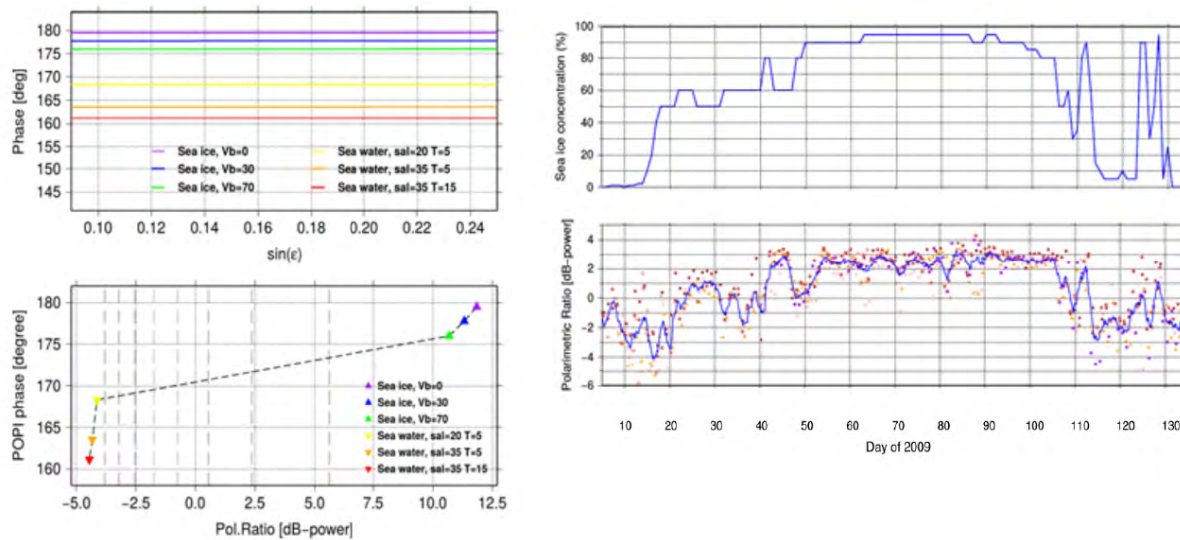


FIGURE 7. Left: Polarimetric phase interferometry (POPI) of sea ice and sea water obtained from their Fresnel reflection coefficients. Left-bottom: The same magnitude as a function of polarimetric ratio, at 15° elevation angle, using the same examples of sea water and sea ice. The vertical gray dashed lines mark the polarimetric ratio for absolute permittivities going from 10 to 70 (left to right) in steps of 10 units. Right: ESA experimental campaign of reflectometry at 700 m cliff over Disko Bay, Greenland 2009, GPS-SIDS contract number GPS-SIDS, R21793/08/NL/ST. Top-right: the sea ice concentration values (visually inspected from site). Top-bottom: GNSS-R polarimetric ratio measured at 10° deg elevation angle, with uncalibrated ports. Figures from [16] reproduced with authorization of the authors.

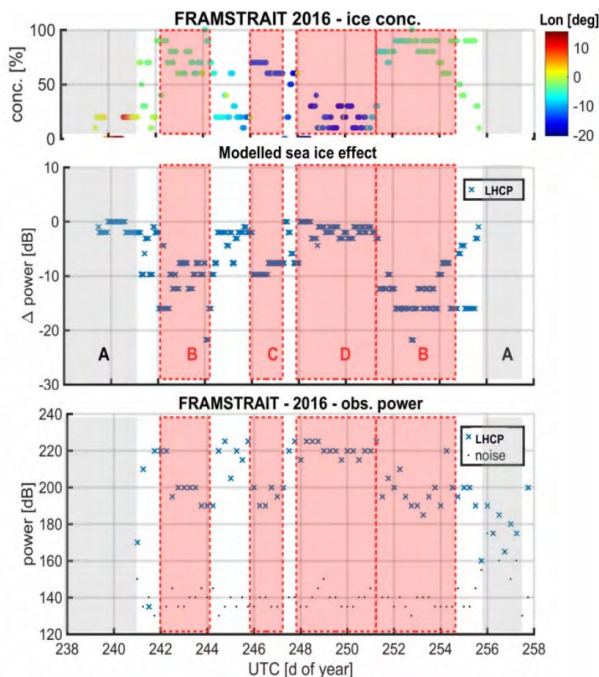


FIGURE 8. Sea ice characterization from a shipborne GNSS-R experiment. Sea ice concentration routinely observed from the ship (upper panel). Close drift ice period B occur in central Fram Strait. Fast ice C and open drift ice D was spotted near the Greenland, western Fram Strait. Rough sea periods A without sea ice were encountered near Spitsbergen, eastern Fram Strait. Modelled power loss due to increased ice concentration (centre panel). Power estimates from the shipborne reflectometry data (lower panel).

GRACE (e.g. [151]) and FORMOSAT-3/COSMIC satellites (e.g. [152], [153]), and their operational assimilation into the weather forecast systems since 2006 [84], [154]–[159]. The RO measurements brought significant improvements in

forecast quality [153], [160] and in atmospheric reanalyses [161], [162] because they complement the information provided by satellite radiances, as a result of superior vertical resolution, and the ability to assimilate them without bias correction. Furthermore, computations based on ensemble data assimilation techniques suggest there is a strong case for increasing the RO data numbers for NWP applications [163].

Continuous RO observations starting with CHAMP data in 2002 enabled the establishment of a meanwhile 15-year climate record with highest quality in the UTLS (Upper Troposphere and Lower Stratosphere) [86], which is of high benefit for monitoring climate variability and detecting changes in the Earth's atmospheric temperature and further relevant parameters [85], [164], [165]. RO measurements are also now considered a key observation type for climate reanalyses [161]. More generally, we expect the climate applications to increase in the coming years as the time-series lengthen. RO data are also valuable for investigating atmospheric dynamics, e.g., the planetary boundary layer [166], the tropopause region [167]–[169], wind fields [170], atmospheric tides and waves [171]–[173] and further phenomena [174].

In addition to RO-based remote sensing of the neutral atmosphere, also the ionospheric profiles of free electron number density are being consolidated as one unique source of information in terms of global coverage and accuracy. This has been motivated since the pioneering RO-mission, GPS/MET [175]–[180], to other follow-on missions like CHAMP, SAC-C and COSMIC/FORMOSAT-3 (e.g. [181], [182]), among others. Now, in parallel with the better understanding and improvement of the RO technique (see, e.g. [183]), the ionospheric electron density profiles

are widely used for space weather related but also climatological studies related to the variability of the Earth's ionosphere [153], [184]–[186]. Complementary results verified the potential, according to classical Chapman theory, to monitor climatologically parameters of the thermosphere such as the scale height by measuring the equivalent slab thickness. Recent computations based on measurements of the total electron content (TEC) and the peak electron density, have indicated a cooling of the thermosphere above northern Germany during the recent solar cycle [187]. It has been recently proven to be a much better description of the topside electron density profile in terms of a linearly varying scale height (Vary-Chap model), in agreement with the first principles prediction (based on an increasing electron temperature with height in such a region [188]). GNSS RO enables measurements all over the globe, in particular also at low latitudes where highly dynamic electron density variations and plasma turbulences occur but the data base is far from being sufficient and will profit from the G-TERN data. The impact of a better modelling of the ionospheric contribution to the bending angle is receiving as well an increasing interest [189].

GNSS RO data are currently already operationally available from several missions, e.g., Metop-A/B, GRACE, TerraSAR-X, TanDEM-X, and the dying FORMOSAT-3/COSMIC mission. Several new operational missions with GNSS RO started recently or will be realized in near future, e.g., COSMIC-2, EUMETSAT Polar System - Second generation (EPS-SG), FengYun-3 (FY3), Spire. Therefore, the need to get RO data from G-TERN seems less compelling and is regarded as mission goal with lower priority, as compared to GNSS based ice and ocean remote sensing. Nevertheless, the case for increasing the number of RO measurements is clear [163].

Moreover, there are several highly innovative aspects supporting GNSS-RO measurements within the G-TERN mission. These are:

- Exploring new capabilities: Galileo, GLONASS and BeiDou signals for RO. In addition to the new signal structured in the new GNSS constellations, G-TERN would also use the modernized GPS system. Therefore, G-TERN will provide a unique data set for scientific investigations to improve POD and RO data analysis and related product quality.
- Provision of high quality RO data in the lower troposphere due to high-gain antenna, which is not possible from current missions.
- Strong complementarity to the grazing angle GNSS reflectometry approach, the coherent reflectometry observations for altimetric measurements of ice and ocean surface topography, which are part of the primary mission goals [12], [122]. This also represents provision of important additional atmospheric (dry and wet tropospheric) and ionospheric delay information partially collocated with the coherent G-TERN GNSS-R measurements and of relevance for the analysis and

correction of the grazing reflectometry measurements for ice and ocean surface height measurements obtained aboard the G-TERN satellite.

- Omnidirectional downlooking RHCP for reflectometry allows the reception of side-looking RO events, which last significantly longer than the standard occultation data events and are not available from current and future operational RO missions. They cover larger horizontally atmospheric regions and contain more atmospheric information as the currently used RO data products. The value of these data to improve global weather forecasts would be investigated in cooperation with the leading NWP centers. Experiments for a GNSS RO based monitoring system using 12 beams in parallel could be conducted from G-TERN (see Figure 9 for example of 24 hours coverage). This would allow assessing the potential of new scientific applications in polar but also non-polar regions, e.g., 3D atmospheric reconstructions to investigate meso-scale atmospheric phenomena, as, e.g. atmospheric waves.

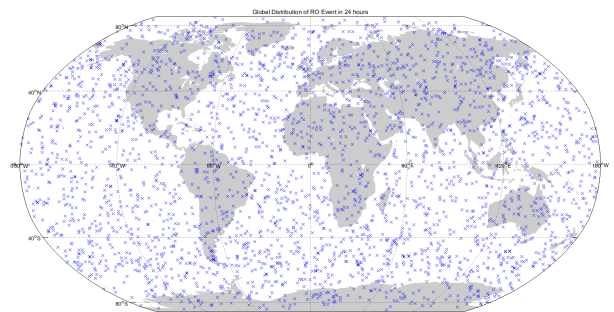


FIGURE 9. Example of geographical distribution of G-TERN RO profiles accumulated in 24 hours if all the twelve beams were devoted to capture GNSS occulting signals, enabling side-looking events. From this single receiving system it would be possible to acquire ~3000 RO profiles per day.

F. GNSS PRECISE ORBIT DETERMINATION

The success of G-TERN critically depends on the ability to accurately geolocate the phase centre position of the G-TERN antennas in a well-defined Earth-fixed terrestrial reference frame. For this purpose, Precise Orbit Determination (POD) using GNSS carrier phase tracking data, collected by a dedicated zenith-looking antenna, is a prerequisite and thus a key task of the G-TERN experiment. Most stringent POD accuracy requirements are needed for many satellite missions, typically demanding (1-D) position RMS errors of few centimeters, e.g., for gravity missions such as GRACE and GOCE (e.g. [190], [191]), altimetry missions such as Jason-2 (e.g. [192]), and SAR missions such as TanDEM-X and Sentinel-1 (e.g. [193]). Especially the radial component is crucial for altimetry missions to derive high quality data products. Most dynamic solutions based on a sophisticated force modeling of the underlying orbital dynamics are thus preferable for this type of orbit determination (e.g. [194]).

Off-line dynamic and reduced-dynamic POD based on dual-frequency GPS data has evolved to a mature and well established technique, offering cm-accuracies. As a prerequisite the attitude motion of the onboard GNSS receiver antennas in inertial space needs to be precisely known, e.g. from star tracker measurements, and GNSS sensor locations need to be well specified by proper calibrations on ground such that only small systematic errors remain in the data, e.g. antenna phase center variations, that may be calibrated in orbit [195]. Compared to dynamic and reduced-dynamic orbit determination only marginally worse accuracies are today achieved in the kinematic mode if the number of simultaneously and continuously tracked GPS satellites is sufficiently large.

V. IMPLEMENTATION

A. INSTRUMENT

The instrument concept is based in previous studies led by Airbus DS Space System España, (former EADS CASA Espacio), namely: the ESA PARIS In Orbit Demonstration (PARIS-IOD) Critical Technology-1; the ESA PARIS-IOD GNSS-R Feasibility Study; and the ESA GEROS-ISS industrial feasibility (mission's phase-A) study.

This section provides a brief overview of the main characteristics of the payload. The instrument will work in two RF frequency bands simultaneously L1 (1570.809 MHz) and L5 (1189.35 MHz) that are converted to intermediate frequency by means of a local oscillator. The bandwidths are set to 47.322 MHz and 63.9 MHz at L1 and L5 respectively. Many parameters will change from one operational observation to the next, mainly driven by the selected application (altimetry, scatterometry, grazing altimetry, radio occultation) and acquisition geometry. Even during the observation, adaptation of parameters is required, i.e. delay coefficients, beams, etc.

All these particulars prompt to plan a flexible commanding technique that is able to cope with a multitude of user demands and needs. In principle, the commanding concept provides the capability to program an operational run of the instrument in form of a series of user defined antenna modes and applications states during a swapping period. Each application state can be split into different sub-states reflecting beam pointing changes during the state. Each antenna mode, application state pair reflects the complete parameter setting for a dedicated instrument operation and selectable time duration.

These features are planned to be implemented in the G-TERN instrument through the following elements, sketched in a blocks diagram in Figure 10:

- Instrument RF Front-End including:
 - 1 Double side (Up and Down) antenna Array
 - 31 Calibration and Low Noise Amplifiers Modules (CAL/LNA)
 - 4 Beam Forming Network Units (BFN)
- Instrument Back-end including:
 - 4 Signal Processor Unit (SPU)
 - 1 Instrument Control Unit (ICU)
 - 1 Precision and Orbit Determination Receiver (POD)

– 1 Power Supply Unit (SPU)

For instrument time synchronization it is convenient to use the GPS/POD time as a highly accurate atomic time scale. This time scale is available in both the ground segment and the satellite, on ground by conversion of UTC time to GPS time and onboard due to the use of POD receiver. The onboard POD receiver outputs a PPS (pulse per second) time tick signal which will be used onboard as a 1 Hz synchronization signal. This synchronization signal coincides with the GPS epoch with a very high precision and fixes the exact moment of GPS time validity. Hence, any onboard event can be dated accurately in terms of GPS time by means of time measurements with respect to the PPS signal and by assigning the absolute GPS time to the relevant PPS epoch.

A set of instrument modes is introduced to ease the operation of the instrument from ground on one hand and to clearly structure the control of the instrument according to the system hierarchy on the other hand. The instrument is set into the desired mode by processing the commands from ground. The instrument control expands or converts the commands into an appropriate sequence of instrument internal commands that will be sent to other units and modules. The on-ground telecommand generation should follow a simple approach. First, the user must select the GNSS to be tracked. Depending on the desired application the instrument must point the antenna towards the direct signal and/or the reflected one. Second, the user establishes a sequence of observation states (applications) within a swapping period and some parameters that configure the selected application such as integration times. Based on the parameter information the instrument control composes and sends the required commands to the CAL/LNA, BFN and SPU units. Imaging of desired ground scenarios is planned and prepared in advance on ground. During this planning phase the desired orbit position and the related OBT time are predicted for each observation and are included in the corresponding time-tagged Configuration commands.

The instrument electrical concept is the result of a trade-off between instrument complexity and the survival of all mission applications. The Instrument Control Unit is the central element in charge of instrument operation. The front-end and back-end elements respond to ICU commands. The operational synchronization of all elements is under this unit responsibility. The SPU is based on the signal processing cores developed for PARIS-IOD and GEROS-ISS missions, the 'PARIS CORrelator' (PACO) unit [204]. The SPU control is basically the PACOs control. Each PACO has one Spacewire interface that shall be used by the ICU to control all PACO internal parameters and configurations. The same Spacewire interface is used for housekeeping and scientific telemetry.

The two G-TERN antennas are arrays of 31 patch elements (up-looking side) and 30 path elements (down-looking side) in a hexagonal array lattice with a separation of 178 mm between patches as shown in Figure 12. The down-looking side of the antenna contains Left Hand

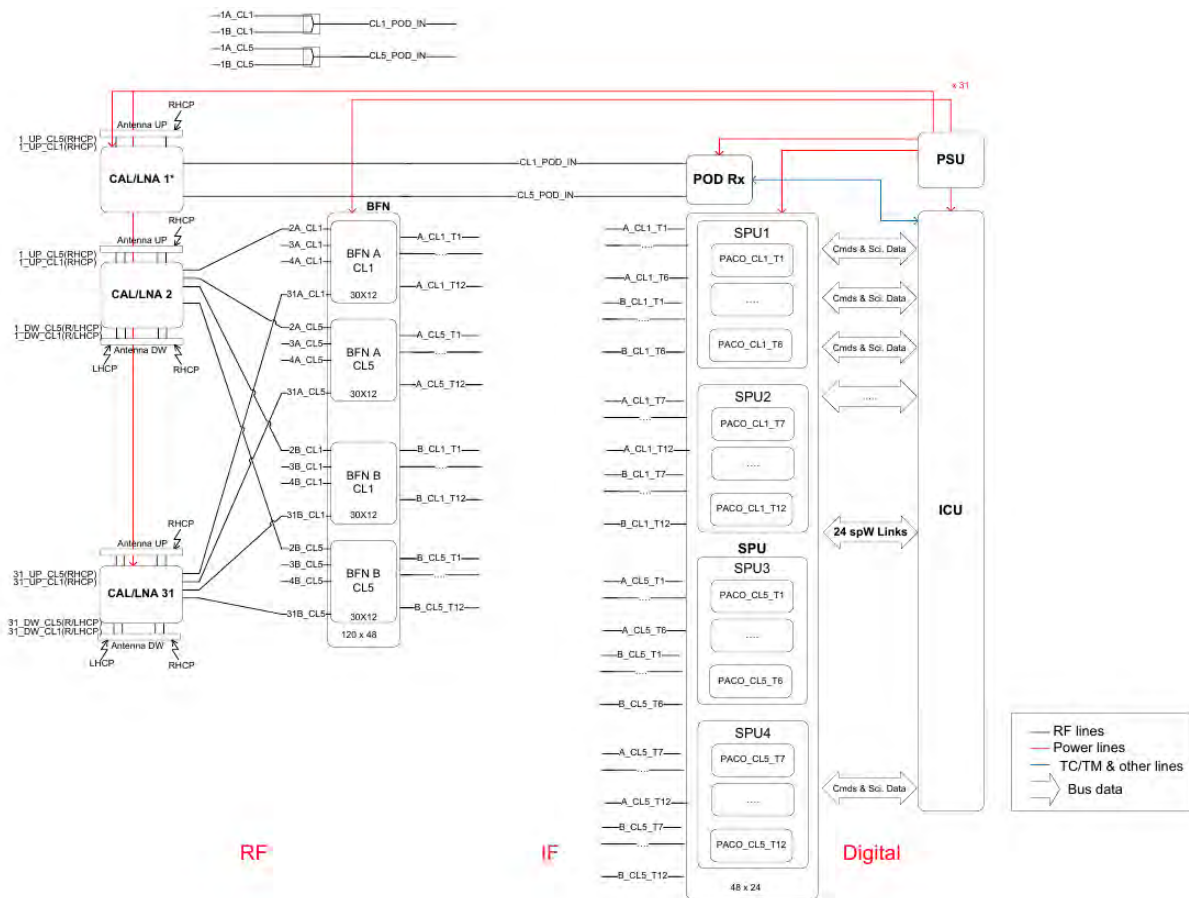


FIGURE 10. G-TERN instrument block diagram.

Circular Polarized (LHCP) and Right Hand Circular Polarized (RHCP) polarizations and the up-looking antenna RHCP only. The central element in the up-looking array is used for the POD receiver and the central element of the down-looking is used by a retro-reflector allowing laser ranging, so actually the array has 30 active elements. The concept for the G-TERN elementary radiator is similar to the PARIS-IOD elementary radiator, developed in the frame of ESA contracts PARIS-IOD Critical Breadboarding -1 (No.102784) and GNSS-R-Feasibility Study (Phase A) (AO/1-6576/2010/F/WE). The radiating elements of the antenna array are stacked circular patches using as substrate an air-like foam. In this configuration, an active circular patch is excited by two coaxial probes that are combined with a 90° hybrid coupler with one stage to provide the required bandwidth. Each input of the hybrid provides an orthogonal circular polarization (RHCP and LHCP). Therefore, it is possible to have access to both circular polarizations at each radiator by terminating the 90° hybrid by a connector. An array model has been developed in order to simulate the antenna performance for the different coverages. This model takes into account the coupling between elements in the array using the Finite Array Generalized Scattering Matrix

Method with spherical modes coupling. Thus, the radiation pattern of each element in the array is different due to the couplings between the adjacent elements. As an example of this effect (and the importance of considering the coupling and not just an array factor computation), Figure 11 shows the embedded radiation pattern of the central element at L1 band (1575 MHz) in directivity.

Variable antenna beam pointing can be achieved by respective control of received signal phases of each RF path within the beam-former Network. To cope with this task a number of basic one-dimensional phase settings for elevation and azimuth pointing, respectively, will be stored in separate onboard look-up tables. A particular antenna beam configuration will then be generated by means of simple onboard synthesis that combines two one-dimensional settings in elevation and azimuth to the desired phase setting of the operational beam. This procedure supposes an ideal behavior of phase shifters. Compensation of unwanted parasitic effects, which would degrade the beam steering, is another task of the instrument control by means of compensating the effect via the control of one attenuator per RF path. The pointing angles used to select azimuth and elevation indexes shall be calculated on board using the relative positions between

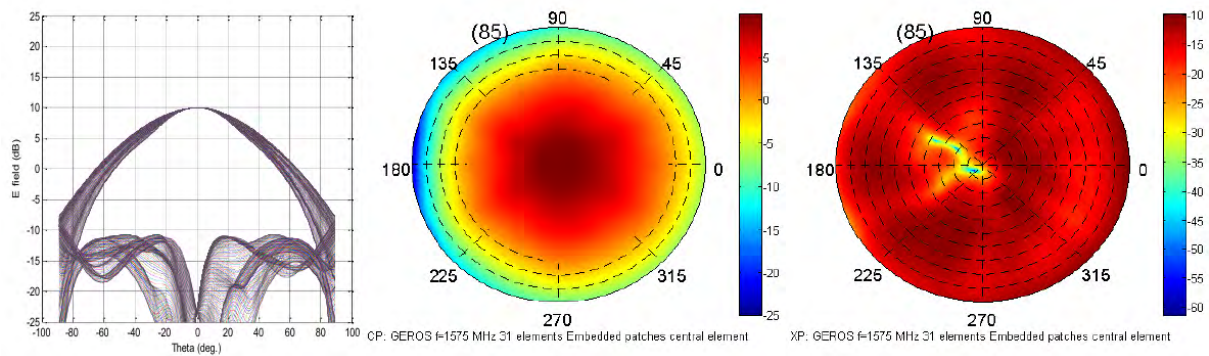


FIGURE 11. Embedded elementary radiator radiation pattern (central element; $f = 1575$ MHz).

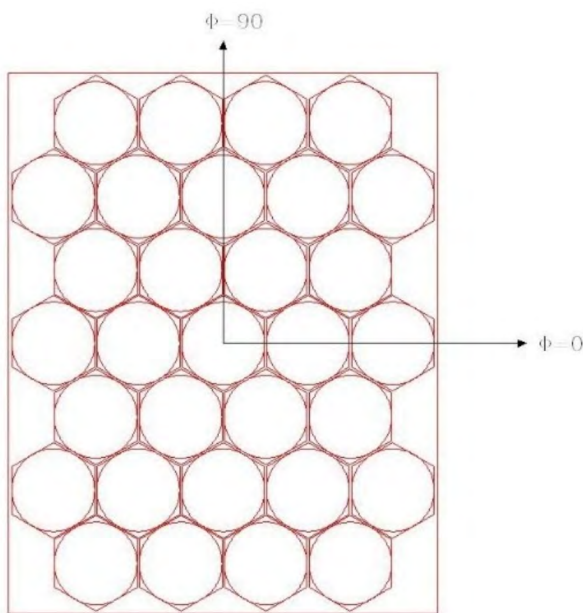


FIGURE 12. G-TERN antenna array.

G-TERN, GNSS transmitter and reflection point plus the application type. The relative angles are derived from present G-TERN position and GNSS predicted position. G-TERN position is propagated from Precise Orbit Determination data and GNSS position is propagated from TLE parameters. The beamforming network is based on 4 BFN modules, each pair devoted to one RF path at one frequency. Each BFN module delivers 12 different beam outputs, to enable the synthesis of 12 different beams simultaneously. The architecture is based on a succession of four stages: RF dividers, beam former, using variable attenuators and phase shifters, RF combiners and RF to IF down-converters. The BFN section is a 48 beams conforming network (from a 30 elements array) together with down-converting from RF to IF. Furthermore it includes DC/DC converter from primary supply bus and LO signal generation from Master Clock. The 48 beams correspond to 12 beams for each frequency (CL1 and CL5) and for each antenna (up- and down-looking).

The beams at intermediate frequency are connected to the processing unit SPU. This module is based on ADC

chips and ASIC correlators controlled by Spacewire links, which are able to perform different processing techniques for GNSS reflectometry, scatterometry and radio occultation. Each correlator can compensate the physical delay and the Doppler frequency differences between the signals to process (i.e. for altimetry application the up and down signals). The coherent and non-coherent integration times are also configurable via the Spacewire interface. Also each correlator allows the use of clean replica codes to be processed together with the down-looking signal for radio occultation purposes.

The main components of the board are sketched in Figure 13. The SPU boards are clocked by the G-TERN master clock of 153.6MHz (TBC). The clock distribution ensures that the skew between all ADC and the PACO are so that correct sampling of the data is guaranteed. The foreseen ADC features a 1:2 de-multiplexed data signal, meaning that the data rate is half of the sampling clock of 153.6 MHz, hence 76.8 MS/s. The analogue part of the board is placed on the left side of the board, whereas the digital interfaces are connected to the backplane. In addition to the digital interfaces, the power supply is also routed via the backplane. Local Point of Load (PoL) converters are foreseen, to ensure stable supply for all components of the SPU board. The PACOs are placed as close as possible to the backplane, in order to maximize the heat transfer to the frame.

The concept for the PACO processor includes the cross-correlation of up-looking and down-looking beams' signals, its swapping, Doppler and delay compensations, and voltage offset compensations, among other features. The swapping can be configured via the interface control unit (ICU). The cross correlator is a 400 tap lag correlator, running at 76.8MHz, hence a tap spacing of 13ns. The output of the cross correlator is then fed into a Doppler Shift circuit (called Doppler bin), which is replicated for 5 different Doppler frequencies (controllable via the ICU). The circuit allows to further increase the number of Doppler frequencies up to a factor of 3 (with reduced time resolution). PACO generates the DDM as power and/or complex waveforms.

The Instrument Control Unit (ICU) shall be in charge of the control of the overall instrument, data handling, data storage and of interfacing towards the platform. It is the operational centre of the whole instrument. So it is in charge

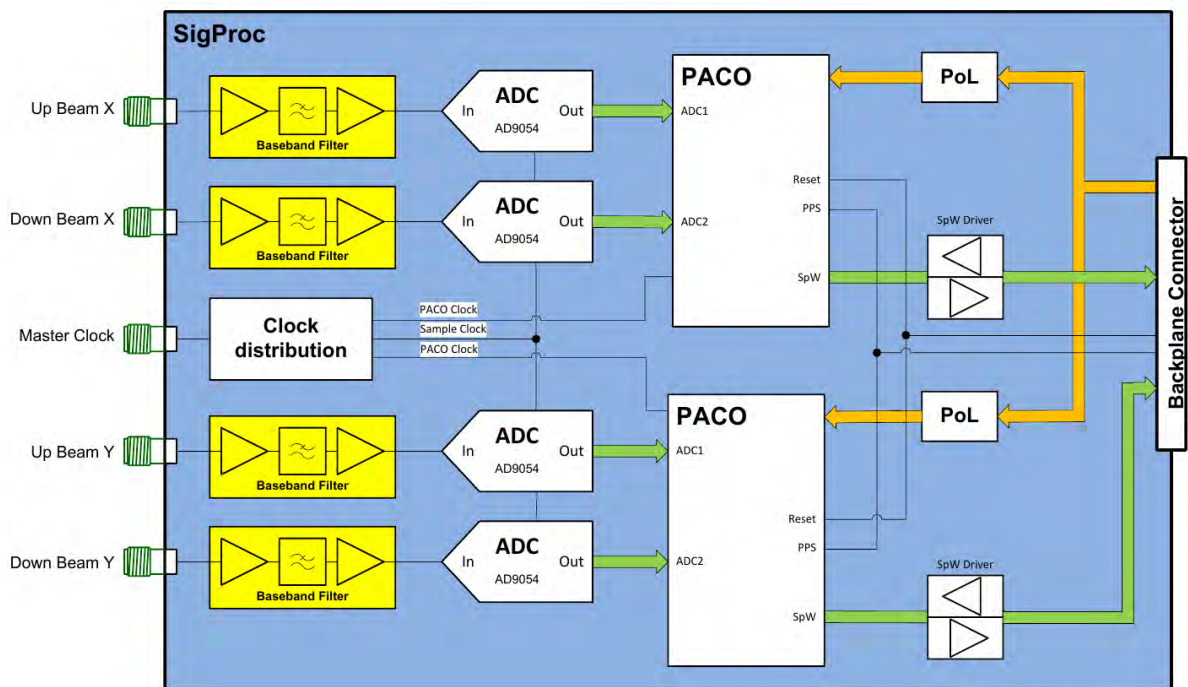


FIGURE 13. Signal-Processor Unit board concept.

of the instrument preparation for an event observation and the synchronized execution of the observation. It manages the beams pointing, the CAL/LNAs switching and the operational management of the SPU, providing it with data as Doppler settings, coherent and incoherent integration parameters, desired output waveform, etc. It also generates and distributes the master clock to the whole instrument. It is basically composed of a microprocessor system, where the software runs, a big memory module, an instrument house-keeping signals acquisitions module and hardware interfaces towards the rest of the instrument modules and the satellite platform.

The ICU is based on a unit composed of two completely redundant parts assembled in a common mechanical housing hosting three different types of board per section plus two boards common to both sections: Interface Module (IM), in charge of the instruments data processing and communication with the platform and instruments down-stream units (BFNs, SPU, POD, and CAL/LNAs); Specific Interface Module (SIM), in charge of generation and acquisition of discrete standard interfaces (as thermistors, voltages, currents) needed for monitoring, reporting and control of the complete instrument; Converter Module (CM), in charge of providing Power Conversion functions; Clock Distribution Module (CDM), amplifying, splitting and combination of master clock signal to be distributed towards the G-TERN Instrument units; Backplane (MB), connecting all modules and performing the signals cross-strapping where needed.

A POD receiver subsystem is included in the instrument which: (1) provides the on-board time reference to all the instrument, including the PPS signal; (2) provides the

position of the instrument to the ICU; (3) obtains ephemerides data to estimate the reflection observation; and (4) delivers observables that are considered as Level 0 data products and it is used in the geo-location of the power-delay waveforms in the level 1B product.

Finally, Table 4 shows the main performances and budgets of instrument units and for the overall instrument. The total estimated power consumption is 461.6 W (553.92 W with 20% margin), and the total weight 266.63 kg (319.96 kg with 20% margin).

B. PLATFORM

In order to accommodate the payload and support its operations in orbit, the OHB LEO platform has been preliminary selected for the G-TERN mission. The platform fits within the constraints coming from the above described payload characteristics and is compliant with the G-TERN mission requirements. Designed mainly for LEO Earth observation missions, it is based on EnMAP heritage, combined with experiences from Galileo and SAR-Lupe and SARah. The G-TERN platform is tailored to fly in Sun-Synchronous Orbits (SSO) between 600 and 800 km altitude and different Local Time of the Ascending Nodes (LTANs) can be attained with minimum modification of the spacecraft accommodation. Different orbits require adaptation of the platform with the magnitude of fall-outs depending on the deviation from the nominal: however the platform is again flexible to cope with these changes with, possibly, few adaptations. The platform offers a design lifetime of 10 years and it is intended for the payload ranges detailed in Table 5. A major highlight is the capability to be launched with a dual-launch

TABLE 4. Main budgets and performances of the G-TERN instrument.

Antenna Array Structure	1 Unit
Mass per unit (kg)	18.5
Dimension per unit (L,W,H mm)	900x1135x334
Radiator	31 Units (Up) + 30 Units (Down)
Outputs	Up: U_RHCP; Down: D_LHCP and D_RHCP
Mass per unit (kg)	0.24
Dimension per unit (L,W,H mm)	178x90x22
CAL/LNA	31 Units
Inputs	U_RHCP, D_LHCP, D_RHCP
Outputs	A-CL1: U_RHCP or D_LHCP or D_RHCP; A-CL5: U_RHCP or D_LHCP or D_RHCP; B-CL1: U_RHCP or D_LHCP or D_RHCP; B-CL5: U_RHCP or D_LHCP or D_RHCP
Mass per unit (kg)	1.9
Dimension per unit (L,W,H mm)	135x94x167
Power per unit (W)	2.65
BFN	4 Units
Inputs	BFN_A-CL1: 30xA_CL1; BFN_A-CL5: 30xA_CL5; BFN_B-CL1: 30xB_CL1; BFN_B-CL5: 30xB_CL5 Total: 120
Outputs	BFN_A-CL1: 12 A-beams at CL1; BFN_A-CL5: 12 A-beams at CL5; BFN_B-CL1: 12 B-beams at CL1; BFN_B-CL5: 12 B-beams at CL5 Total: 48 beams
Mass per unit (kg)	33.7
Dimension per unit (L,W,H mm)	380x480x270
Power per unit (W)	19.8
SPU	4 Units
Inputs	SP1: 6xA_beams_CL1 and 6xB_beams_CL1 SP2: 6xA_beams_CL1 and 6xB_beams_CL1 SP3: 6xA_beams_CL5 and 6xB_beams_CL5 SP4: 6xA_beams_CL5 and 6xB_beams_CL5 Total: 48
Outputs	12 correlations A*B at CL1 12 correlations A*B at CL5 Total: 24
Mass per unit (Kg)	12
Dimension per unit (L,W,H mm)	200x300x250
Power per unit (W)	81
POD	1 Unit
Inputs	CL1 and CL2
Outputs	ICU interface
Mass per unit (Kg)	7.2
Dimension per unit (L,W,H mm)	205x226x184
Power per unit (W)	24
ICU	1 Unit
Nr units	1
Inputs	24 correlations A*B
Outputs	3072 Kbps of instrument data rate
Mass per unit (kg)	10
Dimension per unit (L,W,H mm)	200x300x230
Power per unit (W)	20
PSU	1 Unit
Inputs	22V-37V unregulated
Outputs	31x CAL/LNA: DC/DC (N&R) V1 DC/DC (N&R) V2 DC/DC (N&R) V3 4XSPU (N&R): 22-37V 4X BFN (N&R): 22-37V 1xICU (N&R): 22-37V
Mass per unit (Kg)	10
Dimension per unit (L,W,H mm)	350x230x230
Power per unit (W)	25

TABLE 5. Main characteristics of the G-TERN platform.

Payload (kg)	mass	Average payload power (W)	Spacecraft mass (kg)	dry	Mission lifetime (years)	Payload downlink (Mbit/s)	data rate	Min platform dimensions (m ³)	Max payload dimensions (m ³)	Most constraining launcher
< 350		< 600	< 800		< 10	≤ 150		1.5 × 1.1 × 1.1 (L x W X H)	2.0 × 1.2 × 2.0 (L x W X H)	Inside Vespa, Upper Vega (on Vespa)

on Vega by using the VESPA adapter: depending on the payload volume, the spacecraft might even fit into the lower position inside VESPA. The platform is conceived to have a

‘plug and play’ payload, or in other words, to be decoupled from the payload module: the payload module is separated from the platform module and the two are only connected

via power, data and mechanical interfaces. The platform uses for the most parts off-the-shelf space-qualified components with Technological Readiness Level (TRL) ≥ 8 , while the subsystems, which require minor modifications for the specific mission needs, still reach a TRL $\geq 5/6$. The agile 3-axis stabilized platform is able to meet the most stringent pointing requirements. Furthermore, it offers several optional features to adapt to different mission-specific and payload-specific constraints, for example in terms of power generation and storage, payload data handling and transmission. The platform can comply with both uncontrolled and controlled re-entries. Due to its cost-effectiveness and modular decoupled design, providing separation between payload and platform modules and resulting in programmatic savings, the platform is the perfect candidate for the G-TERN mission in the frame of Earth Explorer 9 programme.

The platform is designed to fit either in the lower or upper position - depending on the payload - of the 'extended' VESPA (+500mm) of VEGA, for dual launch. In Figure 14, the spacecraft is depicted, fitting within the useable envelope of Vega upper position. The Launch Vehicle Adapter is a band clamp with a diameter of 937mm. Given the limited information available on Vega-C and the smaller size of current Vega fairing, the conservative approach of fitting the spacecraft inside the current launcher configuration was assumed. In the next phase of the study, following the consolidation of mission, payload and system requirements as well as updated information of the VESPA adaption to Vega-C, a more detailed assessment could be performed on whether and under which conditions/configurations it would be possible to fit the spacecraft inside VESPA, in lower position.

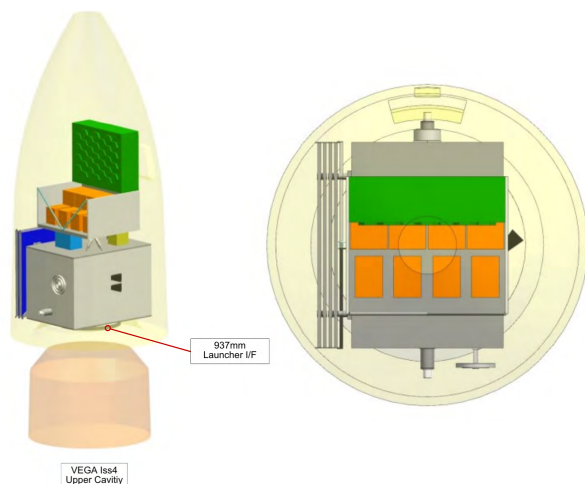


FIGURE 14. G-TERN satellite inside VEGA Launcher.

Figure 15 provides an overview of the G-TERN spacecraft in stowed and deployed configurations, with dimensions. It is possible to clearly identify the separation between platform module and payload modules and their isostatic mechanical interface. Figure 16 shows the internal units accommodation

of G-TERN. In Figure 17, the difference between two orbital configurations is shown: on the left, the platform is adapted to LTAN close to Noon-Midnight orbits (typical orbits for optical payloads) while on the right the solution is adapted to a Dawn-Dusk orbit. As it is possible to see, the orbit choice is flexible and minimum adaptation of configuration and internal accommodation is required (the radiator for both configurations on the hidden side in these figures).

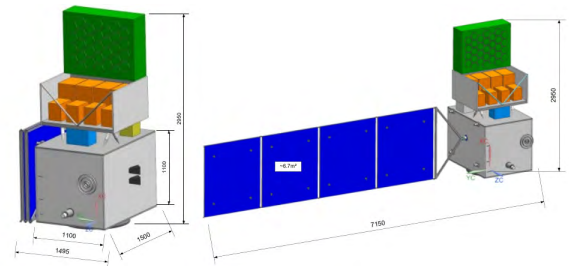


FIGURE 15. G-TERN satellite in stowed (left) and deployed configurations (middle).

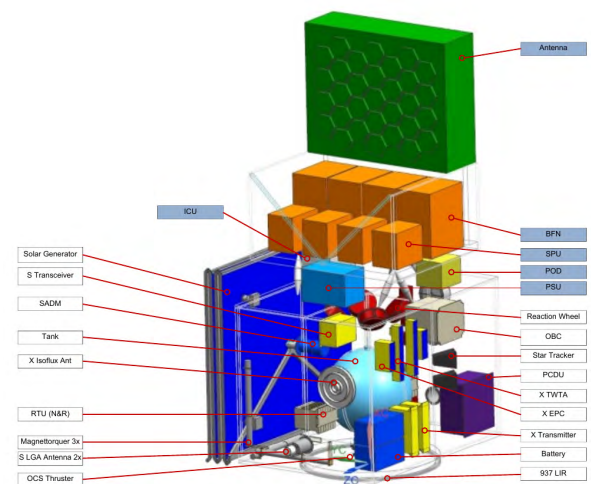


FIGURE 16. Internal accommodation of G-TERN payload systems and components.

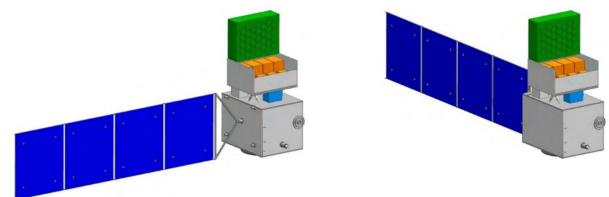


FIGURE 17. G-TERN solar array configuration for different orbits.

The propulsion system is sized to allow station keeping for 10 years in conditions of maximum solar activity. The residual propellant is used to perform perigee lowering for uncontrolled re-entry in less than 25 years. It is remarked that if the orbit altitude is selected close to 600 km, the spacecraft would naturally decay in less than 25 years. If a controlled

re-entry is required, adaptation of the propulsion system is needed: in the following phase of the development, a consolidation of mission requirements and spacecraft design will allow for detailed re-entry analyses and assessment of casualty risk, to demonstrate compliance with current regulations.

The telemetry and telecommand transmission is performed via S-band while the science data are downlinked via X-band, together with telemetry data for contingency. The payload data handling and transmission subsystem has the following characteristics:

- An Isoflux antenna allows transmission to the ground station
- The high data downlink rate and memory size allow considerable memory margins, even when considering 100% duty cycle with 12 beams and 2 frequencies, i.e. 3.1 Mbit per second of science data.

A downsizing of the payload data handling and transmission subsystem could be performed, if considered necessary, to reduce the design margins in a more mature phase. The data downlink budget was analysed assuming the Kiruna 13 meters dish with 5° minimum elevation angle. As the electrical power generation and distribution system (EPS) is concerned, a solar array driving mechanism coupled with a mounting cant angle, when applicable, allows to achieve high performances by sun tracking. The spacecraft has a 28V unregulated bus with direct energy transfer distribution. The electrical power system is sized for 10 years for a 600 km dawn-dusk orbit (LTAN 06:00), where maximum eclipse reaches 20 minutes duration in winter. The seven square meter solar array is able to provide 1315 W at the power control and distribution unit. Batteries provide 57 Ah at 33.6 V. The power budget is analysed under different modes of operation: 91% of the duty cycle it would operate under nominal operation mode, while the ground station pass mode (payload operational and simultaneous downlink) would happen up to 9% of the duty cycle. This results in an average power budget of 943.8 W, which consistently accounts for the design margins.

The mass budget has been estimated considering a range of margins (from 5% to 30% depending on the subsystem) and including the propellant mass. The total spacecraft wet mass then results in 870 kg, which fits within the constraints of the launcher and the EE9 Call.

VI. EXPECTED PERFORMANCE

The fulfillment of the required critical performances (Table 1) is evaluated by means of end-to-end simulation exercises. The exercises are limited to the altimetric performances, as they represent the most demanding application in G-TERN. The approach comprises the following blocks:

- 1) Generation of synthetic 1-second level-1 data according to the G-TERN orbital and instrumental characterization, as well as a limited set of sea ice conditions and geometries. These data sets must include the different noise components, in the form of a Monte Carlo like approach.

- 2) To apply the inversion algorithms to retrieve the group-delay altimetric products (1 Hz level-2 data) from the synthetic level-1 observables generated in block 1 above.
- 3) To determine the uncertainty of the retrieved 1Hz level-2 group-delay altimetric products over sea ice, by means of comparison with the well-known ground truth (simulation settings) and the dispersion obtained from the Monte Carlo set of samples. Blocks 1 to 3 are presented in Section VI-A. Given that GEROS-ISS mission went through industrial and scientific feasibility studies (Phase-A) and these sort of exercises were done and compiled for Ocean applications in [123], we limit these simulations to sea ice scattering conditions, and will use the outcome of [123] for sea surface altimetric performances.
- 4) To simulate phase-delay synthetic data and its retrieved altitudes to estimate the 1-second equivalent phase-delay accuracy (Section VI-B).
- 5) To simulate the location of the specular points that a G-TERN system would collect in 3 days, at 1 second sampling over polar areas (here defined as $|lat| > 60^\circ$). Define a grid of cells sized 30 km \times 30 km across the polar zone, and group the 1-second observations by the cell where their specular points belong.
- 6) With the 1-second uncertainties obtained in blocks 3 and 4 above and the number of 1-second observations within each cell obtained in block 5, compute the overall uncertainty over each cell.
- 7) Analyze the statistics of the obtained uncertainties at each cell within the 3 days simulation period. Blocks 5 to 7 are presented in Section VI-C.

A. GENERATION OF 1HZ-LIKE LEVEL-1 WAVEFORMS AND DERIVED LEVEL-2 GROUP-DELAY ALTIMETRIC ACCURACIES

This section compiles blocks 1 to 3 of the end-to-end simulation description above. The simulations correspond to the G-TERN orbit and instrument (see Sections III and V respectively) in four different geometries and two rather extreme examples of sea ice, the best and worst reflectors. The best case reflector corresponds to smooth ice (low roughness) and more reflecting, i.e. saltier ice such as first-year (FY). For simplicity we will call it FY (despite FY can also be rougher). The worst reflector corresponds to ice with rough surfaces and less reflecting properties, i.e. fresher ice with less salt, such as in multi-year ice (MY), hereafter identified as MY (despite MY ice can present smooth surfaces). The smooth sea ice corresponds to the conditions found in Hudson Bay in TDS-1 TD18, 15th January 2015 [29], [30], providing highly specular reflections. The scattering regime for the MY extreme case considered here has been analyzed through TDS-1 TD51 track, 11 February 2015, from 16:55 to 16:58 UTC, for rough ice conditions. The summary of relevant parameters is given in Table 6, including orbital, instrumental, geometries and characterization of the sea

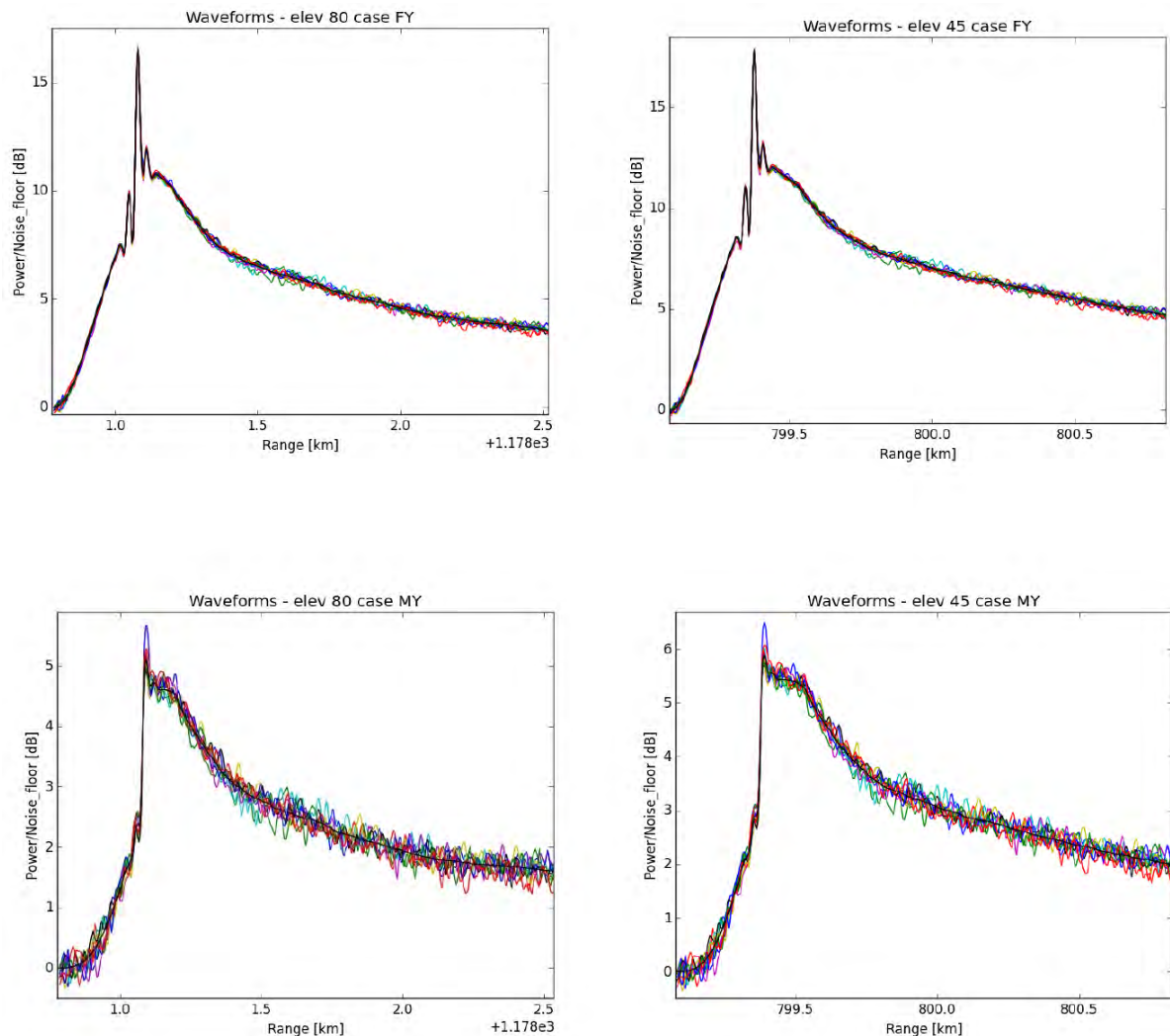


FIGURE 18. Examples of 10 synthetic level-1 waveforms generated for four scenarios (colored lines), in dB SNR. In black the noise-free or 'average' waveform. Top-left: best case (smooth first year sea ice with 4 times larger coherent scattering than diffuse scattering) observed at 10° incidence (80° elevation). Top-right: same for 45° incidence angle. Bottom-left: worst case (rough multi-year ice with diffuse only scattering) observed at 10° incidence (80° elevation). Bottom-right: same at 45° incidence. Note that the simulations included 1,000 of such noisy synthetic level-1 products, only 10 randomly selected are shown here for clarity purposes.

ice (surface roughness and permittivity) and the scattering regime (ratio between coherent and incoherent scattering, analyzed on actual TDS-1 data following the methodology in [104]).

For each geometry and ice type, 1000 realizations of 1 second incoherent integration each have been generated with the 'wavy' open source simulation tool [196], [197]. The coherent integration time is set to 1 ms. Within the wavy simulator, the noise terms include thermal noise and speckle, with their corresponding distinctive delay-correlation and time correlation. The delay-correlation of the noise is relevant to the altimetric precision because the retrieval algorithm takes the derivative of the leading edge and this involves differentiating the waveform along its delay axis. Noise correlated along the delay axis tends to reduce the noise of this altimetric retrieval. As for the time-correlation of the noise, it has

a relevant role in the final determination of the dispersion of the 1-second waveforms. For example, if the model determines that the correlation time of the measurement is longer than 1 ms, then the 1000 ms integrated within one second are not fully independent and the dispersion is not reduced as $1/\sqrt{1000}$ but for the corresponding number of independent samples in one second (e.g. [96], [105]).

Figure 18 shows 10 noisy waveforms (level-1 product) out of the 1000 realizations corresponding to four of the simulated scenarios: best reflector and worst reflector for 10° and 45° incidences, the highest and lowest incidence angles simulated in the exercise. The signals reflected off rough multi-year ice, under purely diffuse regime and lower permittivity (extreme case with volumetric brine content set to zero and L-band $mss=0.017$), present much larger noise levels than the mostly coherent scattering off the

TABLE 6. Settings of the simulation to generate the level-1 observables for 1 Hz group-delay altimetry over sea ice.

Near-nadir group-delay simulation of level-1 synthetic data for sea ice G-TERN reflectometry		
Orbit height:	600 km	
Antenna gain:	20 dB	
Sampling rate:	76 Msamples/second	
Receiver bandwidth:	10 MHz at baseband (G-TERN has configurable filters, this number should be optimized in further phases of the mission)	
Noise figure:	3.5 dB	
Incidence angles:	10°, 20°, 30°, 45°	
Sea ice characterization (extremes):	Best case: coherent on FY	Worst case: diffuse on MY
	Roughness [11]: $\sigma_z=0.1$ m $L_{coh}=3.3$ m $mss=2 \sigma_z^2/L_{coh}^2=0.002$	Roughness [11]: $\sigma_z=0.3$ m $L_{coh}=3.3$ m $mss=2 \sigma_z^2/L_{coh}^2=0.017$
	Permittivity [148]: $V_b=70$ $\epsilon=3.750 + j 0.390$	Permittivity [148]: $V_b=0$ $\epsilon=3.120 + j0.040$
	Scattering regime: Coherence analysis in [105] applied to TDS-1 data [30] results in $P_{coh}/P_{diff} = 4$	Scattering regime: Coherence analysis in [105] applied to TDS-1 rough MY data results in diffuse scattering

TABLE 7. Mean error and dispersion of the error resulting from the simulations described in this section, corresponding to 1 Hz level-2 sea ice altimetric products. Reflection off smooth salty sea ice (best reflector) and rough fresh ice (worst reflector) have been simulated at four geometries each, and 1000 times for each case following a Montecarlo-like approach.

Group-delay sea ice altimetric error from 1000 level-1 sea ice reflected waveforms, thermal and speckle noise terms:			
Case:	Mean error (bias-like):	Standard deviation σ :	Multi-Doppler processing, standard deviation σ :
Best reflector 10° incidence:	< 0.1 cm	2.5 cm	1.9 cm
Best reflector 20° incidence:	< 0.1 cm	2.6 cm	2.0 cm
Best reflector 30° incidence:	< 0.1 cm	2.7 cm	2.0 cm
Best reflector 45° incidence:	0.1 cm	3.4 cm	2.6 cm
Worst reflector 10° incidence:	-1.7 cm	39.7 cm	29.8 cm
Worst reflector 10° incidence:	-1.9 cm	39.1 cm	29.3 cm
Worst reflector 10° incidence:	-1.9 cm	42.6 cm	32.0 cm
Worst reflector 10° incidence:	-3.1 cm	58.9 cm	44.2 cm

smooth Hudson Bay first-year ice. Note that the scattering off smooth first-year ice has been set to a regime with 4 times higher coherent power than diffuse power, as deduced from TDS-1 data in [30] applying the method described in [104]. An altimetric retrieval algorithm based on the leading-edge derivative (LED) approach [94], [114], has then been applied to each of these level-1 noisy waveforms. The inversion algorithm provides an altimetric solution (level-2 product) for each of the level-1 waveforms. Given that the exact ‘true’ altimetric information is known (set by the simulation), we can then extract the error obtained in each case. The statistics of these errors provide indication of the overall expected bias and root mean square (RMS) dispersion (1- σ precision). Table 7 summarizes the results, which show precisions of the order of 3 cm in 1 second observation over the best reflector (smooth FY ice). On the other hand, group-delay altimetry measured with G-TERN over extreme rough and low permittivity sea ice presents worse precisions by one order of magnitude, especially at the edge of the near-nadir field of view (45° incidence). Closer to the nadir (10° incidence) the precision is 39.7 cm. Recent studies have proved both theoretically and with actual spaceborne GNSS-R TDS-1 data, that the precision can be improved by a factor of 20-30% using multi-Doppler altimetric algorithms [101], [198]. An intermediate reduction factor of 25% in the dispersion has been here assumed in the last column of Table 7.

The accuracies obtained in this exercise must be complemented with the uncertainties given by other systematic

effects, such as orbital errors, tropospheric errors and ionospheric errors. The orbital errors (precise orbit determination, POD) and tropospheric errors are obtained with the simulator developed for the GEROS-ISS mission, and for simplicity they will be here fixed to 5 cm POD and 1 cm for tropospheric residual errors [123]. Note that these values were computed for GEROS-ISS, and for this reason they represent a conservative envelope of the actual expected values: the POD error values at the ISS are larger than POD values in small satellites (larger uncertainty in ISS positioning is due to large structures with changing mass distribution, uncertain centre of mass, changes in attitude due to maneuvers, etc). As for the troposphere, the 1 cm standard deviation of the residual errors found in GEROS-ISS studies were based on actual ECMWF field values and their uncertainties across tropical areas, where the atmosphere is moister than in polar areas.

The ionospheric effects have been simulated through the SCIONAV model, developed under an ESA contract [199]. This tool was initially developed to investigate the influence of ionospheric perturbations on the performance of navigation receivers. This simulator has been later used to study the impact of ionospheric perturbations in GNSS-R scatterometry [200] and altimetry measurements [201] with the GEROS-ISS mission as example. The solar activity predicted for period when G-TERN would orbit, the 25th solar cycle (2017 to 2029), is expected to be mild (110 sunspots of of maximum [202]). Nevertheless, the simulation has used two extreme values of

TABLE 8. Total group-delay altimetry uncertainties in the near-nadir field of view (incidence $\leq 45^\circ$), including thermal and speckle noise, orbital, tropospheric and ionospheric errors. The noise figures for level-2 sea ice altimetric products have been obtained from a polynomial fit as a function of the incidence angle (θ) of the data in Table 7 for two extreme sea ice conditions (best and worst ice reflectors), and multi-Doppler processing is assumed. For sea surface altimetry, the noise terms have been extracted from the GEROS-ISS studies [123]. POD effects are all set to 5 cm level. Tropospheric effects all set to 1 cm level. Ionospheric effect at polar areas are negligible while 15 cm residual dispersion is assumed in the ionospheric-free GNSS combination at non-polar regions. All units in cm.

Final 1-second equivalent level-2 group-delay uncertainty (noise and systematic effects)	
	Total precision (cm)
Best reflector sea ice	$a+b*\theta+c*\theta^2+d*\theta^3$, $a=5.4$, $b=0.017$, $c=-0.0008$, $d=1.3e-05$ (mean ~ 5.5 cm)
Worst reflector sea ice	$a+b*\theta+c*\theta^2+d*\theta^3$, $a=32.5$, $b=-0.2861$, $c=0.0035$, $d=1.94e-04$ (30 to 45 cm)
Rough waters, polar zones	30.4
Rough water, non-polar zones	34 (30.4 to 44.9 cm)

solar activity for illustration purposes. Solar flux data from <http://www.sws.bom.gov.au/Solar/1/6> has been used, assuming a minimum solar flux $SF = 68.2$ SFU (corresponding to January 2009) and a maximum $SF = 223$ SFU (April 2000). Based on these numbers, the Global Ionospheric Scintillation Model (GISM) has been used to compute the corresponding scintillation indexes $S4$ and σ_ϕ at L1, L2 and L5 GNSS frequency bands. Over polar regions, ‘diffractive scintillation’ has not been found. This type of scintillation cannot be corrected using the ionospheric-free combination of GNSS signals. Therefore, only ‘refractive scintillation’ would be produced, which can be fully corrected with the ionospheric-free combination. Nevertheless, to be on the conservative side, we have generated the residual delay errors after ionospheric-free combination for the worst possible case, that is 0° longitude and 20° latitude at 20:00 UTC, which corresponds to the maximum perturbation. We will therefore consider that the G-TERN polar observations are not affected by the scintillation, but the non-polar ones would be affected, especially around the Tropics. The selection of a Sun-synchronous orbit 6AM-6PM would minimize this effect, avoiding the maximum activity. To provide a single number for the non-Polar areas, we simply take the average of the Tropical 8PM effect between a minimum solar activity ($\ll 1$ mm bias, 0.62 cm dispersion) and a maximum solar activity (23 cm bias, 33 cm dispersion). The resulting value, ~ 15 cm dispersion is rather conservative for the rest of the Globe, especially in a 6AM-6PM Sun-synchronous orbit.

To provide sets of overall errors induced by these combined effects, the uncertainties in last column of Table 7 are first expressed through a polynomial fit as function of the incidence angle, and then added quadratically to the remaining

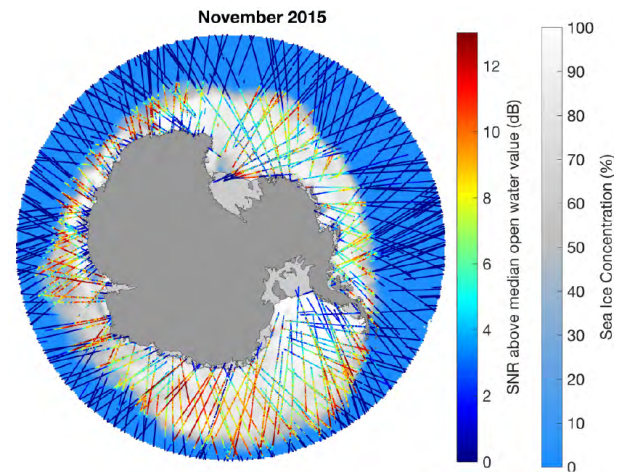


FIGURE 19. Actual spaceborne GNSS-R reflected signals captured aboard TDS-1 across sea ice in the Southern Ocean, surrounding Antarctica. The SNR of the signals reflected off the sea ice are higher or equal to the SNR of signals reflected off the ocean. Unpublished figure from [203], reproduced here with authorization of the authors.

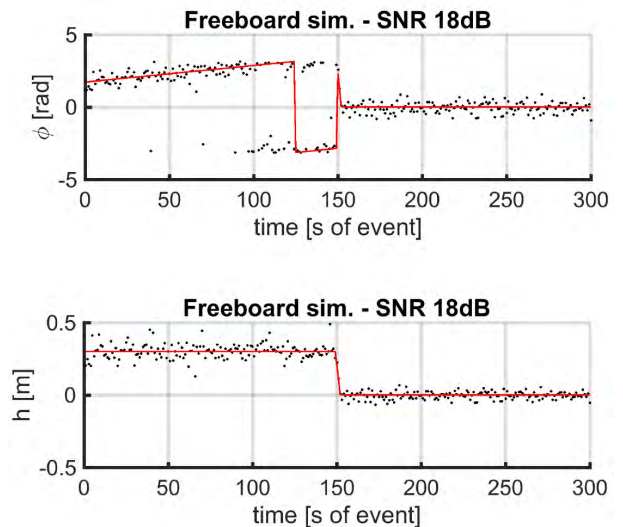


FIGURE 20. Simulation of phase delay observables and their altimetric retrievals in grazing angle geometry (varying around 10° elevation in this case). The surface height is perturbed with a 30 cm step-like feature, and the signal is received at 18 dB SNR. The phase obtained can be tracked, and it presents noise levels between 0.4 to 0.5 rad (top). Bottom: after unwrapping the phase and applying the altimetric inversion, the altimetric profile is recovered at around ~ 4 -5 cm precision (better precisions achieved at slightly higher elevation angles and/or higher SNR).

sources of error (POD, troposphere and ionosphere). The resulting 1 Hz level-2 precisions, with all terms accounted for, are summarized in Table 8.

B. PHASE DELAY LEVEL-2 ALTIMETRIC ACCURACY

As already described in Sections IV-B, the phase delay observables are either very precise or they are not possible to track. The possibility of tracking the phase and the noise level of the phase itself are both driven by the SNR of the signal. On the other hand, as is shown in Figure 19, actual spaceborne data obtained with TDS-1 generally present higher levels of

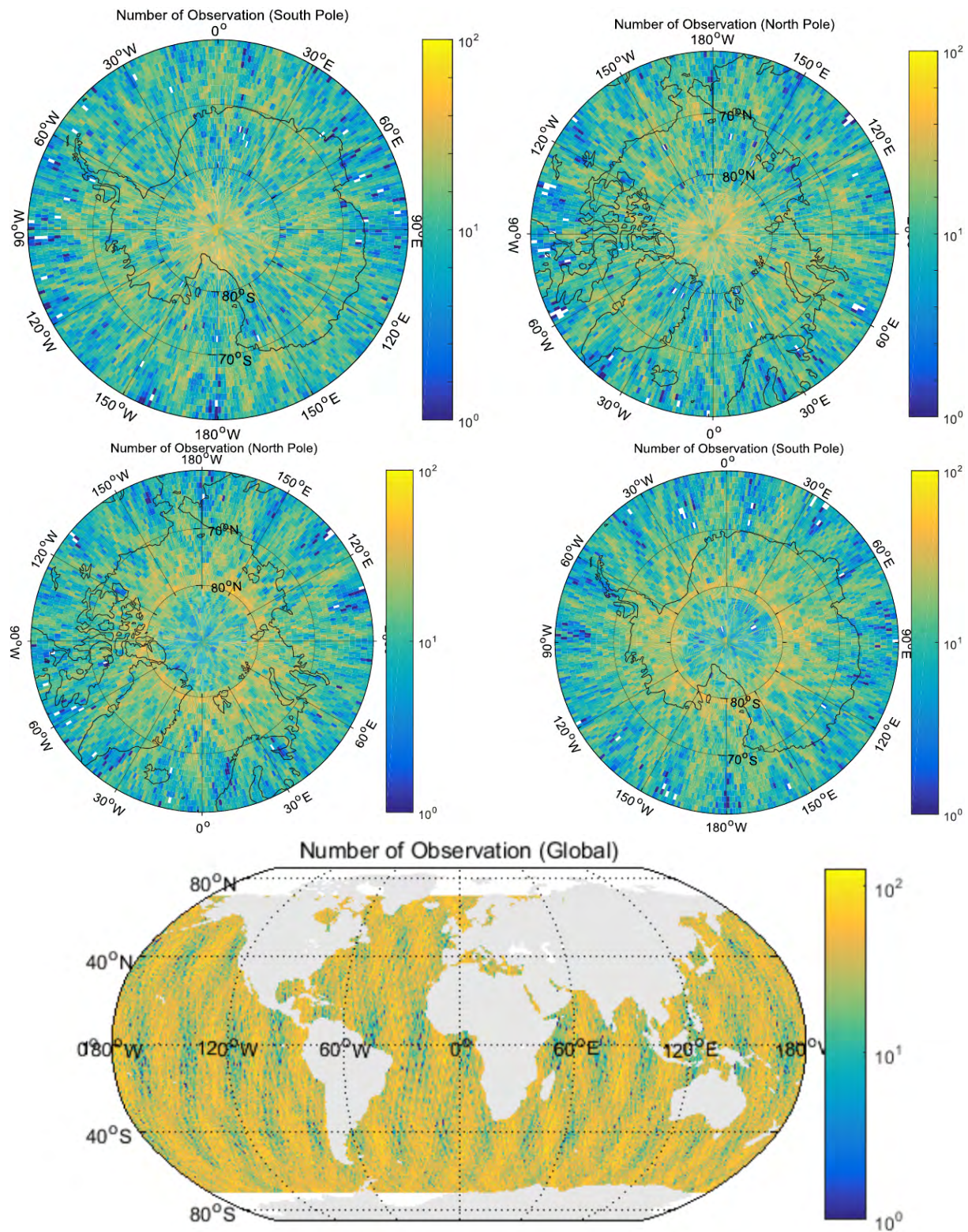


FIGURE 21. Top row: number of 1-second observations obtained at each cell of $30\text{ km} \times 30\text{ km}$ resolution during 3 days in Scenario 1, north pole and south pole (right-left). Central row: same for Scenario-2. Bottom row: number of 1-second observations obtained at each cell of $0.5^\circ \times 0.5^\circ$ resolution cells during 10 days in Scenario-3.

SNR over sea ice than over ocean waters. The worst case SNR over sea ice corresponds the old sea ice, with SNR values similar to those of ocean waters. The simulation exercise

presented here correspond to SNR values compatible with this worst-case scenario. Any other sea ice phase delay altimetric retrieval will present lower levels of noise, thus better

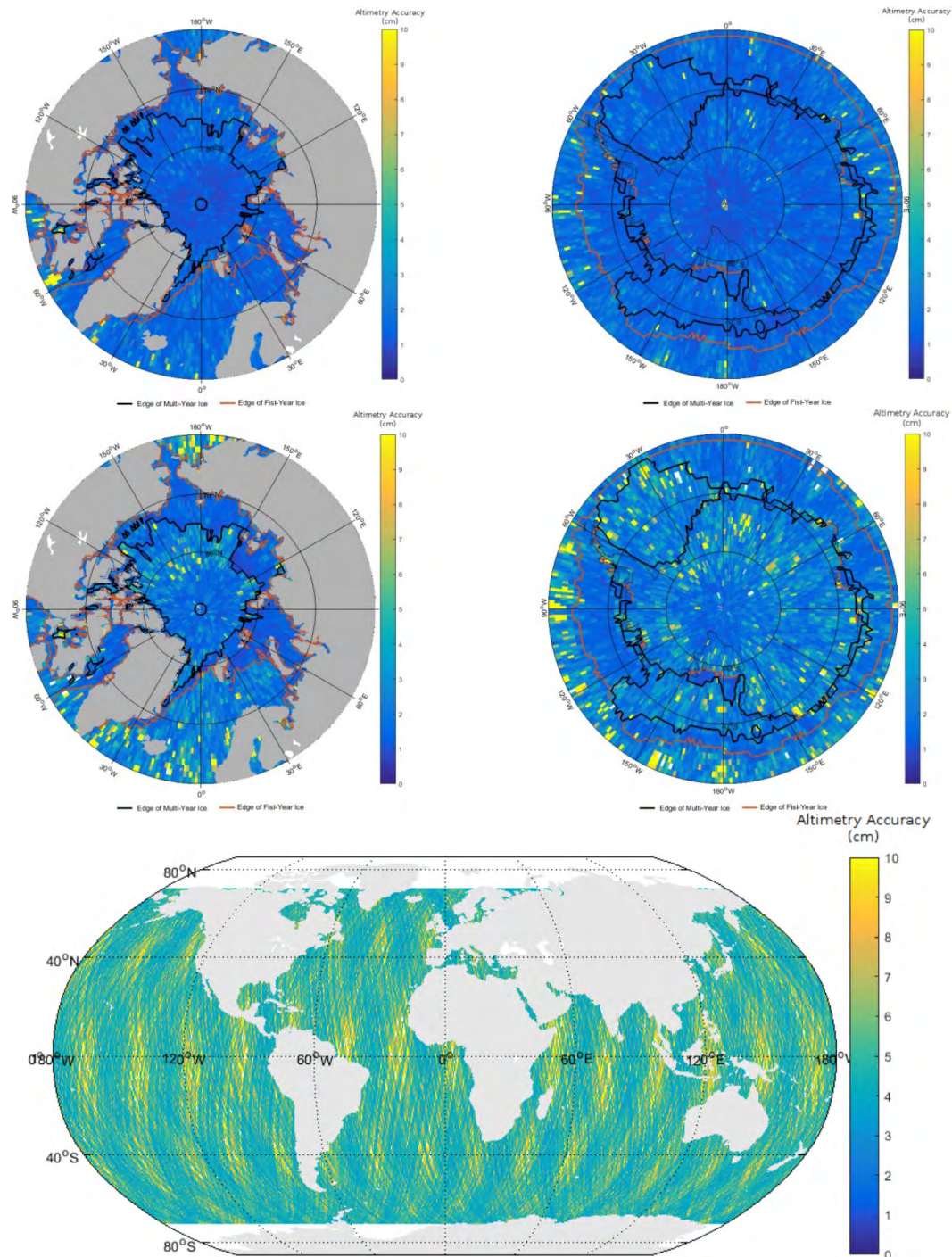


FIGURE 22. Top row: particular realization of the geographical distribution of level-3 altimetric accuracy at each cell of $30 \text{ km} \times 30 \text{ km}$ resolution during 3 days in Scenario 1, north pole and south pole (right-left). Central row: same for Scenario-2. In both cases best ice reflector has been assigned to first year ice and worst case reflector to multi-year ice. The FY and MY contours have been approximated from Nimbus-7 SMMR and DMSP SSM/I-SSMIS ice concentrations provided by NSIDC, considering MY the extension during an arbitrary date of the local summer and FY the extension of another arbitrary date in local winter (dates: 01/08/2015 and 01/01/2015). GNSS-R does not follow a repeatable pattern, therefore the actual distribution of observations will change daily, but keeping the latitudinal statistics. Bottom row: geographical distribution of the accuracy of scenario-3 over $0.5^\circ \times 0.5^\circ$ cells in 10 days accumulated data, for $-70^\circ \leq \text{lat} \leq 70^\circ$. The group delay level-2 altimetric product has been assumed at 34 cm accuracy in 1 Hz [123].

precision. For example, the aforementioned $\sim 3\text{-cm}$ RMS precision at 50Hz rate reported for phase-delay altimetry from TDS-1 data in [30].

Simulations have been run following the approach in [123] and [124]. SNR values set at 18 dB have been used to simulate the coherent scattering along a surface which presents

a step-like height increase of 30 cm. These simulations include the tropospheric, ionospheric and POD systematic effects [123]. After applying the phase delay retrieval algorithms, it is first possible to connect and nearly stop the phases (Figure 20-top). These residual phases are later resolved as height anomalies, recovering the original 30 cm step in the altimetric profile (Figure 20-bottom). The precision of these phase delay measurements are between 0.4 and 0.5 rad, which maps into uncertainties between 1 and 8 cm in 1 second (changing with the geometry, between 60° and 85° incidence). Similar performances are found with shorter surface height steps (20 cm). The performance improves also when higher SNR are assumed. Hereafter we will continue the simulations assuming an equivalent 1 Hz error of ~ 5 cm in the phase delay altimetric retrievals.

C. FULFILLMENT OF THE MISSION REQUIREMENTS

The distributions of 1-second observations obtained for the G-TERN system in a particular set of 3 subsequent days (polar areas) and 10 days (globally) have been simulated. The simulations correspond to three scenarios:

- Scenario-1: Availability of up to 12 simultaneous beams pointing within the grazing angle field of view (5° to 30° elevation) over extended polar areas ($|lat| > 60^\circ$). This means that grazing angle GNSS-R phase-delay altimetry could be done in up to 12 different specular points simultaneously.
- Scenario-2: Availability of a combination of up to 6 grazing angle and up to 6 near-nadir (incidences smaller than 45°) simultaneous reflections over the extended polar areas ($|lat| > 60^\circ$).
- Scenario-3: Availability of up to 12 simultaneous beams pointing to reflections within the near-nadir field of view (incidences smaller than 45°) over the non-polar areas (here defined as $|lat| < 70^\circ$).

The distributions of 1-Hz measurement points for each of these scenarios correspond to those shown in Figure 21. We remind here that GNSS-R does not follow a repeatable pattern, therefore the actual distribution of observations will change daily, but keeping the latitudinal statistics. At this step of the simulations we have considered that all the 1-second observations are uncorrelated. This assumption is too strong, as some of the errors do present spatial or temporal correlations. Nevertheless, this approach permits a quick implementation accounting for all systematic effects without need of simulating natural runs fed by actual tropospheric and ionospheric fields nor POD errors. Therefore, these results might have slightly overestimated the accuracy (underestimate the sigmas), to be partially compensated by certain values of the errors taken on the conservative side.

Using all the 12 G-TERN beams to point at grazing angles of observation, and assuming that the final accuracy of the 1-Hz phase delay observations is at the level of 5 cm (Section VI-B), scenario-1 results in accuracies over $30 \text{ km} \times 30 \text{ km}$ cells in 3 days accumulation that fulfills the mission requirements in 99.1% of the cells.

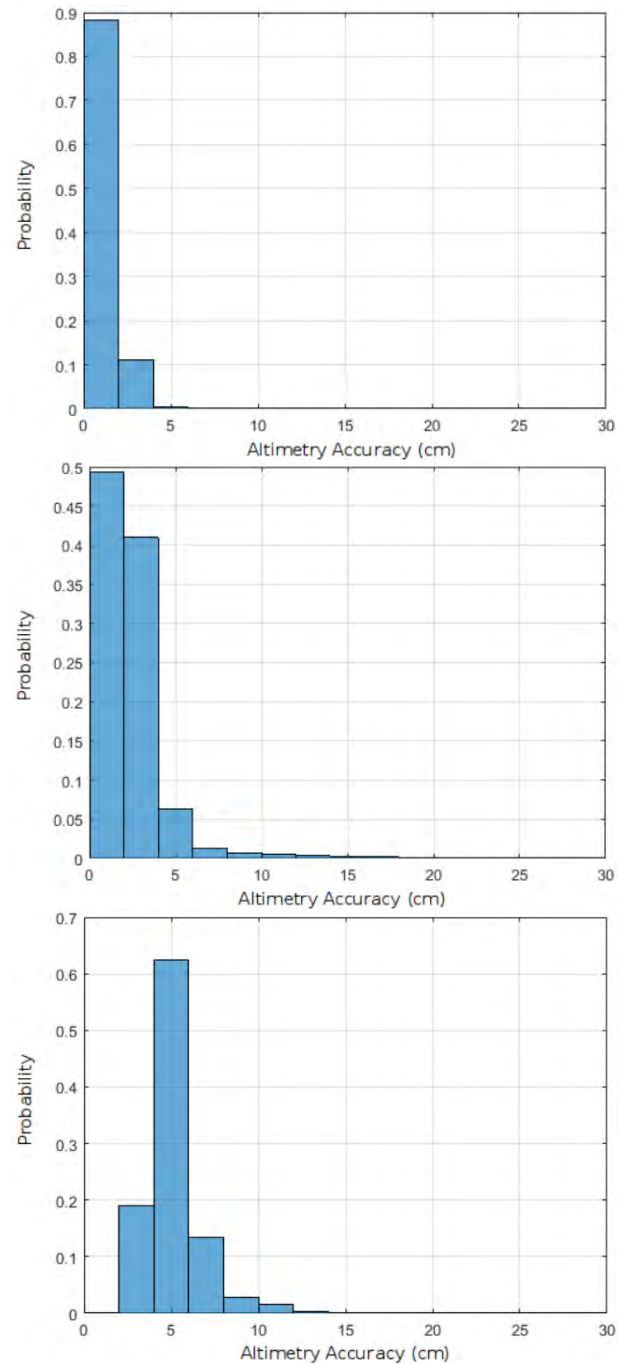


FIGURE 23. Histograms of level-3 altimetric performances over the cells in Figure 22. Top to bottom for scenarios-1 to -3.

In fact, the average precision across the $|lat| > 60^\circ$ regions is 1.6 cm.

For scenario-2, where measurements at near-nadir using group-delay altimetry are combined with phase delay measurements at grazing angles, the simulation has used the following accuracies: measurements done with phase delay observables (Section VI-B): 5 cm at 1 Hz; measurements done with group-delay observables over first year sea ice are considered to correspond to best reflector sea ice reflections, therefore (Table 8-top): 5.5 cm at 1 Hz; measurements done with group-delay observables over multi-year sea ice are

considered to correspond to worst reflector sea ice reflectors, therefore (Table 8-2nd row): $32.5 - 0.29\theta + 3.5E - 3\theta^2 + 1.9E - 4\theta^3$ cm at 1 Hz, ranging from ~ 30 cm at nadir to ~ 44 cm at 45° incidence; measurements done with group-delay observables over ocean waters (Table 8-3rd row) and ice sheets: 30.4 cm. The overall results of combining these 1-second accuracies in $30 \text{ km} \times 30 \text{ km}$ cells during 3 days of accumulated data shows that scenario-2 fulfills the altimetric requirements of the mission in a large extent, with 95.5% of the cells performing better than the mission requirements, and an average accuracy of 2.7 cm over regions with $|lat| > 60^\circ$.

Finally, the scenario-3, over global waters (here defined as $-70^\circ \leq lat \leq 70^\circ$) and $0.5^\circ \times 0.5^\circ$ cells accumulated in 10 days, results in similar numbers: 97.1% of the cells present accuracies below 10 cm (requirement) while the average accuracy over the cells is 5.3 cm. Figure 22 shows the geographic distributions of the resulting level-3 altimetric accuracies for each scenario, while Figure 23 displays their histogram. The optimal combination of grazing angle phase delay measurements (finer precision) and near nadir group delay measurements (better roughness estimates) would be investigated in future stages of the mission.

VII. CONCLUSIONS

This study summarizes the main aspects of the GNSS Trans-polar Earth Reflectometry explorIng system (G-TERN), a mission proposal submitted in 2017 in response to the ESA Earth Explorer 9 (Revised Call). The mission is foreseen to implement the interferometric GNSS reflectometry technique to address key scientific questions on the inter-relationship between the cryosphere and other main components of the climate system, in view of the global warming. The main focus of G-TERN is set on the sea ice, its dynamic variations and how they both module and are modulated by its surrounding environment, the global atmospheric and ocean circulations as well as extreme weather systems.

The G-TERN satellite should provide altimetric, scatterometric and polarimetric GNSS-Reflectometry based geophysical data products, characterizing the sea ice, oceans, ice sheets and land surface, covering the poles in grids of $30 \text{ km} \times 30 \text{ km}$ cells in just 3 days, and the rest of the globe in 10 days over grids of $0.5^\circ \times 0.5^\circ$ cells. The foreseen observation techniques of G-TERN and their preliminary implementation have been introduced. The technical concept is substantially different from other recent GNSS-R missions and includes several novelties and innovation aspects. We highlight in this context: (1) interferometric GNSS reflectometry from space, which provides finer horizontal resolution and higher altimetric accuracy; (2) parallel provision of altimetric, scatterometric and polarimetric GNSS-R data products; (3) twelve simultaneous GNSS-R high-gain beams electronically synthesized and steered to enable observations with unprecedented coverage; (4) combination of slant phase-delay observations and near-nadir group-delay measurements for ice/ocean altimetry with high accuracy; and (5) symbiotic use of GNSS

reflectometry and radio-occultation for combined monitoring of the Earth surface and atmosphere/ionosphere.

The G-TERN spacecraft is based on a modernized platform of space-proven components. The main payload, the combined GNSS-R/RO instrument, has strong heritage from two ESA mission studies: the PARIS-IOD and GEROS-ISS concepts. The proposed orbit is near-polar at 600 km altitude, optimally Sun-synchronous at 6AM/6PM.

A set of specific mission simulations was conducted during the proposal preparation to provide first estimates of the altimetric performance of G-TERN over sea ice and oceans. The required geophysical observational needs are essentially met according to the results of these calculations. Accuracies were obtained, better or equal to 10 cm in more than 95% of the sea ice cells in the polar grid in three days integration, and in more than 97% of the global ocean cells in ten days integration. The G-TERN measurements are also expected to prove a set of secondary mission goals, which include the provision of currently not available innovative cryosphere and wetland related data products. These observations would represent a breakthrough in their irrespective science fields. The G-TERN, with its versatile mission scope and unique payload may act as a forerunner for a potential next generation of 'low cost' Earth Observation Systems.

ACKNOWLEDGMENTS

The authors would like to thank SSTL for providing GNSS-R data acquired from the TDS-1 mission that have been used in this study.

REFERENCES

- [1] M. Martin-Neira, "A passive reflectometry and interferometry system (PARIS): Application to ocean altimetry," *ESA J.*, vol. 17, pp. 331–355, Aug. 1993.
- [2] J. L. Garrison, S. J. Katzberg, and M. I. Hill, "Effect of sea roughness on bistatically scattered range coded signals from the global positioning system," *Geophys. Res. Lett.*, vol. 25, no. 13, pp. 2257–2260, Jul. 1998.
- [3] J. L. Garrison, E. Cardellach, S. Gleason, and S. Katzberg, "Foreword to special issue on reflectometry using global navigation satellite systems and other signals of opportunity (GNSS+R)," *IEEE J. Sel. Topics Appl. Earth Observ. Remote Sens.*, vol. 7, no. 5, pp. 1412–1415, May 2014, doi: [10.1109/JSTARS.2014.2325996](https://doi.org/10.1109/JSTARS.2014.2325996).
- [4] E. Cardellach, S. Vey, and J. Wickert, "Foreword to the special issue on GNSS reflectometry," *IEEE J. Sel. Topics Appl. Earth Observ. Remote Sens.*, vol. 9, no. 10, pp. 4519–4524, Oct. 2016, doi: [10.1109/JSTARS.2016.2607618](https://doi.org/10.1109/JSTARS.2016.2607618).
- [5] V. U. Zavorotny, S. Gleason, E. Cardellach, and A. Camps, "Tutorial on remote sensing using GNSS bistatic radar of opportunity," *IEEE Geosci. Remote Sens. Mag.*, vol. 2, no. 4, pp. 8–45, Dec. 2014, doi: [10.1109/MGRS.2014.2374220](https://doi.org/10.1109/MGRS.2014.2374220).
- [6] D. Gebre-Egziabher and S. Gleason, Eds., *GNSS Applications and Methods*. Norwood, MA, USA: Artech House, 2009, p. 530.
- [7] S. Jin, E. Cardellach, and F. Xie, *GNSS Remote Sensing: Theory, Methods and Applications*. New York, NY, USA: Springer, 2014, p. 276, doi: [10.1007/978-94-007-7482-7](https://doi.org/10.1007/978-94-007-7482-7).
- [8] P. J. G. Teunissen and O. Montenbruck, Eds., *Springer Handbook of Global Navigation Satellite Systems*. Cham, Switzerland: Springer, 2017, pp. 31 and 1327, doi: [10.1007/978-3-319-42928-1](https://doi.org/10.1007/978-3-319-42928-1).
- [9] A. Komjathy, J. Maslanik, V. U. Zavorotny, P. Axelrad, and S. J. Katzberg, "Sea ice remote sensing using surface reflected GPS signals," in *Proc. IEEE IGARSS*, Honolulu, HI, USA, Jul. 2000, pp. 2855–2857.

- [10] M. B. Rivas, "Bistatic scattering of global positioning system signals from Arctic sea ice," Ph.D. dissertation, Dept. Aerosp. Eng., Univ. Colorado Boulder, Boulder, CO, USA, 2007.
- [11] M. B. Rivas, J. A. Maslanik, and P. Axelrad, "Bistatic scattering of GPS signals off Arctic Sea ice," *IEEE Trans. Geosci. Remote Sens.*, vol. 48, no. 3, pp. 1548–1553, Mar. 2010.
- [12] E. Cardellach, C. O. Ao, M. de la Torre Juárez, and G. A. Hajj, "Carrier phase delay altimetry with GPS-reflection/occultation interferometry from low Earth orbiters," *Geophys. Res. Lett.*, vol. 31, no. 10, p. L10402, May 2004, doi: [10.1029/2004GL019775](https://doi.org/10.1029/2004GL019775).
- [13] S. Gleason, "Remote sensing of ocean, ice, and land surfaces using bistatically scattered GNSS signals from low earth orbit," Ph.D. dissertation, Univ. Surrey, Guildford, U.K., 2006. [Online]. Available: <http://ethos.bl.uk/OrderDetails.do?uin=uk.bl.ethos.435334>
- [14] S. Gleason, "Towards sea ice remote sensing with space detected GPS signals: Demonstration of technical feasibility and initial consistency check using low resolution sea ice information," *Remote Sens.*, vol. 2, no. 8, pp. 2017–2039, Aug. 2010. [Online]. Available: <http://www.mdpi.com/2072-4292/2/8/2017/>
- [15] E. Cardellach, F. Fabra, O. Nogués-Correig, S. Oliveras, S. Ribó, and A. Rius, "GNSS-R ground-based and airborne campaigns for ocean, land, ice, and snow techniques: Application to the GOLD-RTR data sets," *Radio Sci.*, vol. 46, no. 6, Dec. 2011. [Online]. Available: <http://onlinelibrary.wiley.com/doi/10.1029/2011RS004683/supinfo> and <http://onlinelibrary.wiley.com/doi/10.1029/2011RS004683/pdf>, doi: [10.1029/2011RS004683](https://doi.org/10.1029/2011RS004683).
- [16] F. Fabra, "GNSS-R as a source of opportunity for remote sensing of the cryosphere," Ph.D. dissertation, Dept. Teoria Senyal Comun., Polytech. Univ. Catalonia, Barcelona, Spain, 2013. [Online]. Available: <http://www.tdx.cat/handle/10803/117605>
- [17] F. Fabra et al., "Phase altimetry with dual polarization GNSS-R over sea ice," *IEEE Trans. Geosci. Remote Sens.*, vol. 50, no. 6, pp. 2112–2121, Jun. 2012, doi: [10.1109/TGRS.2011.2172797](https://doi.org/10.1109/TGRS.2011.2172797).
- [18] K. M. Larson and F. G. Nievinski, "GPS snow sensing: Results from the EarthScope plate boundary observatory," *GPS Solution*, vol. 17, no. 1, pp. 41–52, Jan. 2013, doi: [10.1007/s1029101202597](https://doi.org/10.1007/s1029101202597).
- [19] K. M. Larson and E. E. Small, "Estimation of snow depth using L1 GPS signal-to-noise ratio data," *IEEE J. Sel. Topics Appl. Earth Observ. Remote Sens.*, vol. 9, no. 10, pp. 4802–4808, Oct. 2016, doi: [10.1109/JSTARS.2016.2508673](https://doi.org/10.1109/JSTARS.2016.2508673).
- [20] S. Vey, A. Güntner, J. Wickert, T. Blume, H. Thoss, and M. Ramatschi, "Monitoring snow depth by GNSS reflectometry in built-up areas: A case study for Wettzell, Germany," *IEEE J. Sel. Topics Appl. Earth Observ. Remote Sens.*, vol. 9, no. 10, pp. 4809–4816, Oct. 2016, doi: [10.1109/JSTARS.2016.2516041](https://doi.org/10.1109/JSTARS.2016.2516041).
- [21] M. Wiehl, B. Legrésy, and R. Dietrich, "Potential of reflected GNSS signals for ice sheet remote sensing," *Prog. Electromagn. Res.*, vol. 40, pp. 177–205, 2003. [Online]. Available: <http://citeseerx.ist.psu.edu/viewdoc/download?doi=10.1.1.843.5779&rep=rep1&type=pdf>
- [22] E. Cardellach, F. Fabra, A. Rius, S. Pettinato, and S. D'Addio, "Characterization of dry-snow sub-structure using GNSS reflected signals," *Remote Sens. Environ.*, vol. 124, pp. 122–134, Sep. 2012, doi: [10.1016/j.rse.2012.05.012](https://doi.org/10.1016/j.rse.2012.05.012).
- [23] C. Chew et al., "SMAP radar receiver measures land surface freeze/thaw state through capture of forward-scattered L-band signals," *Remote Sens. Environ.*, vol. 198, pp. 333–344, Sep. 2017, doi: [10.1016/j.rse.2017.06.020](https://doi.org/10.1016/j.rse.2017.06.020).
- [24] H. Carreno-Luengo, S. Lowe, C. Zuffada, S. Esterhuizen, and S. Oveisgharan, "Spaceborne GNSS-R from the SMAP mission: First assessment of polarimetric scatterometry over land and cryosphere," *Remote Sens.*, vol. 9, no. 4, p. 362, 2017, doi: [10.3390/rs9040362](https://doi.org/10.3390/rs9040362).
- [25] A. Rius, E. Cardellach, F. Fabra, W. Li, S. Ribó, and M. Hernández-Pajares, "GNSS-R ice sheet altimetry in greenland using TDS-1 data," *Remote Sens.*, vol. 9, no. 7, p. 742, 2017, doi: [10.3390/rs9070742](https://doi.org/10.3390/rs9070742).
- [26] Q. Yan and W. Huang, "Spaceborne GNSS-R sea ice detection using delay-Doppler maps: First results from the U.K. TechDemoSat-1 mission," *IEEE J. Sel. Topics Appl. Earth Observ. Remote Sens.*, vol. 9, no. 10, pp. 4795–4801, Oct. 2016, doi: [10.1109/JSTARS.2016.2582690](https://doi.org/10.1109/JSTARS.2016.2582690).
- [27] A. Alonso-Arroyo, V. U. Zavorotny, and A. Camps, "Sea ice detection using U.K. TDS-1 GNSS-R data," *IEEE Trans. Geosci. Remote Sens.*, vol. 55, no. 9, pp. 4989–5001, Sep. 2017, doi: [10.1109/TGRS.2017.2699122](https://doi.org/10.1109/TGRS.2017.2699122).
- [28] Q. Yan, W. Huang, and C. Moloney, "Neural networks based sea ice detection and concentration retrieval from GNSS-R delay-Doppler maps," *IEEE J. Sel. Topics Appl. Earth Observ. Remote Sens.*, vol. 10, no. 8, pp. 3789–3798, Aug. 2017, doi: [10.1109/JSTARS.2017.2689009](https://doi.org/10.1109/JSTARS.2017.2689009).
- [29] C. Hu, C. Benson, C. Rizos, and L. Qiao, "Single-pass sub-meter space-based GNSS-R ice altimetry: Results from TDS-1," *IEEE J. Sel. Topics Appl. Earth Observ. Remote Sens.*, vol. 10, no. 8, pp. 3782–3788, Aug. 2017, doi: [10.1109/JSTARS.2017.2690917](https://doi.org/10.1109/JSTARS.2017.2690917).
- [30] W. Li, E. Cardellach, F. Fabra, A. Rius, S. Ribó, and M. Martín-Neira, "First spaceborne phase altimetry over sea ice using TechDemoSat-1 GNSS-R signals," *Geophys. Res. Lett.*, vol. 44, no. 16, pp. 8369–8376, Aug. 2017.
- [31] J. Wickert et al., "GNSS transpolar earth reflectometry exploring system (G-TERN)," in *Proposal Submitted to the ESA Earth Explorer 9, Revised Call*, Jun. 2017.
- [32] *ESA Earth Explorer 9, Revised Call*, ESA, Paris, France, Dec. 2016.
- [33] M. Martín-Neira, S. D'Addio, C. Buck, N. Floury, and R. Prieto-Cerdeira, "The PARIS ocean altimeter in-orbit demonstrator," *IEEE Trans. Geosci. Remote Sens.*, vol. 49, no. 6, pp. 2209–2237, Jun. 2011, doi: [10.1109/TGRS.2010.2092431](https://doi.org/10.1109/TGRS.2010.2092431).
- [34] J. Wickert et al., "GEROS-ISS: GNSS reflectometry, radio occultation, and scatterometry onboard the international space station," *IEEE J. Sel. Topics Appl. Earth Observ. Remote Sens.*, vol. 9, no. 10, pp. 4552–4581, Oct. 2016, doi: [10.1109/JSTARS.2016.2614428](https://doi.org/10.1109/JSTARS.2016.2614428).
- [35] V. Kattsov, G. Flato, S. Bony, S. Gille, B. Kirtman, V. Ryabinin, A. Scaife, and K. Trenberth, (2012). *Cryosphere in a Changing Climate: A Grand Challenge of Climate Science*. World Climate Research Program (WCRP). [Online]. Available: <https://www.wcrp-climate.org/melting-ice-global-consequences-documents>
- [36] IPCC, *Climate Change 2013: The Physical Science Basis. Contribution of Working Group I to the Fifth Assessment Report of the Intergovernmental Panel on Climate Change*, T. F. Stocker et al., Eds. Cambridge, U.K.: Cambridge Univ. Press, 2013, p. 1535. [Online]. Available: https://www.ipcc.ch/pdf/assessmentreport/ar5/wg1/WG1AR5_Frontmatter_FINAL.pdf
- [37] G. Flato, V. Kattsov, and J. Baeseman, (2016). *Melting Ice—Global Consequences Initial Implementation Plan for the WCRP Grand Challenge on the Cryosphere in a Changing Climate*, Version 3. World Climate Research Program (WCRP). [Online]. Available: <https://www.wcrpclimate.org/melting-ice-global-consequences-documents>
- [38] I. Cvijanovic and K. Caldeira, "Atmospheric impacts of sea ice decline in CO2 induced global warming," *Climate Dyn.*, vol. 44, nos. 5–6, pp. 1173–1186, Mar. 2015, doi: [10.1007/s00382-015-2489-1](https://doi.org/10.1007/s00382-015-2489-1).
- [39] V. Guemas and D. Salas-Méla, "Simulation of the Atlantic meridional overturning circulation in an atmosphere-ocean global coupled model. Part I: a mechanism governing the variability of ocean convection in a preindustrial experiment," *Climate Dyn.*, vol. 31, no. 2, pp. 29–48, Jul. 2008.
- [40] D. M. Lawrence, A. G. Slater, R. A. Tomas, M. M. Holland, and C. Deser, "Accelerated Arctic land warming and permafrost degradation during rapid sea ice loss," *Geophys. Res. Lett.*, vol. 35, no. 11, p. L11506, Jun. 2008, doi: [10.1029/2008GL033985](https://doi.org/10.1029/2008GL033985).
- [41] C. Deser, R. Tomas, M. Alexander, and D. Lawrence, "The seasonal atmospheric response to projected Arctic sea ice loss in the late twenty-first century," *J. Climate*, vol. 23, no. 2, pp. 333–351, 2010.
- [42] *AMAP Arctic Monitoring and Assessment Programme, Snow, Water, Ice and Permafrost in the Arctic (SWIPA): Climate Change and the Cryosphere*, AMAP, Oslo, Norway, 2011.
- [43] J. A. Francis and S. J. Vavrus, "Evidence linking Arctic amplification to extreme weather in mid-latitudes," *Geophys. Res. Lett.*, vol. 39, p. L06801, Mar. 2012, doi: [10.1029/2012GL051000](https://doi.org/10.1029/2012GL051000).
- [44] M. Jakobsson et al., "The international bathymetric chart of the Arctic Ocean (IBCAO) version 3.0," *Geophys. Res. Lett.*, vol. 39, p. L12609, Jun. 2012, doi: [10.1029/2012GL052219](https://doi.org/10.1029/2012GL052219).
- [45] T. Koenigk, C. K. Beatty, M. Caian, R. Döschner, and K. Wyser, "Potential decadal predictability and its sensitivity to sea ice albedo parameterization in a global coupled model," *Climate Dyn.*, vol. 38, nos. 11–12, pp. 2389–2408, 2012.
- [46] W. Maslowski, J. C. Kinney, M. Higgins, and A. Roberts, "The future of Arctic sea ice," *Annu. Rev. Earth Planetary Sci.*, vol. 40, pp. 625–654, Mar. 2012.

- [47] S. V. Nghiem, I. G. Rigor, D. K. Perovich, P. Clemente-Colón, J. W. Weatherly, and G. Neumann, "Rapid reduction of Arctic perennial sea ice," *Geophys. Res. Lett.*, vol. 34, p. L19504, Oct. 2007, doi: [10.1029/2007GL031138](https://doi.org/10.1029/2007GL031138).
- [48] S. V. Nghiem et al., "Field and satellite observations of the formation and distribution of Arctic atmospheric bromine above a rejuvenated sea ice cover," *J. Geophys. Res.*, vol. 117, p. D00S05, Sep. 2012, doi: [10.1029/2011JD016268](https://doi.org/10.1029/2011JD016268).
- [49] S. V. Nghiem, D. K. Hall, I. G. Rigor, P. Li, and G. Neumann, "Effects of Mackenzie River discharge and bathymetry on sea ice in the Beaufort Sea," *Geophys. Res. Lett.*, vol. 41, no. 3, pp. 873–879, Feb. 2014, doi: [10.1002/2013GL058956](https://doi.org/10.1002/2013GL058956).
- [50] D. K. Perovich, B. Light, H. Eicken, K. F. Jones, K. Ruciman, and S. V. Nghiem, "Increasing solar heating of the Arctic Ocean and adjacent seas, 1979–2005: Attribution and role in the ice-albedo feedback," *Geophys. Res. Lett.*, vol. 34, no. 19, p. L19505, Oct. 2007, doi: [10.1029/2007GL031480](https://doi.org/10.1029/2007GL031480).
- [51] J. King, "A resolution of the Antarctic paradox," *Nature*, vol. 505, pp. 491–492, Jan. 2014.
- [52] J. P. Liu and J. A. Curry, "Resolving the paradox of Antarctic sea-ice growth," *Bull. Amer. Meteorol. Soc.*, vol. 92, pp. 1411–1412, Nov. 2011.
- [53] T. Maksym, S. E. Stammerjohn, S. Ackley, and R. Massom, "Antarctic sea ice—A polar opposite?" *Oceanography*, vol. 25, no. 3, pp. 140–151, Sep. 2012.
- [54] J. E. Walsh, "A comparison of Arctic and Antarctic climate change, present and future," *Antarctic Sci.*, vol. 21, no. 3, pp. 179–188, 2009, doi: [10.1017/S0954102009001874](https://doi.org/10.1017/S0954102009001874).
- [55] National Research Council, *Seasonal to Decadal Predictions of Arctic Sea Ice: Challenges and Strategies*. Washington, DC, USA: Academies, 2012. [Online]. Available: <https://www.nap.edu/catalog/13515/seasonal-to-decadal-predictions-of-arctic-sea-ice-challenges-and->, doi: <https://doi.org/10.17226/13515>.
- [56] J. Maslanik, J. Stroeve, C. Fowler, and W. Emery, "Distribution and trends in Arctic sea ice age through spring 2011," *Geophys. Res. Lett.*, vol. 38, no. 13, p. L13502, 2011, doi: [10.1029/2011GL047735](https://doi.org/10.1029/2011GL047735).
- [57] C. Haas, A. Pfaffling, S. Hendricks, L. Rabenstein, J.-L. Etienne, and I. Rigor, "Reduced ice thickness in Arctic Transpolar Drift favors rapid ice retreat," *Geophys. Res. Lett.*, vol. 35, no. 17, p. L17501, 2008, doi: [10.1029/2008GL034457](https://doi.org/10.1029/2008GL034457).
- [58] J. C. Comiso, "Large decadal decline of the Arctic multiyear ice cover," *J. Climate*, vol. 25, pp. 1176–1193, Sep. 2012.
- [59] H. Goosse, O. Arzel, C. M. Bitz, A. de Montety, and M. Vancoppenolle, "Increased variability of the Arctic summer ice extent in a warmer climate," *Geophys. Res. Lett.*, vol. 36, no. 23, p. L23702, 2009, doi: [10.1029/2009GL040546](https://doi.org/10.1029/2009GL040546).
- [60] J. K. Hutchings and I. G. Rigor, "Role of ice dynamics in anomalous ice conditions in the Beaufort Sea during 2006 and 2007," *J. Geophys. Res.*, vol. 117, no. C8, p. C00E04, 2012, doi: [10.1029/2011JC007182](https://doi.org/10.1029/2011JC007182), 2012.
- [61] M. M. Holland, D. A. Bailey, and S. Vavrus, "Inherent sea ice predictability in the rapidly changing arctic environment of the community climate system model, version 3," *Climate Dyn.*, vol. 36, nos. 7–8, pp. 1239–1253, 2011.
- [62] S. V. Nghiem et al., "Studying bromine, ozone, and mercury chemistry in the arctic," *Trans. Amer. Geophys. Union*, vol. 94, no. 33, pp. 289–291, Aug. 2013.
- [63] S. V. Nghiem, I. G. Rigor, P. Clemente-Colón, G. Neumann, and P. P. Li, "Geophysical constraints on the Antarctic sea ice cover," *Remote Sens. Environ.*, vol. 181, pp. 281–292, Aug. 2016, doi: [10.1016/j.rse.2016.04.005](https://doi.org/10.1016/j.rse.2016.04.005).
- [64] National Academies of Sciences, *Engineering, and Medicine, Antarctic Sea Ice Variability in the Southern Ocean-Climate System: Proceedings of a Workshop*. Washington, DC, USA: Academies, 2017. [Online]. Available: <https://www.nap.edu/catalog/24696/antarctic-sea-ice-variability-in-the-southern-ocean-climatesystem>, doi: <https://doi.org/10.17226/24696>.
- [65] A. Khazendar, M. P. Schodlok, I. Fenty, S. R. M. Ligtenberg, E. Rignot, and M. R. van den Broeke, "Observed thinning of Totten Glacier is linked to coastal polynya variability," *Nature Commun.*, vol. 4, Dec. 2013, Art. no. 2857, doi: [10.1038/ncomms3857](https://doi.org/10.1038/ncomms3857).
- [66] R. A. Massom et al., "Examining the interaction between multi-year land-fast sea ice and the Mertz Glacier Tongue, East Antarctica: Another factor in ice sheet stability?" *J. Geophys. Res.*, vol. 115, no. C12, p. C12027, doi: [10.1029/2009JC006083](https://doi.org/10.1029/2009JC006083).
- [67] B. W. J. Miles, C. R. Stokes, and S. S. R. Jamieson, "Pan-ice-sheet glacier terminus change in East Antarctica reveals sensitivity of Wilkes Land to sea-ice changes," *Sci. Adv.*, vol. 2, no. 5, p. e1501350, 2016, doi: [10.1126/sciadv.1501350](https://doi.org/10.1126/sciadv.1501350).
- [68] D. K. Perovich, J. A. Richter-Menge, K. F. Jones, and B. Light, "Sunlight, water, and ice: Extreme Arctic sea ice melt during the summer of 2007," *Geophys. Res. Lett.*, vol. 35, no. 11, p. L1150, doi: [10.1029/2008GL034007](https://doi.org/10.1029/2008GL034007).
- [69] J. Zhang, R. Lindsay, M. Steele, and A. Schweiger, "What drove the dramatic retreat of Arctic sea ice during summer 2007?" *Geophys. Res. Lett.*, vol. 35, no. 11, p. L11505, 2008, doi: [10.1029/2008GL034005](https://doi.org/10.1029/2008GL034005).
- [70] R. W. Lindsay, J. Zhang, A. Schweiger, M. Steele, and H. Stern, "Arctic sea ice retreat in 2007 follows thinning trend," *J. Climate*, vol. 22, pp. 165–176, Jan. 2009.
- [71] M. Ogi and J. M. Wallace, "The role of summer surface wind anomalies in the summer Arctic sea ice extent in 2010 and 2011," *Geophys. Res. Lett.*, vol. 39, no. 9, p. L09704, 2012.
- [72] M. M. Holland, C. M. Bitz, and B. Tremblay, "Future abrupt reductions in the summer Arctic sea ice," *Geophys. Res. Lett.*, vol. 33, no. 23, p. L23503, 2006, doi: [10.1029/2006GL028024](https://doi.org/10.1029/2006GL028024).
- [73] D. K. Perovich, S. V. Nghiem, T. Markus, and A. Schweiger, "Seasonal evolution and interannual variability of the local solar energy absorbed by the Arctic sea ice–ocean system," *J. Geophys. Res.*, vol. 112, no. C3, p. C03005, doi: [10.1029/2006JC003558](https://doi.org/10.1029/2006JC003558).
- [74] D. K. Perovich and C. Polashenski, "Albedo evolution of seasonal Arctic sea ice," *Geophys. Res. Lett.*, vol. 39, p. no. 8, p. L08501, 2012, doi: [10.1029/2012GL051432](https://doi.org/10.1029/2012GL051432).
- [75] M. P. Meredith and A. M. Hogg, "Circumpolar response of Southern Ocean eddy activity to a change in the Southern Annular Mode," *Geophys. Res. Lett.*, vol. 33, no. 16, p. L16608, 2006, doi: [10.1029/2006GL026499](https://doi.org/10.1029/2006GL026499).
- [76] R. Farneti, T. L. Delworth, A. J. Rosati, S. M. Griffies, and F. Zeng, "The role of mesoscale eddies in the rectification of the Southern ocean response to climate change," *J. Phys. Oceanogr.*, vol. 40, no. 7, pp. 1539–1557, 2010, doi: [10.1175/2010JPO4353.1](https://doi.org/10.1175/2010JPO4353.1).
- [77] J. Walsh et al., "Chapter 2: Our changing climate," in *Climate Change Impacts in the United States: The Third National Climate Assessment*, J. M. Melillo, T. Richmond, and G. W. Yohe, Eds. U.S. Global Change Research Program, 2014, pp. 19–67, doi: [10.7930/J0KW5CXT](https://doi.org/10.7930/J0KW5CXT).
- [78] M. Wang and J. E. Overland, "A sea ice free summer Arctic within 30 years: An update from CMIP5 models," *Geophys. Res. Lett.*, vol. 39, no. 18, p. L18501, 2012. [Online]. Available: <http://onlinelibrary.wiley.com/doi/10.1029/2012GL052868/pdf>, doi: [10.1029/2012GL052868](https://doi.org/10.1029/2012GL052868).
- [79] J. E. Overland and M. Wang, "When will the summer Arctic be nearly sea ice free?" *Geophys. Res. Lett.*, vol. 40, no. 10, pp. 2097–2101. [Online]. Available: <http://onlinelibrary.wiley.com/doi/10.1002/grl.50316/pdf>, doi: [10.1002/grl.50316](https://doi.org/10.1002/grl.50316).
- [80] M. Wang and J. E. Overland, "A sea ice free summer Arctic within 30 years?" *Geophys. Res. Lett.*, vol. 36, no. 7, p. L07502, 2009. [Online]. Available: <http://onlinelibrary.wiley.com/doi/10.1029/2009GL037820/pdf>, doi: [10.1029/2009GL037820](https://doi.org/10.1029/2009GL037820).
- [81] J. C. Stroeve et al., "Trends in Arctic sea ice extent from CMIP5, CMIP3 and observations," *Geophys. Res. Lett.*, vol. 39, no. 6, p. L16502, 2012, doi: [10.1029/2012GL052676](https://doi.org/10.1029/2012GL052676).
- [82] A. M. Semmling et al., "Sea surface topography retrieved from GNSS reflectometry phase data of the GEOHALO flight mission," *Geophys. Res. Lett.*, vol. 41, no. 3, pp. 954–960, 2014, doi: [10.1002/2013GL058725](https://doi.org/10.1002/2013GL058725).
- [83] S. D'Addio, M. Martin-Neira, M. di Bisceglie, C. Galdi, and F. M. Alemany, "GNSS-R altimeter based on Doppler multi-looking," *IEEE J. Sel. Topics Appl. Earth Observ. Remote Sens.*, vol. 7, no. 5, pp. 1452–1460, May 2014, doi: [10.1109/JSTARS.2014.2309352](https://doi.org/10.1109/JSTARS.2014.2309352).
- [84] S. B. Healy, J. Wickert, G. Michalak, T. Schmidt and G. Beyerle, "Combined forecast impact of GRACE-A and CHAMP GPS radio occultation bending angle profiles," *Atmos. Sci. Lett.*, vol. 8, no. 2, pp. 43–50, 2007, doi: [10.1002/asl.149](https://doi.org/10.1002/asl.149).
- [85] A. K. Steiner, B. C. Lacker, F. Ladstädter, B. Scherllin-Pirscher, U. Foelsche, and G. Kirchengast, "GPS radio occultation for climate monitoring and change detection," *Radio Sci.*, vol. 46, no. 6, p. RS0D24, 2011, doi: [10.1029/2010RS004614](https://doi.org/10.1029/2010RS004614).
- [86] A. K. Steiner et al., "Quantification of structural uncertainty in climate data records from GPS radio occultation," *Atmos. Chem. Phys.*, vol. 13, pp. 1469–1484, 2013, doi: [10.5194/acp-13-1469-2013](https://doi.org/10.5194/acp-13-1469-2013).

- [87] S.-P. Ho et al., "Reproducibility of GPS radio occultation data for climate monitoring: Profile-to-profile inter-comparison of CHAMP climate records 2002 to 2008 from six data centers," *J. Geophys. Res.*, vol. 117, no. D18, p. D18111, 2012, doi: [10.1029/2012JD017665](#).
- [88] T. Schmidt, H. Schoon, H. Dobsław, K. Matthes, M. Thomas, and J. Wickert, "UTLS temperature validation of MPI-ESM decadal hindcast experiments with GPS radio occultations," *Meteorol. Zeitschrift*, vol. 25, no. 6, pp. 673–683, doi: [10.1127/metz/2015/0601](#).
- [89] C. S. Ruf et al., "The CYGNSS nanosatellite constellation hurricane mission," in *Proc. Int. Geosci. Remote Sens. Symp.*, Munich, Germany, Jul. 2012, pp. 214–216, doi: [10.1109/IGARSS.2012.6351600](#).
- [90] G. Foti et al., "Spaceborne GNSS reflectometry for ocean winds: First results from the UK TechDemoSat-1 mission," *Geophys. Res. Lett.*, vol. 42, no. 13, pp. 5435–5441, 2015. [Online]. Available: <http://dx.doi.org/10.1002/2015GL064204>
- [91] M. Unwin, P. Jales, J. Tye, C. Gommenginger, G. Foti, and J. Rosello, "Spaceborne GNSS-reflectometry on TechDemoSat-1: Early mission operations and exploitation," *IEEE J. Sel. Topics Appl. Earth Observ. Remote Sens.*, vol. 9, no. 10, pp. 4525–4539, Oct. 2016, doi: [10.1109/JSTARS.2016.2603846](#).
- [92] J. L. Garrison and S. J. Katzberg, "The application of reflected GPS signals to ocean remote sensing," *Remote Sens. Environ.*, vol. 73, no. 2, pp. 175–187, 2000.
- [93] V. U. Zavorotny and A. G. Voronovich, "Scattering of GPS signals from the ocean with wind remote sensing application," *IEEE Trans. Geosci. Remote Sens.*, vol. 38, no. 2, pp. 951–964, Mar. 2000.
- [94] G. A. Hajj and C. Zuffada, "Theoretical description of a bistatic system for ocean altimetry using the GPS signal," *Radio Sci.*, vol. 38, no. 5, p. 1089, 2003.
- [95] S. Gleason et al., "Detection and Processing of bistatically reflected GPS signals from low Earth orbit for the purpose of ocean remote sensing," *IEEE Trans. Geosci. Remote Sens.*, vol. 43, no. 6, pp. 1229–1241, Jun. 2005.
- [96] Camps, A., "Optimization and performance analysis of interferometric GNSS-R altimeters: Application to the PARIS IoD mission," *IEEE J. Sel. Topics Appl. Earth Observ. Remote Sens.*, vol. 7, no. 5, pp. 1436–1451, May 2014, doi: [10.1109/JSTARS.2014.2320873](#).
- [97] A. Camps et al., "Sensitivity of GNSS-R spaceborne observations to soil moisture and vegetation," *IEEE J. Sel. Topics Appl. Earth Observ. Remote Sens.*, vol. 9, no. 10, pp. 4730–4742, Oct. 2016, doi: [10.1109/JSTARS.2016.2588467](#).
- [98] A. M. Semmling et al., "A zeppelin experiment to study airborne altimetry using specular global navigation satellite system reflections," *Radio Sci.*, vol. 48, no. 4, pp. 427–440, 2013, doi: [10.1002/rds.20049](#).
- [99] C. Ruf et al., "CYGNSS: Enabling the future of hurricane prediction," *IEEE Geosci. Remote Sens. Mag.*, vol. 1, no. 2, pp. 52–67, Jun. 2013, doi: [10.1109/MGRS.2013.2260911](#).
- [100] A. Camps, D. Pascual, H. Park, and F. Martín, "PARIS IoD: ID-16A contribution to performance and error budgets report," ESA, Paris, France, Tech. Rep. AO/1-6576/2010/F/WE-ID, Nov. 2012.
- [101] S. D'Addio and M. Martín-Neira, "Comparison of processing techniques for remote sensing of earth-exploiting reflected radio-navigation signals," *Electron. Lett.*, vol. 49, no. 4, pp. 292–293, Feb. 2013.
- [102] E. Cardellach et al., "Consolidating the precision of interferometric GNSS-R ocean altimetry using airborne experimental data," *IEEE Trans. Geosci. Remote Sens.*, vol. 52, no. 8, pp. 4992–5004, Aug. 2014, doi: [10.1109/TGRS.2013.2286257](#).
- [103] F. Martín, A. Camps, H. Park, S. DaAddio, M. Martín-Neira, and D. Pascual, "Cross-correlation waveform analysis for conventional and interferometric GNSS-R approaches," *IEEE J. Sel. Topics Appl. Earth Observ. Remote Sens.*, vol. 7, no. 5, pp. 1560–1572, May 2014, doi: [10.1109/JSTARS.2014.2300232](#).
- [104] F. Martín, S. D'Addio, A. Camps, and M. Martín-Neira, "Modeling and analysis of GNSS-R waveforms sample-to-sample correlation," *IEEE J. Sel. Topics Appl. Earth Observ. Remote Sens.*, vol. 7, no. 5, pp. 1545–1559, May 2014, doi: [10.1109/JSTARS.2014.2308982](#).
- [105] W. Li, A. Rius, F. Fabra, E. Cardellach, S. Ribó, and M. Martín-Neira, "Revisiting the GNSS-R waveform statistics and its impact on altimetric retrievals," *IEEE Trans. Geosci. Remote Sens.*, to be published, doi: [10.1109/TGRS.2017.2785343](#).
- [106] M. Martín-Neira, W. Li, A. Andrés-Bevide, and X. Ballesteros-Sels, "'Cookie': A satellite concept for GNSS remote sensing constellations," *IEEE J. Sel. Topics Appl. Earth Observ. Remote Sens.*, vol. 9, no. 10, pp. 4593–4610, Oct. 2016, doi: [10.1109/JSTARS.2016.2585620](#).
- [107] E. R. De Roo and F. T. Ulaby, "Bistatic specular scattering from rough dielectric surfaces," *IEEE Trans. Antennas Propag.*, vol. 42, no. 2, pp. 220–231, Feb. 1994.
- [108] A. Alonso-Arroyo, A. Camps, H. Park, D. Pascual, R. Onrubia, and F. Martín, "Retrieval of significant wave height and mean sea surface level using the GNSS-R interference pattern technique: Results from a three-month field campaign," *IEEE Trans. Geosci. Remote Sens.*, vol. 53, no. 6, pp. 3198–3209, Jun. 2015.
- [109] H. Carreno-Luengo and A. Camps, "Unified GNSS-R formulation including coherent and incoherent scattering components," in *Proc. IEEE Int. Geosci. Remote Sens. Symp. (IGARSS)*, Beijing, China, Jul. 2016, pp. 4815–4818, doi: [10.1109/IGARSS.2016.7730256](#).
- [110] H. Carreno-Luengo and A. Camps, "First dual-band multiconstellation GNSS-R scatterometry experiment over boreal forests from a stratospheric balloon," *IEEE J. Sel. Topics Appl. Earth Observ. Remote Sens.*, vol. 9, no. 10, pp. 4743–4751, Oct. 2016, doi: [10.1109/JSTARS.2015.2496661](#).
- [111] H. Carreno-Luengo, A. Camps, J. Querol, and G. Forte, "First results of a GNSS-R experiment from a stratospheric balloon over boreal forests," *IEEE Trans. Geosci. Remote Sens.*, vol. 54, no. 5, pp. 2652–2663, May 2016, doi: [10.1109/TGRS.2015.2504242](#).
- [112] S. T. Lowe, C. Zuffada, Y. Chao, P. Kroger, L. E. Young, and J. L. LaBrecque, "5-cm-precision aircraft ocean altimetry using GPS reflections," *Geophys. Res. Lett.*, vol. 29, no. 10, pp. 13–13–4, 2002, doi: [10.1029/2002GL014759](#).
- [113] G. Ruffini, F. Soulat, M. Caparrini, O. Germain, and M. Martín-Neira, "The eddy experiment: Accurate GNSS-R ocean altimetry from low altitude aircraft," *Geophys. Res. Lett.*, vol. 31, p. L12306, Jun. 2004, doi: [10.1029/2004GL019994](#).
- [114] A. Rius, E. Cardellach, and M. Martín-Neira, "Altimetric analysis of the sea-surface GPS-reflected signals," *IEEE Trans. Geosci. Remote Sens.*, vol. 48, no. 4, pp. 2119–2127, Apr. 2010, doi: [10.1109/TGRS.2009.2036721](#).
- [115] A. Rius et al., "Altimetry with GNSS-R interferometry: first proof of concept experiment," *GPS Solutions*, vol. 16, no. 2, pp. 231–241, 2012, doi: [10.1007/s10291-011-0225-9](#).
- [116] H. Carreno-Luengo, A. Camps, I. Ramos-Perez, G. Forte, R. Onrubia, and R. Diez, "'Cat-2: A P(Y) and C/A GNSS-R experimental nano-satellite mission," in *Proc. IEEE Int. Geosci. Remote Sens. Symp. (IGARSS)*, Jul. 2013, pp. 843–846.
- [117] S. V. Nghiem et al., "Wetland monitoring with global navigation satellite system reflectometry," *Earth Space Sci.*, vol. 4, no. 1, pp. 16–39, doi: [10.1002/2016EA000194](#).
- [118] M. P. Clarizia, C. Ruf, P. Cipollini, and C. Zuffada, "First spaceborne observation of sea surface height using GPS-reflectometry," *Geophys. Res. Lett.*, vol. 43, no. 2, pp. 767–774, 2016.
- [119] IEEC, *SPiR Report on Flight December 3rd 2015, Final Report on ESA PIT-POC-CCN4*, document Ref. PIT-POC-CCN4-FR2, 2016.
- [120] C. Zuffada et al., *The Rise of GNSS Reflectometry for Earth Remote Sensing*. Accessed: Oct. 11 2017. [Online]. Available: https://www.researchgate.net/publication/308819024_The_rise_of_GNSS_reflectometry_for_Earth_remote_sensing
- [121] G. Beyerle and K. Hocke, "Observation and simulation of direct and reflected GPS signals in radio occultation experiments," *Geophys. Res. Lett.*, vol. 28, no. 9, pp. 1895–1898, 2001.
- [122] G. Beyerle, K. Hocke, J. Wickert, T. Schmidt, C. Marquardt, and C. Reigber, "GPS radio occultations with CHAMP: A radio holographic analysis of GPS signal propagation in the troposphere and surface reflections," *J. Geophys. Res.*, vol. 107, no. D24, pp. ACL27-1–ACL27-14, 2002, doi: [10.1029/2001JD001402](#).
- [123] *GNSS-R Assessment of Requirements and Consolidation of Retrieval Algorithms, Final Project Report*, document ESA-AO1-7850/14-GARCA-FR, GARCA Team, 2016, p. 463.
- [124] A. M. Semmling, V. Leister, J. Saynisch, F. Zus, S. Heise, and J. Wickert, "A phase-altimetric simulator: Studying the sensitivity of earth-reflected GNSS signals to ocean topography," *IEEE Trans. Geosci. Remote Sens.*, vol. 54, no. 11, pp. 6791–6802, Nov. 2016, doi: [10.1109/TGRS.2016.25910652016](#).
- [125] A. M. Semmling et al., "On the retrieval of the specular reflection in GNSS carrier observations for Ocean altimetry," *Radio Sci.*, vol. 47, no. 6, pp. 1–13, 2012, doi: [10.1029/2012RS005007](#).
- [126] A. M. Semmling et al., "A zeppelin experiment to study airborne altimetry using specular Global Navigation Satellite System reflections," *Radio Sci.*, vol. 48, no. 4, pp. 427–440, 2013, doi: [10.1002/rds.20049](#).

- [127] G. Liebsch, U. Schirmer, J. Ihde, H. Denker, and J. Müller, *Quasigeoidbestimmung für Deutschland*, vol. 49. DVW-Schriftenreihe, 2006, pp. 127–146. [Online]. Available: <https://www.dvw.de/rubrik/publikationen-schriftenreihe/144>
- [128] A. M. Semmling et al., “Detection of Arctic Ocean tides using interferometric GNSS-R signals,” *Geophys. Res. Lett.*, vol. 38, no. 4, p. L04103, 2011, doi: [10.1029/2010GL046005](https://doi.org/10.1029/2010GL046005).
- [129] J. L. Garrison, A. Komjathy, V. U. Zavorotny, and S. J. Katzberg, “Wind speed measurement using forward scattered GPS signals,” *IEEE Trans. Geosci. Remote Sens.*, vol. 40, no. 1, pp. 50–65, Jan. 2002.
- [130] A. Komjathy, M. Armatys, D. Masters, P. Axelrad, V. Zavorotny, and S. Katzberg, “Retrieval of ocean surface wind speed and wind direction using reflected GPS signals,” *J. Atmos. Ocean. Technol.*, vol. 21, no. 3, pp. 515–526, Mar. 2004.
- [131] A. Rius, J. M. Aparicio, E. Cardellach, M. Martín-Neira, and B. Chapron, “Sea surface state measured using GPS reflected signals,” *Geophys. Res. Lett.*, vol. 29, pp. 37-1–37-4, Dec. 2002.
- [132] E. Cardellach, G. Ruffini, D. Pino, A. Rius, A. Komjathy, and J. L. Garrison, “Mediterranean balloon experiment: Ocean wind speed sensing from the stratosphere, using GPS reflections,” *Remote Sens. Environ.*, vol. 88, no. 3, pp. 351–362, Dec. 2003, doi: [10.1016/S0034-4257\(03\)00176-7](https://doi.org/10.1016/S0034-4257(03)00176-7).
- [133] O. Germain, G. Ruffini, F. Soulat, M. Caparrini, B. Chapron, and P. Silvestrin, “The eddy experiment: GNSS-R speculometry for directional sea-roughness retrieval from low altitude aircraft,” *Geophys. Res. Lett.*, vol. 31, p. L21307, Nov. 2004, doi: [10.1029/2004GL020991](https://doi.org/10.1029/2004GL020991).
- [134] T. Elfouhaily, D. R. Thompson, and L. Linstrom, “Delay-Doppler analysis of bistatically reflected signals from the ocean surface: Theory and application,” *IEEE Trans. Geosci. Remote Sens.*, vol. 40, no. 3, pp. 560–573, Mar. 2002, doi: [10.1109/TGRS.2002.1000316](https://doi.org/10.1109/TGRS.2002.1000316).
- [135] O. Nogués-Correig, E. C. Gali, J. S. Campderros, and A. Rius, “A GPS-reflections receiver that computes Doppler/delay maps in real time,” *IEEE Trans. Geosci. Remote Sens.*, vol. 45, no. 1, pp. 156–174, Jan. 2007.
- [136] E. Cardellach and A. Rius, “A new technique to sense non-Gaussian features of the sea surface from L-band bi-static GNSS reflections,” *Remote Sens. Environ.*, vol. 112, no. 6, pp. 2927–2937, 2008, doi: [10.1016/j.rse.2008.02.003](https://doi.org/10.1016/j.rse.2008.02.003).
- [137] E. Valencia et al., “On the use of GNSS-R data to correct L-band brightness temperatures for sea-state effects: Results of the ALBATROSS field experiments,” *IEEE Trans. Geosci. Remote Sens.*, vol. 49, no. 9, pp. 3225–3235, Sep. 2011.
- [138] P. Høeg and A. Carlström, “Information content in reflected global navigation satellite system signals,” in *Proc. 2nd Int. Conf. Wireless Commun., Veh. Technol., Inf. Theory Aerosp. Electron. Syst. Technol. (Wireless VITAE)*, Chennai, India, Feb./Mar. 2011, pp. 1–5, doi: [10.1109/WIRELESSVITAE.2011.5940894](https://doi.org/10.1109/WIRELESSVITAE.2011.5940894).
- [139] N. Rodriguez-Alvarez, D. M. Akos, V. U. Zavorotny, J. A. Smith, A. Camps, and C. W. Fairall, “Airborne GNSS-R wind retrievals using delay-Doppler maps,” *IEEE Trans. Geosci. Remote Sens.*, vol. 51, no. 1, pp. 626–641, Jan. 2013, doi: [10.1109/TGRS.2012.2196437](https://doi.org/10.1109/TGRS.2012.2196437).
- [140] E. Valencia, V. U. Zavorotny, D. M. Akos, and A. Camps, “Using DDM asymmetry metrics for wind direction retrieval from GPS ocean-scattered signals in airborne experiments,” *IEEE Trans. Geosci. Remote Sens.*, vol. 52, no. 7, pp. 3924–3936, Jul. 2014.
- [141] S. Soisuvann, Z. Jelenak, F. Saïd, P. S. Chang, and A. Egido, “The GNSS reflectometry response to the ocean surface winds and waves,” *IEEE J. Sel. Topics Appl. Earth Observ. Remote Sens.*, vol. 9, no. 10, pp. 4678–4699, Oct. 2016, doi: [10.1109/JSTARS.2016.2602703](https://doi.org/10.1109/JSTARS.2016.2602703).
- [142] F. Saïd, S. Soisuvann, Z. Jelenak, and P. S. Chang, “Performance assessment of simulated CYGNSS measurements in the tropical cyclone environment,” *IEEE J. Sel. Topics Appl. Earth Observ. Remote Sens.*, vol. 9, no. 10, pp. 4709–4719, Oct. 2016, doi: [10.1109/JSTARS.2016.2559782](https://doi.org/10.1109/JSTARS.2016.2559782).
- [143] J. Tye, P. Jales, M. Unwin, and C. Underwood, “The first application of stare processing to retrieve mean square slope using the SGR-ReSI GNSS-R experiment on TDS-1,” *IEEE J. Sel. Topics Appl. Earth Observ. Remote Sens.*, vol. 9, no. 10, pp. 4669–4677, Oct. 2016, doi: [10.1109/JSTARS.2016.2542348](https://doi.org/10.1109/JSTARS.2016.2542348).
- [144] D. Schiavulli, F. Nunziata, M. Migliaccio, F. Frappart, G. Ramilien, and J. Darrozes, “Reconstruction of the radar image from actual DDMs collected by TechDemoSat-1 GNSS-R mission,” *IEEE J. Sel. Topics Appl. Earth Observ. Remote Sens.*, vol. 9, no. 10, pp. 4700–4708, Oct. 2016.
- [145] N. Pierdicca, L. Guerriero, R. Giusto, M. Brogioni, and A. Egido, “SAVERS: A simulator of GNSS reflections from bare and vegetated soils,” *IEEE Trans. Geosci. Remote Sens.*, vol. 52, no. 10, pp. 6542–6554, Oct. 2014, doi: [10.1109/TGRS.2013.2297572](https://doi.org/10.1109/TGRS.2013.2297572).
- [146] J. C. Falkingham, (Mar. 2014). Global Satellite Observation Requirements for Floating Ice. Focusing on Synthetic Aperture Radar. WMO Polar Space Task Group. [Online]. Available: https://www.wmo.int/pages/prog/sat/pstg_en.php
- [147] F. T. Ulaby, R. K. Moore, and A. K. Fung, *Microwave Remote Sensing: Active and Passive*, vol. 2. Reading, MA, USA: Addison-Wesley, 1986.
- [148] A. M. Semmling, A. Rösel, M. Ludwig, M. Bratrein, S. Gerland, and J. Wickert, *A Fram Strait Experiment: Sensing Sea Ice Conditions Using Shipborne GNSS Reflectometry*, vol. 19, document EGU2017-13287, Geophysical Research Abstracts, EGU General Assembly, 2017. [Online]. Available: <http://meetingorganizer.copernicus.org/EGU2017/EGU2017-13287.pdf>
- [149] J. Wickert et al., “GPS radio occultation: Results from CHAMP, GRACE and FORMOSAT-3/COSMIC,” *Terrestrial Atmos. Ocean. Sci.*, vol. 20, pp. 35–50, Feb. 2009, doi: [10.3319/TAO.2007.12.26.01\(F3C\)](https://doi.org/10.3319/TAO.2007.12.26.01(F3C)).
- [150] J. Wickert et al., “Atmosphere sounding by GPS radio occultation: First results from CHAMP,” *Geophys. Res. Lett.*, vol. 28, no. 17, pp. 3263–3266, 2001.
- [151] J. Wickert et al., “GPS radio occultation with CHAMP and GRACE: A first look at a new and promising satellite configuration for global atmospheric sounding,” *Ann. Geophys.*, vol. 23, no. 3, pp. 653–658, 2005, doi: [10.5194/angeo-23-653-2005](https://doi.org/10.5194/angeo-23-653-2005).
- [152] R. A. Anthes, C. Rocken, and Y.-H. Kuo, “Applications of COSMIC to meteorology and climate,” *Terrestrial Atmos. Ocean. Sci.*, vol. 11, no. 1, pp. 115–156, 2000.
- [153] R. A. Anthes et al., “The COSMIC/FORMOSAT-3 mission: Early results,” *Bull. Amer. Meteorol. Soc.*, vol. 89, pp. 313–333, Mar. 2008, doi: [10.1175/BAMS-89-3-313](https://doi.org/10.1175/BAMS-89-3-313).
- [154] S. B. Healy and J.-N. Thépaut, “Assimilation experiments with CHAMP GPS radio occultation measurements,” *Quart. J. Roy. Meteorol. Soc.*, vol. 132, no. 615, pp. 605–623, 2006.
- [155] J. M. Aparicio and G. Deblonde, “Impact of the assimilation of CHAMP refractivity profiles on environment Canada global forecasts,” *Monthly Weather Rev.*, vol. 136, pp. 257–275, Jan. 2008.
- [156] P. Poli, S. B. Healy, F. Rabier, and J. Pailleux, “Preliminary assessment of the scalability of GPS radio occultations impact in numerical weather prediction,” *Geophys. Res. Lett.*, vol. 35, no. 23, p. L23811, 2008, doi: [10.1029/2008GL035873](https://doi.org/10.1029/2008GL035873).
- [157] L. Cucurull, “Improvement in the use of an operational constellation of GPS radio occultation receivers in weather forecasting,” *Weather Forecast.*, vol. 25, pp. 749–767, Apr. 2010.
- [158] M. P. Rennie, “The impact of GPS radio occultation assimilation at the Met Office,” *Quart. J. Roy. Meteorol. Soc.*, vol. 136, no. 646, pp. 116–131, 2010.
- [159] P. Bauer, G. Radnóti, S. Healy, and C. Cardinali, “GNSS radio occultation constellation observing system experiments,” *Monthly Weather Rev.*, vol. 142, no. 2, pp. 555–572, 2014, doi: [10.1175/MWR-D-13-00130.1](https://doi.org/10.1175/MWR-D-13-00130.1).
- [160] C. Cardinali, “Monitoring the observation impact on the short-range forecast,” *Quart. J. Roy. Meteorol. Soc.*, vol. 135, no. 648, pp. 239–250, 2009, doi: [10.1002/qj.366](https://doi.org/10.1002/qj.366).
- [161] P. Poli, S. B. Healy, and D. P. Dee, “Assimilation of global positioning system radio occultation data in the ECMWF ERA-Interim reanalysis,” *Quart. J. Roy. Meteorol. Soc.*, vol. 136, no. 653, pp. 1972–1990, 2010, doi: [10.1002/qj.722](https://doi.org/10.1002/qj.722).
- [162] A. J. Simmons et al., “Estimating low-frequency variability and trends in atmospheric temperature using ERA-Interim,” *Quart. J. Roy. Meteorol. Soc.*, vol. 140, no. 679, pp. 329–353, 2014, doi: [10.1002/qj.2317](https://doi.org/10.1002/qj.2317).
- [163] F. Harnisch, S. B. Healy, P. Bauer, and S. J. English, “Scaling of GNSS radio occultation impact with observation number using an ensemble of data assimilations,” *Monthly Weather Rev.*, vol. 141, pp. 4395–4413, Dec. 2013. [Online]. Available: <http://dx.doi.org/10.1175/MWR-D-13-00098.1>
- [164] B. C. Lackner, A. K. Steiner, G. C. Hegerl, and G. Kirchengast, “Atmospheric climate change detection by radio occultation data using a fingerprinting method,” *J. Clim.*, vol. 24, pp. 5275–5291, Oct. 2011, doi: [10.1175/2011JCLI3966.1](https://doi.org/10.1175/2011JCLI3966.1).
- [165] A. K. Steiner, G. Kirchengast, B. C. Lackner, B. Pirscher, M. Borsche, and U. Foelsche, “Atmospheric temperature change detection with GPS radio occultation 1995 to 2008,” *Geophys. Res. Lett.*, vol. 36, no. 18, p. L18702, 2009, doi: [10.1029/2009GL039777](https://doi.org/10.1029/2009GL039777).

- [166] A. von Engeln, J. Teixeira, J. Wickert, and S. A. Buehler, "Using CHAMP radio occultation data to determine the top altitude of the planetary boundary layer," *Geophys. Res. Lett.*, vol. 32, no. 6, p. L06815, 2005, doi: [10.1029/2004GL022168](https://doi.org/10.1029/2004GL022168).
- [167] T. Schmidt, J. Wickert, and A. Haser, "Variability of the upper troposphere and lower stratosphere observed with GPS radio occultation bending angles and temperatures," *Adv. Space Res.*, vol. 46, no. 2, pp. 150–161, 2010, doi: [10.1016/j.asr.2010.01.021](https://doi.org/10.1016/j.asr.2010.01.021).
- [168] T. Schmidt, J. Wickert, G. Beyerle, and S. Heise, "Global tropopause height trends estimated from GPS radio occultation data," *Geophys. Res. Lett.*, vol. 35, no. 11, p. L11806, 2008, doi: [10.1029/2008GL034012](https://doi.org/10.1029/2008GL034012).
- [169] T. Rieckh, B. Scherllin-Pirscher, F. Ladstädter, and U. Foelsche, "Characteristics of tropopause parameters as observed with GPS radio occultation," *Atmos. Meas. Techn.*, vol. 7, pp. 3947–3958, Nov. 2014, doi: [10.5194/amt-7-3947-2014](https://doi.org/10.5194/amt-7-3947-2014).
- [170] B. Scherllin-Pirscher, A. K. Steiner, and G. Kirchengast, "Deriving dynamics from GPS radio occultation: Three-dimensional wind fields for monitoring trends estimated from GPS radio occultation data," *Geophys. Res. Lett.*, vol. 41, pp. 7367–7374, Oct. 2014, doi: [10.1002/2014GL061524](https://doi.org/10.1002/2014GL061524).
- [171] T. Schmidt, S. Heise, J. Wickert, G. Beyerle, and C. Reigber, "GPS radio occultation with CHAMP and SAC-C: Global monitoring of thermal tropopause parameters," *Atmos. Chem. Phys.*, vol. 5, pp. 1473–1488, 2005, doi: [10.5194/acp-5-1473-2005](https://doi.org/10.5194/acp-5-1473-2005).
- [172] S. P. Alexander, A. R. Klekociuk, and T. Tsuda, "Gravity wave and orographic wave activity observed around the Antarctic and Arctic stratospheric vortices by the COSMIC GPS-RO satellite constellation," *J. Geophys. Res.*, vol. 114, p. D17103, Sep. 2009, doi: [10.1029/2009JD011851](https://doi.org/10.1029/2009JD011851).
- [173] T. Tsuda, "Characteristics of atmospheric gravity waves observed using the MU (Middle and Upper atmosphere) radar and GPS (Global Positioning System) radio occultation," *Proc. Jpn. Acad. B-Phys.*, vol. 90, no. 1, pp. 12–27, 2014.
- [174] R. A. Anthes, "Exploring Earth's atmosphere with radio occultation: Contributions to weather, climate and space weather," *Atmos. Meas. Techn.*, vol. 4, no. 6, pp. 1077–1103, 2011, doi: [10.5194/amt-4-1077-2011](https://doi.org/10.5194/amt-4-1077-2011).
- [175] G. A. Hajj and L. J. Romans, "Ionospheric electron density profiles obtained with the Global Positioning System: Results from the GPS/MET experiment," *Radio Sci.*, vol. 33, no. 1, pp. 175–190, 1998.
- [176] A. Rius, G. Ruffini, and A. Romeo, "Analysis of ionospheric electron density distribution from GPS/MET occultations," *IEEE Trans. Geosci. Remote Sens.*, vol. 36, no. 2, pp. 383–394, Mar. 1998.
- [177] G. Ruffini, E. Cardellach, A. Flores, L. Cucurull, and A. Rius, "Ionospheric calibration of radar altimeters using GPS tomography," *Geophys. Res. Lett.*, vol. 25, no. 20, pp. 3771–3774, 1998.
- [178] M. Hernández-Pajares, J. M. Juan, J. Sanz, and J. G. Solé, "Global observation of the ionospheric electronic response to solar events using ground and LEO GPS data," *J. Geophys. Res., Space Phys.*, vol. 103, no. A9, pp. 20789–20796, 1998.
- [179] W. S. Schreiner, S. V. Sokolovskiy, C. Rocken, and D. C. Hunt, "Analysis and validation of GPS/MET radio occultation data in the ionosphere," *Radio Sci.*, vol. 34, no. 4, pp. 949–966, 1999.
- [180] M. Hernández-Pajares, J. M. Juan, and J. Sanz, "Improving the Abel inversion by adding ground GPS data to LEO radio occultations in ionospheric sounding," *Geophys. Res. Lett.*, vol. 27, no. 16, pp. 2473–2476, 2000.
- [181] N. Jakowski et al., "GPS radio occultation measurements of the ionosphere from CHAMP: Early results," *Geophys. Res. Lett.*, vol. 29, no. 10, pp. 95–1–95–4, 2002.
- [182] M. Garcia-Fernandez, M. Hernandez-Pajares, J. M. Juan, and J. Sanz, "Performance of the improved Abel transform to estimate electron density profiles from GPS occultation data," *GPS Solutions*, vol. 9, no. 2, pp. 105–110, 2005.
- [183] A. J. Mannucci, C. O. Ao, X. Pi, and B. A. Iijima, "The impact of large scale ionospheric structure on radio occultation retrievals," *Atmos. Meas. Techn.*, vol. 4, no. 12, pp. 2837–2850, 2011.
- [184] C. Arras, J. Wickert, G. Beyerle, S. Heise, T. Schmidt, and C. Jacobi, "A global climatology of ionospheric irregularities derived from GPS radio occultation," *Geophys. Res. Lett.*, vol. 35, no. 14, p. L14809, 2008, doi: [10.1029/2008GL034158](https://doi.org/10.1029/2008GL034158).
- [185] N. Jakowski, S. Heise, S. M. Stankov, and K. Tsybulia, "Remote sensing of the ionosphere by space-based GNSS observations," *Adv. Space Res.*, vol. 38, no. 11, pp. 2337–2343, 2006.
- [186] N. Jakowski, V. Wilken, and C. Mayer, "Space weather monitoring by GPS measurements on board CHAMP," *Space Weather*, vol. 5, no. 8, pp. 1–13, 2007, doi: [10.1029/2006SW000271](https://doi.org/10.1029/2006SW000271).
- [187] N. Jakowski, J. Mielich, M. Hoque, and M. Danielides, "Equivalent slab thickness at the mid-latitude ionosphere during solar cycle 23," in *Proc. 38th COSPAR Sci. Assembly*, Bremen, Germany, Jul. 2010.
- [188] G. Olivares-Pulido, M. Hernández-Pajares, A. Aragón-Angel, and A. Garcia-Rigo, "A linear scale height Chapman model supported by GNSS occultation measurements," *J. Geophys. Res. Space Phys.*, vol. 121, no. 8, pp. 7932–7940, 2016, doi: [10.1002/2016JA022337](https://doi.org/10.1002/2016JA022337).
- [189] J. Danzer, S. B. Healy, and I. D. Culverwell, "A simulation study with a new residual ionospheric error model for GPS radio occultation climatologies," *Atmos. Meas. Techn.*, vol. 8, no. 8, pp. 3395–3404, 2015.
- [190] A. Jäggi, U. Hugentobler, H. Bock, and G. Beutler, "Precise orbit determination for GRACE using undifferenced or doubly differenced GPS data," *Adv. Space Res.*, vol. 39, no. 10, pp. 1612–1619, 2007, doi: [10.1016/j.asr.2007.03.012](https://doi.org/10.1016/j.asr.2007.03.012).
- [191] H. Bock, A. Jäggi, G. Beutler, and U. Meyer, "GOCE: Precise orbit determination for the entire mission," *J. Geodesy*, vol. 88, no. 11, pp. 1047–1060, 2014, doi: [10.1007/s00190-014-0742-8](https://doi.org/10.1007/s00190-014-0742-8).
- [192] C. Flohrer, M. Otten, T. Springer, and J. Dow, "Generating precise and homogeneous orbits for Jason-1 and Jason-2," *Adv. Space Res.*, vol. 48, no. 1, pp. 152–172, 2011, doi: [10.1016/j.asr.2011.02.017](https://doi.org/10.1016/j.asr.2011.02.017).
- [193] H. Peter et al., "Sentinel-1A—First precise orbit determination results," *Adv. Space Res.*, vol. 60, no. 5, pp. 879–892, 2017, doi: [10.1016/j.asr.2017.05.034](https://doi.org/10.1016/j.asr.2017.05.034).
- [194] S. Hackel, O. Montenbruck, P. Steigenberger, U. Balss, C. Gisinger, and M. Eineder, "Model improvements and validation of TerraSAR-X precise orbit determination," *J. Geodesy*, vol. 91, no. 5, pp. 547–562, 2017, doi: [10.1007/s00190-016-0982-x](https://doi.org/10.1007/s00190-016-0982-x).
- [195] A. Jäggi, R. Dach, O. Montenbruck, U. Hugentobler, H. Bock, and G. Beutler, "Phase center modeling for LEO GPS receiver antennas and its impact on precise orbit determination," *J. Geodesy*, vol. 83, no. 12, pp. 1145–1162, 2009, doi: [10.1007/s00190-009-0333-2](https://doi.org/10.1007/s00190-009-0333-2).
- [196] F. Fabra, E. Cardellach, W. Li, and A. Rius, (May 2017). *WAVPY: An Open-Source Tool for the GNSS+R Community*. GNSS+R, Ann Arbor, MI, USA. [Online]. Available: http://www.gnssr2017.org/images/Poster_session/GNSS+R2017_Poster_TMS_2_Fabra_Wavpy.pdf and https://www.ice.csic.es/research/gold_rtr_mining/posters/posterWavpy_GNSS+R17.pdf
- [197] F. Fabra. (Jul. 2017). *Wavpy v1.0: User Manual*. ICE-CSIC/IEEC. [Online]. Available: https://www.ice.csic.es/research/gold_rtr_mining/manuals/wavpy_v1.0_User_manual.pdf
- [198] S. D'Addio, "Advanced GNSS-R processing techniques for ocean altimetry," Ph.D. dissertation, Università degli Studi del Sannio, Benevento, Italy, 2017.
- [199] *Improved Modelling of Short and Long Term Characteristics of Ionospheric Disturbances During Active Years of the Solar Cycle*, document ESA Contract 4000115300/15/NL/A, SCIONAV, 2016.
- [200] A. Camps, H. Park, G. Foti, and C. Gommenginger, "Ionospheric effects in GNSS-reflectometry from space," *IEEE J. Sel. Topics Appl. Earth Observ. Remote Sens.*, vol. 9, no. 12, pp. 5851–5861, 2016, doi: [10.1109/JSTARS.2016.2612542](https://doi.org/10.1109/JSTARS.2016.2612542).
- [201] A. Camps, H. Park, E. Lancheros, R. Onrubia, D. Pascual, and J. Querol, "Ionospheric scintillation impact on GNSS-R altimetry," GNSS+R, Ann Arbor, MI, USA, Tech. Rep., Mar. 2018. [Online]. Available: http://www.gnssr2017.org/images/Wednesday_morning/GNSS+R2017_WE_AM_3_Camps_Ionosphere_altimetry.pdf
- [202] K. M. Hiremath, "Prediction of solar cycle 24 and beyond," *Astrophys. Space Sci.*, vol. 314, nos. 1–3, pp. 45–49, 2008, doi: [10.1007/s10509-007-9728-9](https://doi.org/10.1007/s10509-007-9728-9).
- [203] C. Chew, C. Zuffada, R. Shah, and A. Mannucci, "Mapping sea ice using reflected GNSS signals in a bistatic radar system," EGU General Assembly, Vienna, Austria, Tech. Rep. EPSC2016-10574, 2016.
- [204] A. Dielacher and H. Fragner, *PARIS Correlator Final Report*, document Contract P-11281-RP-0006-RSA, Jan. 2015.



ESTEL CARDELLACH (M'10) received the Ph.D. degree in physics from the Polytechnic University of Catalonia, Barcelona, Spain, in 2002. She has been involved in scientific applications of global navigation satellite systems (GNSS) for remote sensing of the Earth, such as extraction of geophysical information of the GNSS reflected signals, radio occultation, and geodetic techniques. She held a post-doctoral position at NASA/Jet Propulsion Laboratory, Pasadena, CA, USA, from 2002 to 2003, and a post-doctoral research position at the Harvard Smithsonian Center for Astrophysics, Cambridge, MA, USA, from 2003 to 2005. Since 2005, she has been with the Institute of Space Sciences (ICE-CSIC/IEEC). She is the Principal Investigator of the space-borne experiment radio-occultation and heavy precipitation aboard the PAZ low earth orbiter. She was a recipient of the National Research Council Award.



JENS WICKERT received the Graduate degree in physics from the Technical University Dresden, Dresden, Germany, in 1989, and the Ph.D. degree in geophysics/meteorology from the Karl-Franzens-University Graz, Austria, in 2002. He was with several German geoscience research institutes. He currently holds a joint professorship of GFZ with the Technical University of Berlin on global navigation satellite systems (GNSS) remote sensing, navigation and positioning. He is also the Deputy GFZ Section Head Space Geodetic Techniques and the GFZ Speaker of the Atmosphere and Climate Research Programme of the German Helmholtz Association. He has authored/co-authored over 160 ISI listed publications on GNSS Earth observation. He was a Principal Investigator of the pioneering GPS radio occultation experiment aboard the German CHAMP satellite and was coordinating the GEROSS-ISS proposal to ESA. He is the Chair of the Science Advisory Group of the GEROSS-ISS mission.

RENS BAGGEN was born in Geleen, The Netherlands. He received the M.Sc. degree from the Technical University of Eindhoven in 1992, with a focus on antennas and propagation. He was involved in the fields of avionics and quality management with the Dutch Aerospace Laboratory (NLR), Amsterdam, in 1993. In 1995, he joined the Department of Antennas and EM-Modeling, IMST, and specialised in antenna theory, simulation methods/tools, waveguide antennas, metamaterials, and measurement techniques. He was the Coordinator of the FP7-Project MEMS-4-MMIC. He has been involved in many research and development projects in FP5, FP6, and FP7 and is currently involved in H2020 projects. Phased array technology is one of his main fields of expertise. He has authored and co-authored over 50 peer-reviewed publications in conferences and journals. His current activities involve acquisition and coordination/management of long term EU and ESA projects.

JAVIER BENITO received the degree in telecommunication engineer from the Universidad Politécnica de Madrid, Madrid, Spain, in 1989. Since 1989, he has been with EADS CASA Espacio, where he is currently a part of Airbus Defence and Space, where he was involved in technological areas and departments of the company. From 1990 to 1992, he was with MATRA-Marconi, Toulouse, France, where he was involved in the integration and test campaign of the telecommunication satellite (HISPASAT 1A) and also with Kourou, (French Guiana), where he was involved in the launch campaign. He has been participating as a Project/Study Manager in multitude of ESA and Spanish projects related with space payloads and satellites MINISAT, COPLAS (communication payload for a LEO satellite), CESAR&MINISOB (observation small satellites), SMOS, SMOSops, SuperMIRAS, PARIS, or GEROSS-ISS. He is also a Project Manager of PROBA-3 Project in Airbus.



ADRIANO CAMPS (F'90) He is currently a Full Professor with the Technical University of Catalonia-BarcelonaTech, Spain. In 1999, he was on sabbatical leave at the Microwave Remote Sensing Laboratory, University of Massachusetts, Amherst. Since 1993, he has been involved in the European Space Agency SMOS Earth Explorer Mission, from the instrument and algorithmic points of view, performing field experiments. Since 2001, he has been studying the use of GNSS-R techniques to perform the sea state correction needed to retrieve salinity from L-band radiometric observations. He is currently the Co-Leader of the Remote Sensing Laboratory and the UPC NanoSat Laboratory. He is responsible of the first four UPC nano-satellites 3Cat-1, a 1U CubeSat with seven small technology demonstrators and scientific payloads, and 3Cat-2, a 6U CubeSat with the first dual-frequency dual-polarization GNSS-R payload, 3Cat-4 a 1U Cubesat with a GNSS-R Payload selected in the 2016 ESA Fly your satellite call, and 3Cat-5A/B a tandem 6U satellite mission winner of the Copernicus masters ESA Sentinel Small Satellite Challenge. He has authored over 170 papers in peer-reviewed journals and over 350 international conference presentations. He holds 10 patents and has advised 22 Ph.D. thesis students, over 130 final projects, and M.Sc. theses. His research interests are focused on in microwave remote sensing, with special emphasis in microwave radiometry by aperture synthesis techniques and remote sensing using signals of opportunity (GNSS-R). Since 2007, he has been focusing on the use of small satellites to test innovative Earth observation sensors. His publications have received over 5900 citations and his h-index is 38.



NUNO CATARINO received the degree in physics engineering from the Instituto Superior Técnico, Lisbon, Portugal, in 2000, and the Ph.D. degree in applied mathematics from the University of Warwick, Coventry, U.K., in 2004. He is currently the Head of the PDGS Division, Ground Segment Systems Business Unit, DEIMOS Engenharia, Lisboa, Portugal. He has led many projects for ESA and other clients, namely, the GNSS-R projects PARIS IOD and GEROSS-ISS Phase A studies, the GARCA scientific studies, the GEAF intelligent Ground Segment orchestrator, and the Sentinel 3 Optical Ground Processor Level 1 Prototype at DEIMOS Engenharia, Lisboa. He has also involved in the Phases 3 and 4 of the SMOS L1 Processor Prototype, including the Image Validation Campaign at ESRIN and the re-design and implementation of the image reconstruction module.

BERTRAND CHAPRON received the Ph.D. degree in fluid mechanics from Aix-Marseille II, Marseille, France, in 1988. He is currently the Head of the Space Oceanography Laboratory, Institut Français de Recherche Pour l'exploitation de la Mer, Paris, France, where he is responsible for the Centre Exploitation and Research for Satellite Data. He has broad background in the use of satellite data for ocean remote sensing and oceanography in general and participates in numerous related national and international satellite and research projects. He has authored over 100 papers in refereed journals on applied mathematics, physical oceanography, electromagnetic wave theory, and its applications to ocean remote sensing, data processing, and management.



including a GPS L2C receiver and has led the passive reflectometry projects, namely, PARIS Correlator and GEROS- ISS and the PACO for CubeSat study at RUAG Space GmbH.

ANDREAS DIELACHER received the M.Sc. degree in computer engineering from Technical University, Vienna, Austria, in 2010. He is currently pursuing the Ph.D. degree with the Austrian CubeSat Project—Passive Reflectometer and DosimeTrY, RUAG Space GmbH, Vienna. He is assigned as Project Engineer for the Passive Reflectometer payload. He is with the Projects Engineering Group, RUAG Space GmbH. He was involved in various designs,



research of the GNSS-R concept toward remote sensing of the cryosphere. He is currently with the Earth Observation Research Group, Institute of Space Sciences (ICE-CSIC/IEEC), Barcelona, where he is involved in the applications of global navigation satellite systems to Earth science.

FRAN FABRA received the M.Sc. degree in telecommunication engineering in 2007, the master's degree in information and communication technologies from the Universitat Politècnica de Catalunya, Barcelona, Spain, in 2007, and the Ph.D. degree from the Universitat Politècnica de Catalunya in 2013. His master's thesis was on security in aeronautical mobile networks at TriaGnoSys GmbH, Munich, Germany. His Ph.D. dissertation was dedicated to

GREG FLATO is currently a Senior Research Scientist with the Environment Canada's Climate Research Division, who specializes in sea ice and global Earth System modeling. He has authored over 60 peer-reviewed papers and has been involved in the development of Environment Canada's series of global and regional climate models; these models are highly regarded internationally and are used in a wide range of climate research and impact assessment studies. He is also involved in the ongoing development of Environment Canada's seasonal to interannual climate prediction system, and the development of the Canadian Climate Data and Scenarios website. He has extensive experience in the IPCC assessment process. He served as a Lead Author on the Working Group I contribution to the Fourth Assessment Report (2007) and a Coordinating Lead Author on the Fifth Assessment Report (2014). He has also served for a number of international scientific committees, including the World Climate Research Program's Joint Scientific Committee. He is currently a Co-Chair of the WCRP's Climate and Cryosphere core project.



opment of the latest space-born GNSS receiver generation of RUAG's product line.

HEINRICH FRAGNER received the Ph.D. degree in physics from the University of Vienna, in 2005, and the M.Sc. degree in computer engineering from the Technical University of Vienna, in 1997. He is currently a Project Manager with RUAG Space GmbH. In particular, he leads the projects which are covering the definition, design, development, and validation of an ASIC-based signal processing core for passive reflectometry. He is also assigned as the Project Manager for the devel-



ical Oceanography Department, Institut de Ciències del Mar, Consejo Superior de Investigaciones Científicas, Barcelona, Spain, where she has been involved in the Soil Moisture and Ocean Salinity (SMOS) mission. She is currently the Executive Director of the SMOS Barcelona Expert Centre on Remote Sensing. Her work is focused on cryospheric applications using satellite radiometry.

CAROLINA GABARRÓ received the B.Eng. degree in telecommunications engineering and the Ph.D. degree in ocean science from the Universitat Politècnica de Catalunya, Barcelona, in 1998 and 2004, respectively. From 1997 to 1999, she was with the European Space Research and Technology Centre, European Space Agency, Noordwijk, The Netherlands, where she was involved in ocean-color remote sensing (for the ENVISAT mission). Since 2000, she has been with the Phys-



Her work includes research in altimetry for sea state, along-track interferometric SAR for currents, global navigation satellite systems reflectometry for surface winds and sea state, SAR altimetry, salinity from space with SMOS, and wide-swath ocean altimetry. Her research interests include active and passive microwave remote sensing of the ocean, understanding interactions of microwave signals with the ocean surface, remote sensing of ocean wind and waves, and developing new Earth observation technologies and applications.

CHRISTINE GOMMENGINGER received the Diplôme d'Etudes Approfondies degree in electromagnetics, telecommunications, and remote sensing from the University of Toulon, La Garde, France—University of Nice Sophia Antipolis, Nice, France, and the Ph.D. degree from the University of Southampton, Southampton, U.K., with a focus on microwave radar remote sensing of the ocean at low grazing angles. She has been involved with the National Oceanography Centre for over 20 years.

CHRISTIAN HAAS received the B.Sc. degree from the Technische Universität Clausthal, in 1989, and the M.Sc. degree from the Christian Albrechts Universität zu Kiel, in 1993, and the Ph.D. degree from the Universität Bremen, in 1996. He was with the University of Alberta and York University, Canada. He is currently a Professor with the University of Bremen, and the Head of the Sea Ice Geophysics Section, Alfred Wegener Institute for Polar and Marine Research, Germany. His research interests focus on the role of Arctic and Antarctic sea ice for the climate and ecosystem and for humans, on atmosphere-ice-ocean-biology interactions, ice thickness measurements, and remote sensing.

SEAN HEALY has been involved in the applications of GNSS radio occultation (GNSS-RO) measurements since 1996, starting with the validation of GPS-MET temperature retrievals. He subsequently co-developed the first "1D-Var" retrieval codes for GNSS-RO measurements and performed early information content studies. He designed and implemented the GNSS-RO refractivity assimilation system used operationally for NWP at the Met Office until 2010 and the bending angle assimilation system used operationally at ECMWF. He was involved in assimilating GNSS-RO measurements in the ERA-interim reanalysis, climate applications of GNSS-RO measurements, the sensitivity to the empirical refractivity coefficients, and the retrieval of surface pressure information from GNSS-RO. He has contributed to numerous successful projects for ESA and EUMETSAT. He has authored/co-authored 31 journal papers in this area since 2000. He is a member of the EUMETSAT/ESA's GRAS Scientific Advisory Group. He organized the ECMWF/GRAS SAF Workshop on applications of GPS radio occultation measurements in 2008.

MANUEL HERNANDEZ-PAJARES is currently a Full Professor with the Technical University of Catalonia, Barcelona. Since 1989, he has been involved in GPS. Since 1994, he has focused in new algorithms for precise ionospheric sounding and GNSS navigation. From 2002 to 2007, he was the Chair and Product Coordinator of the International GNSS Service (IGS) Ionosphere WG and the Principal Investigator of many scientific projects received in competitive calls (10 of them in international competition). He has authored over 60 papers in peer reviewed journals. He is co-authoring two national and two international patents and three GPS processing books. He has been an Associate Editor of the IEEE TGARS and *Radio Science* journals, and belongs to working groups in IGS, ESA, and IAGG. He has co-organized the International Beacon Satellite Symposium Meeting, Barcelona, in 2010. He is currently an Expert Advisor of the European Space Agency in the GNSS Scientific Advisory Group.



PER HØEG received the M.S. degree in geophysics and Ph.D. degree in physics from the University of Copenhagen, Copenhagen, Denmark, in 1981 and 1987, respectively. From 1981 to 1986, he was a Researcher with the Danish Space Research Institute and from 1982 to 1985, the Max-Planck Institute for Aeronomy, Germany. From 1986 to 2004, he was a Senior Researcher and the Head of Research with the Danish Meteorological Institute. From 1994 to 2000, he was an external Associate Professor with the Niels Bohr Institute, University of Copenhagen. From 2004 to 2009, he was a Professor with Aalborg University. From 2009 to 2017, he was a Professor in satellite navigation, space technology, and atmosphere physics with the Technical University of Denmark, Kongens Lyngby, Denmark. He is currently a Professor with the Department of Physics, University of Oslo, Norway. His research interests include global navigation satellite systems (GNSS) satellite navigation, GNSS ocean reflections, ionosphere and atmosphere radio occultation, electromagnetic wave propagation, multipath phenomena, and turbulence.



ADRIAN JÄGGI received the Ph.D. degree in astronomy from the University of Bern, Bern, Switzerland, in 2006. From 2007 to 2009, he was a Research Associate with the Astronomical Institute, University of Bern (AIUB), and a Carl von Linde Junior Fellow with the Institute for Advanced Study, Technical University of Munich, Munich, Germany. In 2009, he became a Senior Research Scientist at AIUB, where he was responsible for research on precise orbit determination of low Earth satellites, gravity field recovery, and satellite laser ranging. Since 2012, he has been holding a professorship with the University of Bern. He is currently the Director of the AIUB. His main scientific interests include orbit and gravity field determination of artificial satellites orbiting the Earth, the Moon, and other planets. He is currently coordinating the H2020 Project European Gravity Service for Improved Emergency Management.



JUHA KAINULAINEN was born in Lappajärvi, Finland, in 1979. He received the M.Sc. degree in technology from the Helsinki University of Technology (currently part of the Aalto University), Espoo, Finland, in 2004, and the Ph.D. degree from Aalto University, Espoo, Finland, in 2013. He was a Ph.D. student with the Department of Radio Science and Engineering, Aalto University. From 1998 to 1999, he was a Trainee with Nokia Networks and Nokia Telecommunications. From 2001 to 2004, he was a Research Assistant with the Laboratory of Space Technology, Helsinki University of Technology. From 2004 to 2005, he was a Young Graduate Trainee with ESA. Since 2012, he has been a Principal

Scientist with Harp Technologies Oy, Finland. He was a Project Manager and the Chief System Engineer in micro- and millimeterwave related technology developments and system studies in the field of remote sensing and space technologies. His duties included development of the department's airborne synthetic aperture radiometer system HUT-2D, managing and involving in several projects in the frame of the ESA's Soil Moisture and Ocean Salinity (SMOS) mission, and involving in other projects related to microwave remote sensing. His work was related to signal processing of the payload instrument of the SMOS mission. His research interests include micro- and millimeterwave technologies, remote sensing systems, interferometry, and signal processing.

SHFAQAT ABBAS KHAN received the Ph.D. degree in geophysics from the University of Copenhagen, Copenhagen, Denmark, in 2004. From 2004 to 2007, he was a Research Associate Geodesy with the Department of Geodesy, National Space Institute, where he became a Senior Research Scientist in 2009. In 2011, he became an Associate Professor with the Technical University of Denmark (DTU Space). His main scientific interests are GPS and crustal motion geodesy, plate tectonics, elastic loading of the earth's surface, postglacial rebound, sea level change, GPS meteorology, realization of space geodetic reference frames, numerical modeling of geodynamic processes, ice sheet and glacier mass balance, ocean tide and atmosphere loading, and remote sensing. From 2010 to 2016, he was a Committee Member of the Nordforsk Program for Top-Level Research Initiative—Interaction between climate change and the cryosphere. Since 2015, he has been the Chair of the International Association of Geodesy Sub-Commission 3.4 (Crustal Deformation and Cryospheric Change).

NORBERT M. K. LEMKE received the Dipl.-Ing. degree in aerospace engineering from the Berlin University of Technology, Germany, in 1993. Since 1992, he has been a system engineer and a project manager for space projects for national and international institutional and commercial customers over all project phases. He is currently with OHB System as a Deputy Director for predevelopment, space system studies and proposals and is responsible for payloads and small satellites.



WEIQIANG LI received the bachelor's degree and the Ph.D. degree from Beihang University. His Ph.D. dissertation was conducted under the supervision of Prof. Q. Zhang and focused on the signal processing methods and instrument for reflected GNSS signal. In his Ph.D. research, he conceived and designed the GNSS-R instrument prototype, which could receive and process the direct and reflected GPS signal at L1 band. From 2008 to 2010, he was involved in different airborne and coastal verification experiments and focused on the processing of the data collected over sea surface. Since 2012, he has been involved in the ESA-China, work group on GNSS-R. As a part of ESA-China Talent Exchange Program, he studied on the subject of typhoon observation utilizing GNSS-R technique. From 2013 to 2014, he led a project that demonstrates the remote-sensing applications of ocean reflected signals from Beidou satellites. Since 2014, he has been involved in the project on designing of a GNSS remote-sensing small satellite constellation. During the past five years, he has authored over 10 papers in peer-reviewed journals and books on GNSS reflectometry. He has presented his work at several national and regional conferences. He was a recipient of two research awards from Chinese Society of Aeronautics and Astronautics and the GNSS and LBS Association of China and a recipient of the Excellent Youth Paper Award at the China Satellite Navigation Conference in 2014.



SON V. NGHIEM (M'85–S'03–F'15) received the B.S. degree in electrical engineering from Texas A&M University, College Station, TX, USA, in 1985, and the S.M. and Ph.D. degrees in electrical engineering and computer science from the Massachusetts Institute of Technology, Cambridge, MA, USA, in 1988 and 1991, respectively.

In 1991, he joined the Jet Propulsion Laboratory (JPL), California Institute of Technology, where he is currently a Senior Research Scientist, the Science and Applications Development Lead of the Radar Science and Engineering Section, and the JPL Hydrology Discipline Program Manager of the Hydrology Office in the Earth Science and Technology Directorate. His research encompasses active and passive remote sensing, development of advanced satellite radars and radiometers, electromagnetic scattering and emission modeling, and earth sciences and applications from the tropics to polar regions. He holds a patent for his invention on high-resolution wind measurements with satellite data for offshore wind energy development. He has authored 110 peer-reviewed articles and over 380 conference articles.

Dr. Nghiem received the 1999 Lew Allen Award for Excellence in recognition of his pioneering research in the areas of polarimetric scatterometry for Earth science remote sensing and contributions to future advanced satellite instrument concepts, the 2006 NASA Exceptional Achievement Medal for developing scientific applications of scatterometry in land, ice, and snow processes, the 2008 NASA Exceptional Scientific Achievement Medal for his contributions to understanding the melt state of Greenland and Antarctica ice sheets, its significance in Earth science missions, and its implications in climate change, the 2010 NASA Exceptional Technology Achievement Medal for his contributions in developing a new technology using NASA satellite scatterometer data to measure high-resolution global wind for offshore wind energy development, and the 2013 Edward Stones Award for outstanding research publication on the extreme melt across the Greenland ice sheet in 2012. He was invited to present science results on Arctic change and impacts to the Office of Science and Technology Policy in the White House in 2012. His research results have been reported worldwide by major news networks.



NAZZARENO PIERDICCA (M'04–SM'13) received the Laurea (Ph.D.) degree (*cum laude*) in electronic engineering from the Sapienza University of Rome, Rome, Italy, in 1981. From 1978 to 1982, he was with the Italian Agency for Alternative Energy. From 1982 to 1990, he was with the Remote Sensing Division, Telespazio, Rome. In 1990, he joined the Department of Information Engineering, Electronics and Telecommunications, Sapienza University of Rome, where he

is currently a Full Professor with the Faculty of Engineering and teaches remote sensing, antenna, and electromagnetic fields. His research interests include electromagnetic scattering and emission models for sea and bare soil surfaces and their inversion, microwave radiometry of the atmosphere, radar land applications, and bistatic radar. He is a past Chairman of the GRSS Central Italy Chapter and a member of the ESA GEROS-SAG.

MARCOS PORTABELLA received the B.Sc. degree in physics from the University of Barcelona, Spain, in 1994, the M.Sc. degree in remote sensing from the Institute of Space Studies of Catalonia, Spain, in 1995, and the Ph.D. degree in physics from the University of Barcelona in 2002. He is currently with the Institut de Ciències del Mar, Barcelona, Spain, where he was involved in satellite remote sensing. He is also involved in scatterometry and L-band radiometry.

KIMMO RAUTIAINEN received the M.Sc. degree from the Helsinki University of Technology (TKK), Espoo, Finland, in 1996. He was a Research Scientist with the TKK Laboratory of Space Technology focusing on microwave radiometer systems, with emphasis on interferometric radiometers. Since 2010, he has been a Research Scientist with the Finnish Meteorological Institute, Arctic Research, specializing in development of retrieval algorithms for passive microwave remote sensing, with a focus on cryosphere applications.



ANTONIO RIJS received the Ph.D. degree in astrophysics from Barcelona University, Barcelona, Spain, in 1974. From 1975 to 1985, he was a Member of the Technical Staff with NASA's Deep Space Communications Complex, Madrid, Spain, where he was responsible for the radio astronomical activities. Since 1986, he has been with the Spanish Consejo Superior de Investigaciones Científicas (CSIC), Barcelona. He is currently a CSIC Research Professor AH with the

research group on Earth Observation at the Institut d'Estudis Espacials de Catalunya (ICE-CSIC/IEEC).

INGO SASGEN received the Diploma degree in geophysics from the Ludwig-Maximilians-Universität München in 2004 and the Ph.D. degree (*summa cum laude*) from the Free University Berlin, GFZ German Research Center of Geoscience, in 2009. His core field of expertise is analyzing temporal satellite gravimetry for signatures of ice-mass change and glacial-isostatic adjustment. Since 2003, he has been a part of the European GRACE Science Team. He undertook a research visit at the Jet Propulsion Laboratories, California, USA, in 2013, and was with Pennsylvania State University, PA, USA, for two years from 2014 to 2015. From 2013 to 2015, he led the ESA Support To Science Project REGINA, including five institutional partners. Since 2016, he has been with the Alfred-Wegener-Institute, Bremerhaven, responsible for the development of multi-satellite products for continental ice mass change.

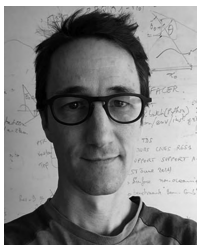


MAXIMILIAN SEMMLING received the degree in physics from Leipzig University, Leipzig, Germany, in 2007, and the Ph.D. degree from the Technical University of Berlin, Berlin, Germany, in 2012. Since 2008, he has been with the Department Geodesy, GFZ, Potsdam, Germany. He is experienced in ground-based experiments for sea ice reflectometry in the Arctic (Disko Bay, Spitsbergen), airborne experiments for sea surface altimetry with a Zeppelin airship over Lake

Constance and with the High Altitude Long range research aircraft over the Mediterranean Sea. He concentrates on simulations of the GEROS-ISS phase altimetry and preparations for an airborne experiment to study GNSS ice sheets reflections over Antarctica. His research interests include the field of GNSS reflectometry and its application for remote sensing.



C. K. SHUM is currently a Professor and a Distinguished University Scholar with the Division of Geodetic Science, School of Earth Sciences, The Ohio State University, Columbus, OH, USA. He was a Lead Author in the 2007 IPCC Working Group I (The Physical Science Basis), Fourth Assessment Report (AR4) Chapter, involving ocean climates and sea-level rise. He has authored over 240 journal articles. He and his group focuses on research topics including the use of geodetic measurements and understanding of the geophysical causes of global sea level rise, under anthropogenic climate change. He is a fellow of the American Association for the Advancement of Science and the International Association of Geodesy. He received the Vening Meinesz Medal from the European Geosciences Union for distinguished research in geodesy, and also many other awards.



tion Satellites, where he is currently involved in SAR and InSAR radar altimetry. He is currently coordinating the Phase B activities of the wide swath altimeter SWOT.

FRANÇOIS SOULAT received the Ph.D. degree in physics of remote sensing from the Polytechnic University of Catalonia, Barcelona, Spain, in 2004. From 2001 to 2006, he was with Starlab, where he was responsible of GNSS-R research projects. He spent almost two years at Mercator Ocean, Toulouse, France, as the Manager of European projects dedicated to the Copernicus Marine Services. Since 2007, he has been with the Space Oceanography Division, Collecte Localisation



Satellites, where he is currently involved in SAR and InSAR radar altimetry. He is currently coordinating the Phase B activities of the wide swath altimeter SWOT.

ANDREA K. STEINER received the Ph.D. degree in meteorology and geophysics from the University of Graz, Austria. She studied at Biosphere 2, AZ, USA, and was a Visiting Scientist at the Danish Meteorological Institute, Copenhagen, Denmark, the University Corporation for Atmospheric Research, and the National Center for Atmospheric Research, Boulder, CO, USA. Since 2003, she has been a Lecturer with the University of Graz, where she received the *venia docendi* in

geophysics and environmental system sciences in 2013 and was an appointed tenured Professor in 2017. She is currently the Vice Director of the Wegener Center for Climate and Global Change, University of Graz, and the Vice Head of Atmospheric Remote Sensing and Climate System Research Group, University of Graz. Her research in atmospheric and environmental physics focuses on atmospheric remote sensing and the use for climate change monitoring and research. She is an expert on radio occultation and its application for atmosphere and climate. <http://homepage.uni-graz.at/andi.steiner/>.

SÉBASTIEN TAILHADES received the master's degree in electrical and control engineering from ENSEEIHT, Toulouse, France. He was an Attitude and Orbit Control System Engineer with ESTEC, Noordwijk, and Thales Alenia Space, Cannes, from 2004 to 2007. He was a System Engineer for spaceborne Synthetic Aperture Radar missions with DLR until 2014, where he was involved in reconnaissance and civil projects like SAR-Lupe, SARah, and TerraSAR-X. He is currently with OHB System as a Marketing and Sales Manager.

MAIK THOMAS received the Ph.D. degree (*summa cum laude*) in geosciences from the University Hamburg in 2001. Since 2007, he has been the Head of the Earth System Modelling Section, GFZ, and holds a joint professorship of GFZ and Freie Universität Berlin on modeling of fluid dynamics in the Earth system. The main focus of his activities is on the simulation of near-surface fluid dynamics and their interactions with the solid earth. He is involved in numerous national and international research projects, is, among others, the head of the GGOS committee on Earth system modeling and has a strong background in the model-based utilization of integral observations, in particular the integration of geophysical/geodetic monitoring data into numerical system model approaches.



future developments. He has been involved in several ESA Earth observation and scientific programs (SMOS, Planck, SMOSops, SuperMIRAS, PARIS, GEROSS-ISS, GAIA, Meteosat 3rd Generation or Metop 2nd Generation), where the company has provided flight hardware like radiometers, GNSS reflectometers, and phase arrays, from UHF to Ka-band frequency. He has also been involved in MMIC and RF design of LNA's, downconverters, SSPA's, and frequency synthesizers for other flight programs.

ROGER VILASECA received the degree in telecommunication engineering from the Universidad Politècnica de Catalunya (UPC), Barcelona, Spain, in 2004, the degree in economics from the Universitat Oberta de Catalunya, and the degree in electronics engineer from UPC. Since 2000, he has been with TRYO Aerospace, where he is currently the Chief Technical Officer. He is responsible of the technical review and approval of flight hardware designed in the company and



between JPL and the academic community. She pioneered the global navigation satellite system reflectometry technique for ocean remote sensing and contributed to electromagnetic scattering and radiation research as a researcher.

CINZIA ZUFFADA received the Ph.D. in electronic engineering degree from the University of Pavia, Pavia, Italy. She was an Assistant Professor in electromagnetic fields theory with the University of Pavia. In 1992, she joined the Jet Propulsion Laboratory (JPL), Pasadena, CA, USA. She was the Manager of the Earth Remote Sensing Section, JPL Science Division. She is currently the Associate Chief Scientist with JPL. She oversees a number of programs supporting collaborations

...